

Department of Physics and Astronomy

Heidelberg University

Master thesis

in Physics

submitted by

Maja Lecher

born in Mödling, Austria

2023

**Radiation Damage Studies of a HV-CMOS particle detector in  
view of the application in the LHCb MightyTracker**

This Master thesis has been carried out by Maja Lecher

at the

Institute of Physics

under the supervision of

Prof. Dr. Ulrich Uwer

### Abstract

As one cornerstone of the prospective LHCb upgrade during Long Shutdown 4 in 2033, the current Scintillating Fibre tracker is set to be replaced by the MightyTracker, which combines scintillating fibres with radiation-hard silicon pixel detectors. The MightyPix sensor proposed as pixel detector employs the relatively new HV-MAPS technology. In preparation for the LHCb upgrade, the ATLASPix 3.1, a detector of similar build as the MightyPix, was studied with an emphasis on radiation damage. While a number of studies investigating the damage sustained by HV-MAPS from radiation exist, irradiation campaigns to date were carried out using unpowered sensors. In a first proof-of-principle measurement, a powered ATLASPix 3.1 was irradiated with 14 MeV protons at the Bonn Isochronous Cyclotron. A complementary irradiation campaign was carried out using an X-ray tube, with the intention of disentangling radiation damage effects from ionising and non-ionising energy loss. Specific sensor characteristics, most notably the leakage current, power consumption, and signal response, were tested before, during, and after irradiation in an effort to evaluate the performance and viability of HV-MAPS in the radiation environment expected for the MightyPix, and to develop a suitable testing environment for future studies.

### Abstract

Der Scintillating Fibre-Tracker des LHCb soll während der vierten Wartungspause in 2033 aufgerüstet werden zu einem hybriden Detektor namens MightyTracker, der die aktuell verwendete Technik der Szintillationsfasern mit strahlenhärteren Pixeldetektoren verbindet. Der dafür angedachte MightyPix-Sensor ist ein HV-MAPS-Pixelsensor der neuen Generation, dessen Vorgänger, der ATLASPix 3.1, im Rahmen dieser Arbeit mit einer besonderen Gewichtung auf Strahlenhärte untersucht wird. Anders als frühere Studien wurde der Sensor für die hier präsentierten Messungen unter Vorspannung bestrahlt. In einer ersten Bestrahlungskampagne seiner Art wurde der ATLASPix 3.1 unter Vorspannung am Bonner Isochron-Zyklotron mit 14 MeV-Protonen bestrahlt. Eine komplementäre Bestrahlungskampagne mit Röntgenphotonen soll Hinweise auf potentielle Unterschiede zwischen den Strahlenschäden ionisierender und nicht-ionisierender Strahlung liefern. Hierfür wurden bestimmte Sensoreigenschaften wie der Leckstrom, der Stromverbrauch, sowie die Signalverarbeitung vor, während, und nach der Bestrahlung untersucht. Das Ziel dieser Arbeit ist es sowohl, die Leistung des Sensors unter den erwarteten Bedingungen zu analysieren, als auch eine geeignete Messinfrastruktur für zukünftige Messungen dieser Art aufzubauen.

# Contents

|          |  |           |
|----------|--|-----------|
| <b>1</b> | <b>Introduction</b>  | <b>6</b>  |
| 1.1      | The Standard Model of Particle Physics . . . . .   | 6         |
| 1.2      | The LHCb Experiment . . . . .  | 7         |
| 1.2.1    | Physics Case . . . . .   | 8         |
| 1.2.2    | The LHCb detector . . . . .  | 8         |
| 1.2.3    | The MightyTracker . . . . .  | 9         |
| <b>2</b> | <b>Interactions of Particles with Matter</b>   | <b>11</b> |
| 2.1      | Charged particles . . . . .  | 11        |
| 2.1.1    | Ionisation . . . . .   | 11        |
| 2.1.2    | Bremsstrahlung . . . . .   | 13        |
| 2.1.3    | Multiple Coulomb Scattering . . . . .  | 13        |
| 2.2      | Photons . . . . .  | 13        |
| 2.2.1    | Photoelectric Effect . . . . .   | 13        |
| 2.2.2    | Compton Scattering . . . . .   | 13        |
| 2.2.3    | Pair production . . . . .  | 14        |
| <b>3</b> | <b>Silicon Pixel Detectors</b>   | <b>15</b> |
| 3.1      | Semiconductor theory . . . . .   | 15        |
| 3.1.1    | Doping . . . . .   | 16        |
| 3.1.2    | The p-n junction . . . . .   | 17        |
| 3.1.3    | MOSFETs . . . . .  | 21        |
| 3.2      | Pixel sensors . . . . .  | 22        |
| 3.2.1    | Signal generation . . . . .  | 22        |
| 3.2.2    | Readout electronics . . . . .  | 23        |
| 3.2.3    | Electronic noise . . . . .   | 25        |
| <b>4</b> | <b>ATLASPix 3.1</b>  | <b>26</b> |
| 4.1      | Sensor architecture . . . . .  | 26        |
| 4.1.1    | Active pixel matrix . . . . .  | 26        |
| 4.1.2    | Periphery . . . . .  | 28        |
| 4.1.3    | Readout scheme . . . . .   | 28        |
| 4.1.4    | Test outputs . . . . .   | 28        |
| 4.2      | Time over Threshold . . . . .  | 29        |
| 4.3      | Breakdown voltage . . . . .  | 29        |
| <b>5</b> | <b>Radiation damage</b>  | <b>30</b> |
| 5.1      | Substrate damage . . . . .   | 30        |
| 5.1.1    | Annealing . . . . .  | 31        |
| 5.1.2    | NIEL Hypothesis . . . . .  | 31        |
| 5.1.3    | Effect of substrate damage on sensor properties and implications for<br>detector operation . . . . . | 32        |
| 5.2      | Surface damage . . . . .   | 37        |

|          |   |           |
|----------|---|-----------|
| <b>6</b> | <b>Measurement Infrastructure</b>                                       | <b>39</b> |
| 6.1      | DAQ systems and measurement infrastructure . . . . .                    | 39        |
| 6.1.1    | GECCO readout system . . . . .  | 39        |
| 6.1.2    | PCIe power adapters . . . . .   | 40        |
| 6.1.3    | PixMon slow control system . . . . .                                    | 40        |
| 6.1.4    | Cooling setup and temperature monitoring . . . . .                      | 40        |
| 6.2      | Particle sources . . . . .  | 43        |
| 6.2.1    | X-ray tube . . . . .  | 43        |
| 6.2.2    | Proton beam at the Bonn Isochronous Cyclotron . . . . .                 | 44        |
| 6.2.3    | $^{55}\text{Fe}$ . . . . .  | 45        |
| <b>7</b> | <b>Simulating LHCb rates with a tabletop X-ray tube</b>                 | <b>46</b> |
| 7.1      | Setup . . . . .   | 46        |
| 7.2      | Cluster corrections . . . . .   | 47        |
| 7.3      | Sanity checks . . . . .   | 48        |
| 7.4      | Achievable hit rate . . . . .   | 51        |
| <b>8</b> | <b>Energy calibration of the ATLASPix 3.1</b>                           | <b>53</b> |
| 8.1      | Setup . . . . .   | 53        |
| 8.2      | Expected energy spectrum of X-ray photons . . . . .                     | 54        |
| 8.3      | Energy dependence of ToT . . . . .                                      | 55        |
| <b>9</b> | <b>Studies on radiation damage</b>                                      | <b>58</b> |
| 9.1      | Systematic limitations . . . . .  | 59        |
| 9.1.1    | Impact of SMU measure range . . . . .                                   | 59        |
| 9.1.2    | Delay of temperature sensor . . . . .                                   | 59        |
| 9.1.3    | Impact of light sensitivity on leakage current . . . . .                | 60        |
| 9.1.4    | Impact of chip configuration on leakage current . . . . .               | 60        |
| 9.2      | Proton irradiation of a powered ATLASPix 3.1 . . . . .                  | 61        |
| 9.2.1    | Setup . . . . .   | 61        |
| 9.2.2    | Irradiation protocol . . . . .  | 62        |
| 9.2.3    | Beam-induced current . . . . .  | 63        |
| 9.2.4    | Leakage current . . . . .   | 66        |
| 9.2.5    | Breakdown voltage . . . . .   | 70        |
| 9.2.6    | S-Curves . . . . .  | 74        |
| 9.2.7    | VDAC response . . . . .   | 76        |
| 9.2.8    | Noise . . . . .   | 76        |
| 9.2.9    | Signal response . . . . .   | 81        |
| 9.3      | Long-term X-ray irradiation of a powered ATLASPix 3.1 . . . . .         | 83        |
| 9.3.1    | Beam-induced current and breakdown voltage during irradiation . . . . . | 84        |
| 9.3.2    | Long-term X-ray irradiation . . . . .                                   | 86        |
| 9.3.3    | Leakage current after long-term irradiation . . . . .                   | 89        |
| 9.3.4    | Impact of long-term irradiation on breakdown voltage . . . . .          | 93        |
| 9.3.5    | Signal response . . . . .   | 93        |
|          | <b>Summary and Outlook</b>  | <b>95</b> |

# Chapter 1

## Introduction

Numerous advances over the years have led to the development of the Standard Model (SM), which describes all known elementary particles along with the four fundamental forces. It is the success story of modern physics: with the discovery of the Higgs Boson at the LHC in 2012, the existence of all particles predicted within its framework have now been found. Despite the remarkable success with which the SM has predicted phenomena which have now been experimentally confirmed, observations like the matter-antimatter asymmetry of the Universe and the existence of Dark Matter are not covered within its framework. The implication that the SM is incomplete has ushered in a new era of physics, with many dedicated experiments still being developed to unify theory and observation.

The LHCb experiment is one of the experiments searching for evidence of New Physics at the energy frontier. In an effort to increase its statistical power, it will undergo a second major upgrade to higher luminosities after the end of its current run in 2033. To cope with the increased luminosity and the correspondingly harsher radiation environment, the current downstream Scintillating Fibre (SciFi) tracker is set to be upgraded to a hybrid detector. In the proposed MightyTracker, the innermost part of the SciFi will be replaced by radiation-hard MightyPix sensors, which are a type of silicon High-Voltage Monolithic Active Pixel Sensors (HV-MAPS).

The increased demands on the radiation tolerance of the upgraded detector requires a good understanding of the radiation damage expected for its detectors. In preparation for the arrival of the MightyPix sensor, this thesis presents a first effort to develop the suitable measurement infrastructure and characterisation routines necessary for its detailed investigation by the LHCb group in Heidelberg.

### 1.1 The Standard Model of Particle Physics

The Standard Model of Particle Physics is the framework within which the fundamental laws of nature are formulated in modern physics. It describes the particle constituents of the universe along with their interactions in a unified picture consisting of twelve spin-1/2 fermions, 4 spin-1 gauge bosons, and the spin-0 Higgs boson, distinguished by a set of distinct quantum numbers. An overview of the standard model particles is shown in fig. 1.1.

The fermions are separated into leptons and quarks, both of which are grouped into three generations of increasing mass. While the lighter particles of the first generation are stable and constitute the vast majority of everyday matter, the heavier charged particles

of the higher generations decay into lower-generation particles through numerous decay channels.

The four fundamental forces are mediated by the gauge bosons. The electromagnetic force is associated with the massless photon and interacts with all electrically charged particles. The W- and Z bosons mediate the weak interaction and facilitate the transition of particles between different generations. The electromagnetic and weak forces are unified into a single electroweak (EW) theory. [1]

The strong force is mediated by eight massless gluons and is described separately by quantum chromodynamics (QCD). Unlike photons, which do not carry any charges, the gluon itself carries the colour charge associated with the strong force. As a consequence of the resulting self-interaction, the range of the strong force is limited, and quarks and gluons are confined to colour-neutral hadrons.

The quarks of each generation have a fractional elementary charge of  $+2/3$  and  $-1/3$ , respectively. In addition to the electric charge, quarks also carry colour charge and interact via the strong force.

The electron, muon, and tau lepton each have an elementary charge of  $-1$ , and are accompanied by a corresponding electrically neutral neutrino. Within the Standard Model, neutrinos are massless, which is in contradiction with the observed neutrino oscillations.

The Higgs boson is the final standard model particle to be experimentally confirmed, and is responsible for the mass of the W and Z bosons. [5]

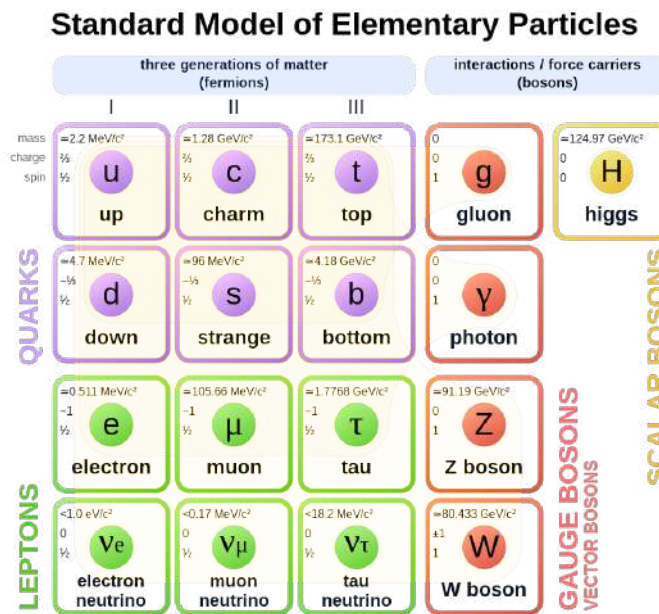


Fig. 1.1 The Standard Model of Particle Physics [2]

## 1.2 The LHCb Experiment

The Large Hadron Collider (LHC) is a proton-proton synchrotron located in an underground tunnel underneath the French-Swiss border near Geneva. It is operated by the European Organisation for Nuclear Research (CERN) and is, with a circumference of 27 km, the largest particle accelerator in the world at the time of this writing.

The LHC is designed to accelerate protons to a maximum center-of-mass energy of  $\sqrt{s} = 14 \text{ TeV}$ , which are brought to collision at four points around the accelerator ring. Each interaction point serves as the basis of one of the four major LHC experiments ALICE (A Large Ion Collider Experiment), ATLAS (A Toroidal LHC ApparatuS), CMS

(Compact Muon Solenoid), and LHCb (LHC beauty). [3]

### 1.2.1 Physics Case

LHCb is a heavy flavour precision physics experiment specialised in  $b$  physics, with a primary goal of finding indirect evidence of New Physics in CP-violating rare decays of hadrons containing  $b$  and  $c$  quarks [44].

The detection concept exploits the distinctive flavour structure of the Standard Model, which forbids flavour-changing processes involving neutral bosons at tree level:

Within the Standard Model, quark mixing is mathematically described by the CKM (Cabbibo-Kobayashi-Masakawa) matrix. To explain the observed matter-antimatter asymmetry of the Universe, a set of three conditions was proposed by Andrei Sakharov in 1967 [4]. Among these is the violation of CP symmetry at a level that is not compatible with the constraints on the possible values of the CKM matrix, which allows for CP violation as a single irreducible complex phase [5]. As the resulting CP violation in the weak interaction of hadrons is not sufficient to explain the matter-antimatter asymmetry in the Universe, the search for sources of CP violation is extended beyond the Standard Model.

Given that many models of New Physics give rise to changes in the expectation values of the CP-violating phases or the branching fractions of rare decays predicted for heavy flavour physics by the Standard Model, precision measurements in this sector are a promising path to unifying theory and observation.

### 1.2.2 The LHCb detector

Starting its first data-taking run in 2010 at a center of mass energy of  $\sqrt{s} = 7$  TeV, the original LHCb experiment underwent several upgrades leading up to its retirement in 2018. During this time, the detector collected data equivalent to an integrated luminosity of  $9 \text{ fb}^{-1}$ .

Following the most recent upgrade during Long Shutdown 2 (LS2) from 2018 to 2022, the detector is now equipped to cope with an instantaneous luminosity increased by a factor of five. The upgraded detector is expected collect data corresponding to an integrated luminosity of  $50 \text{ fb}^{-1}$  by the end of Run 4, before undergoing another major upgrade during LS4 starting in 2033. [3]

The specialized nature of the LHCb detector is reflected in its basic detector layout: unlike the ATLAS and CMS detectors, which are built around the entire collision point in an onion structure, LHCb is implemented as a single-arm forward spectrometer with an approximate coverage of 15 to 300 mrad in the bending, and 15 to 250 mrad in the non-bending plane. This design is a result of the large forward (v.v. backward) momentum of the  $b$ - and  $\bar{b}$ - hadrons produced at high energies [44]. Each of its six subdetectors fulfills one of two basic tasks: the tracking system comprising the Vertex Locator (VELO), the Upstream Tracker (UT), and the Scintillating Fibre Tracker (SciFi) is responsible for measuring the track and momentum of traversing particles, while the particle identification (PID) system consisting of two Ring Imaging Cherenkov Detectors (RICH1 and RICH2), an electromagnetic and a hadronic calorimeter (ECAL and HCAL), and the Muon System (M2-M5) is built to identify the particle species.

An overview of the detector layout with its various subdetectors is shown in fig. 1.2.

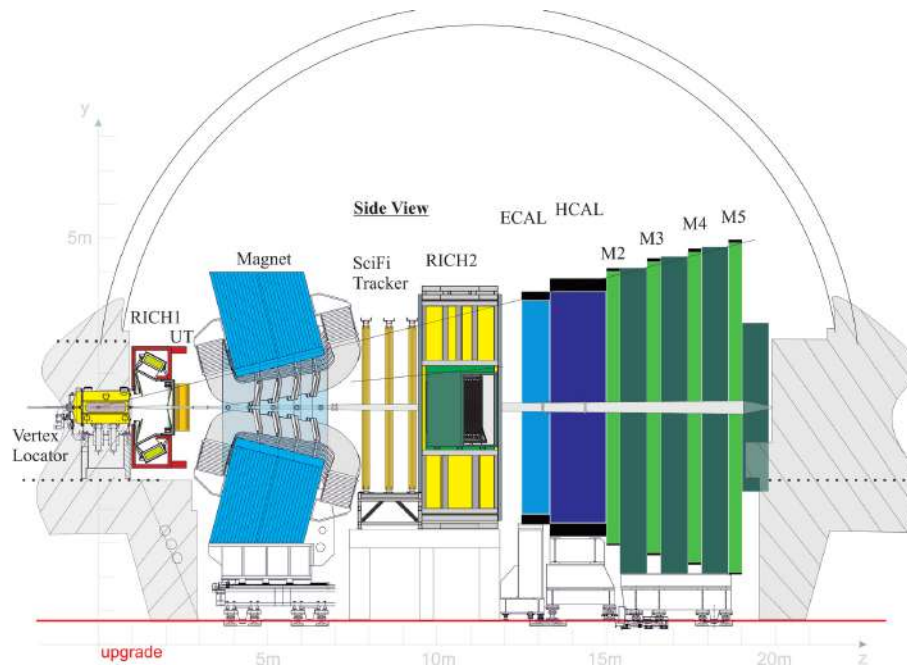


Fig. 1.2 LHCb upgrade I detector. [6]

### 1.2.3 The MightyTracker

To improve its sensitivity to rare processes, a second major upgrade to the LHC is planned for Long Shutdown 4 (LS4) between 2033 and 2035. The Upgrade-II LHCb detector is foreseen to operate at a nominal instantaneous luminosity of  $1.5 \times 10^{34}$   $1/\text{cm}^2\text{s}$  during Run 5 and Run 6, leading to an increased occupancy and a harsher radiation environment. To cope with the new operating conditions, all LHCb subdetectors will be partially or fully upgraded. With the increase in luminosity, the current Scintillating Fibre tracker is expected to record an increase of fake tracks, and experience accelerated ageing that will negatively impact the tracking performance [44]. To mitigate these effects, the SciFi is set to be re-modeled into a new hybrid downstream tracking system by replacing its innermost region, the Inner Tracker (IT), with radiation-hard pixel detectors. With this approach, the proposed MightyTracker (MT) combines the advantages of the high granularity, low ghost rate, and high radiation tolerance of silicon pixel detectors with the low cost and low material budget of the scintillating fibres.

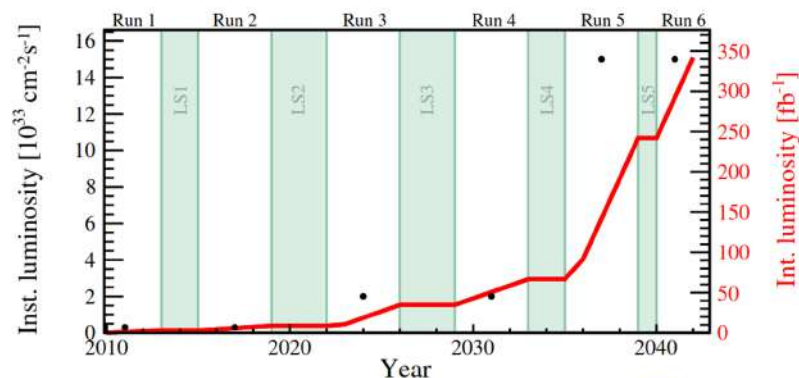


Fig. 1.3 Scheduled luminosity evolution of the LHCb detector [29]

The pixel detector proposed for the MT is the MightyPix, a High-Voltage Monolithic Active Pixel Sensor (HV-MAPS). Its monolithic structure serves to reduce the material budget and associated absorption and multiple scattering effects, while the commercial manufacturing process makes it a more affordable option than competing pixel detector

types. A detailed introduction to HV-MAPS detectors and their principle of operation is given in Ch. 3.

Like the Upgrade-I SciFi, the MightyTracker will consist of three separate tracking stations. Each of the tracking stations is foreseen to be instrumented with two staggered layers of MightyPix sensors, installed in two stages: to reduce the signal-to-noise ratio, the two inner modules of the SciFi are due to be replaced during LS3. This offers the opportunity to equip the inner region with MightyPix sensors as a proof of concept, before expanding the MightyPix-covered area to its full intended scale of  $3 \text{ m}^2$  per layer during LS4.

The proposed layout of the MT is shown in fig. 1.4. The area expected to be installed during LS3 is shown in pink, the Upgrade II-installment in blue. [11]

Conflicting reports exist regarding the expected radiation environment in this area, with some FLUKA simulations showing that the Inner Tracker will need to withstand a maximum integrated neutron fluence of  $5.9 \times 10^{14} \text{ n}_{\text{eq}}/\text{cm}^2$  [44], others that the maximum expected fluence is  $2 \times 10^{15} \text{ n}_{\text{eq}}/\text{cm}^2$ , corresponding to a total ionising dose (TID) of 400 kGy [44] [8] [9].

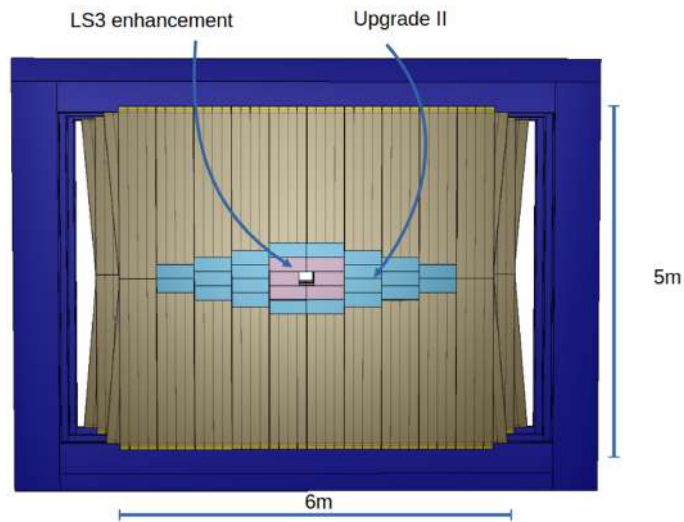


**Fig. 1.4** Layout of a prospective MightyTracker module [29]

## Chapter 2

# Interactions of Particles with Matter

A particle passing through a detector must fulfill two basic requirements in order for it to be detectable: it must interact with the material of the detector, and it must transfer energy in some recognizable fashion. The type and magnitude of energy loss occurring as a result of a given interaction depends on properties of both the particle and the traversed material, and as such can yield valuable information about eg. the mass, charge, and energy of an incident particle.

To aid comprehension, it is useful to separate the types of energy loss by the particle species that undergo them: while charged particles commonly lose energy via ionisation, Bremsstrahlung, Multiple Coulomb Scattering, and Cherenkov radiation, photons typically undergo pair production or transfer energy via Compton scattering or the photoelectric effect.

In order to correctly contextualize the behaviour of the sensor studied within the scope of this thesis, a solid understanding of the physics underlying the interaction of particles is vital. This chapter is therefore dedicated to the processes that are most relevant for the investigated Silicon pixel detectors.

### 2.1 Charged particles

A charged particle traversing matter predominantly interacts with it via the electromagnetic force. This interaction can take several forms, depending on the mass and velocity of the impinging particle: while ionisation is the dominant mechanism for non-relativistic particles, radiation processes such as Bremsstrahlung gain importance for particles in the highly relativistic energy regime.

#### 2.1.1 Ionisation

The mean ionisation energy loss of a charged particle heavier than an electron traversing atoms is governed by the Bethe-Bloch eq.

$$-\left\langle \frac{dE}{dx} \right\rangle = Kz^2 \frac{Z}{A} \frac{1}{\beta^2} \left[ \frac{1}{2} \ln \frac{2m_e c^2 \beta^2 \gamma^2 T_{\max}}{I^2} - \beta^2 - \frac{\delta(\beta\gamma)}{2} \right], \quad (2.1)$$

where  $K = 0.307 \text{ MeV cm}^2/\text{mol}$ ,  $z$  and  $\beta$  are the charge and velocity of the impinging particle, respectively,  $Z$  and  $A$  are the atomic number and -mass of the medium,  $I$  is the mean excitation energy,  $T_{\max}$  the maximum possible energy transfer to a shell electron

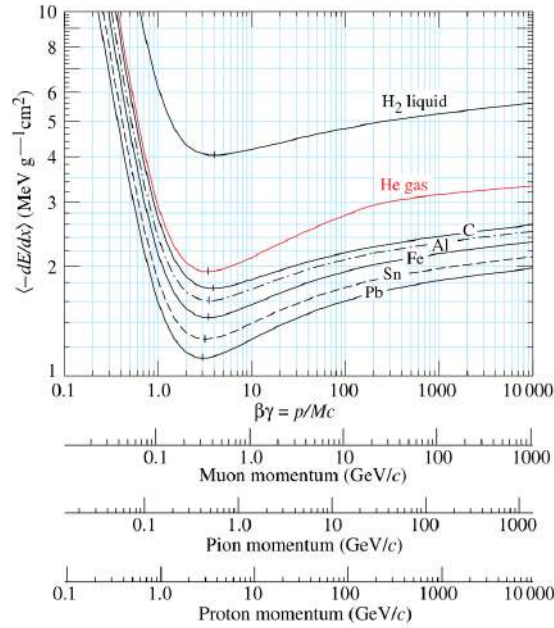


**Fig. 2.1** Bethe-Bloch formula describing the mean energy loss of heavy particles. [12]

in a central collision, and  $\delta(\beta\gamma)$  the density correction, which becomes relevant at high energies.

Fig. 2.1 shows the energy loss as a function of the incident particle's initial kinetic energy for a number of different materials. The origin and implications of the function is best understood by considering three key regimes:

At low energies, i.e. for  $\beta\gamma \lesssim 3$ , the mean ionisation energy loss of a charged particle is dominated by the  $1/\beta^2$  term. At these energies, particles are subject to a larger momentum transfer  $p_T$  since they are in the electric field of the atomic electron for a longer period of time, where  $p_T = \int F dt = e \int E_T \cdot \frac{dx}{v}$ .

Particles populating the minimum at  $\beta\gamma \approx 3 - 4$  are referred to as *Minimum Ionising Particles* (MIPs) and are often of particular interest: as they transfer the least amount of energy to the material they pass through, they are expected to generate the smallest amount of charge in a given detection medium. This makes the detection of MIPs an important benchmark for the efficiency and viability of a detector.

At higher particle energies, the Lorentz contraction of the electric field of atoms in the traversed medium is no longer negligible. As a consequence, incident particles can interact with an increasing number of far-away atoms. This long-range contribution manifests as the logarithmic rise in energy loss seen beyond the minimum of the Bethe-Bloch eq., i.e. for  $\beta\gamma \gtrsim 3$ . As the energy of the particles and therefore the strength of the transverse fields increase, the relativistic rise flattens into the Fermi plateau due to the resulting polarization of the traversed medium. This effect is accounted for via the density correction term  $\delta(\beta\gamma)$ .

Electrons and positrons constitute a special case that requires separate treatment for two reasons: firstly, their small mass leads to a larger deflection and an increased Bremsstrahlung contribution at low momenta. Secondly, the bulk matter traversed by a particle necessarily contains electrons. As such, the indistinguishability of electrons must be taken into account, as well as the additional energy loss experienced by positrons due to annihilation with bulk electrons. Appropriate modifications to the Bethe-Bloch equation lead to the Berger-Seltzer formula, which describes the mean ionisation energy loss of electrons and positrons.

Given that the energy loss of particles in matter is a statistical process, it can be described by a probability distribution. In silicon detectors, this takes the form of a Vasilov distribution, which is a Landau distribution convoluted with a Gaussian to account for  $\delta$  electrons. [26]

### 2.1.2 Bremsstrahlung

The electromagnetic radiation produced by the deceleration of highly relativistic charged particles when deflected by the Coulomb field of other charged particles — typically an electron in the field of an atomic nucleus — is known as **Bremsstrahlung**. The emission of a Bremsstrahlung photon is a consequence of the conservation of energy, which manifests as the conversion of the kinetic energy lost by the decelerated particle into a photon. The Bremsstrahlung energy lost by an impinging particle with an energy  $E$  can be approximated using the material-dependent **radiation length**  $X_0$  [26], where

$$\frac{dE}{dx} = -\frac{E}{X_0}. \quad (2.2)$$

### 2.1.3 Multiple Coulomb Scattering

Charged particles traversing through matter can interact with the Coulomb fields of the nuclei, resulting in many small-angle scattering processes. Given that multiple scattering can limit the momentum and vertex resolution of particle detectors, its impact should be minimised. This is best achieved by reducing the material budget of the detector. [26]

## 2.2 Photons

The main interaction processes undergone by photons are the photoelectric effect, Compton scattering, and pair production. While other forms of interactions like Rayleigh scattering exist, their cross section is small and their contribution typically negligible within the context of particle detection.

### 2.2.1 Photoelectric Effect

The photoelectric effect describes the full absorption of an impinging photon by an atom, which emits the absorbed energy in the form of an electron. The leftover vacancy in the atomic shell is filled by an electron of a higher shell, which releases the difference in binding energy via another photon. For the photoelectric effect to occur, the initial photon energy must exceed the binding energy of the shell electron. [26].

### 2.2.2 Compton Scattering

A photon losing a portion of its energy via elastic scattering on shell electrons is described by the Compton effect. The final energy  $E'_\gamma$  of the scattered photon depends of its initial energy  $E_\gamma$  and the scattering angle  $\phi$ ,

$$E'_\gamma = \frac{E_\gamma}{1 + \frac{E_\gamma}{m_e c^2} (1 - \cos(\phi))}, \quad (2.3)$$

where  $m_e$  is the electron mass, and  $c$  the speed of light. [26]

### 2.2.3 Pair production

Pair production describes the conversion of a photon into an electron-positron pair in the field of a nucleus, where the nucleus is necessary for the conservation of momentum. This process requires the full transfer of the photon energy to the rest mass and kinetic of the final-state particles, and therefore has an energy threshold of

$$E_\gamma \geq 2m_e c^2 \left( 1 + \frac{m_e}{m_n} \right), \quad (2.4)$$

where  $m_e$  and  $m_n$  are the mass of the electron and the nucleus, respectively. [26]

# Chapter 3

## Silicon Pixel Detectors

Compared to other detector types, semiconductor detectors feature several advantages that make them an excellent candidate for tracking and vertexing in high-energy physics (HEP). These include a large amount of energy loss in a short distance, a low ionisation energy of a few eV – compared to 20 - 40 eV for gas detectors and 400-1000 eV for scintillators –, high mobility, and a small amount of diffusion.

Silicon in particular has proven to be a suitable element for particle detection. This is in part due to its moderate band gap of 1.12 eV, which translates to an average energy of 3.6 eV for the creation of an electron-hole pair. This low ionisation energy leads to a high carrier yield and good energy resolution. The high specific energy loss is also beneficial in terms of the resulting low material budget and good spacial resolution, while the high carrier mobility leads to a fast collection time. Finally, silicon semiconductors have a relatively high intrinsic radiation hardness, and their use allows the HEP community to benefit from a vast amount of industry experience.

This chapter provides an introduction to the general working principle of semiconductors and their application as silicon pixel detectors.

### 3.1 Semiconductor theory

Depending on their ability to conduct electricity, solids can be classified as either insulators, semiconductors, or conductors. The classification scheme derives from the **band model**, which provides a theoretical description of the energy levels of electrons within a crystal.

The energy states of electrons in an electric potential  $U(\vec{r})$  are governed by the time-independent Schrödinger equation

$$\left(-\frac{\hbar^2}{2m}\vec{\nabla}^2 + U(\vec{r})\right)\Psi(\vec{r}) = E\Psi(\vec{r}), \quad (3.1)$$

where  $\hbar$  is the Planck constant, and  $\Psi$  a wave function.

The probability that a given energy state  $E$  is occupied in thermodynamic equilibrium is given by the **Fermi-Dirac distribution**

$$f(E) = \frac{1}{e^{\frac{E-E_F}{k_B T}} + 1}, \quad (3.2)$$

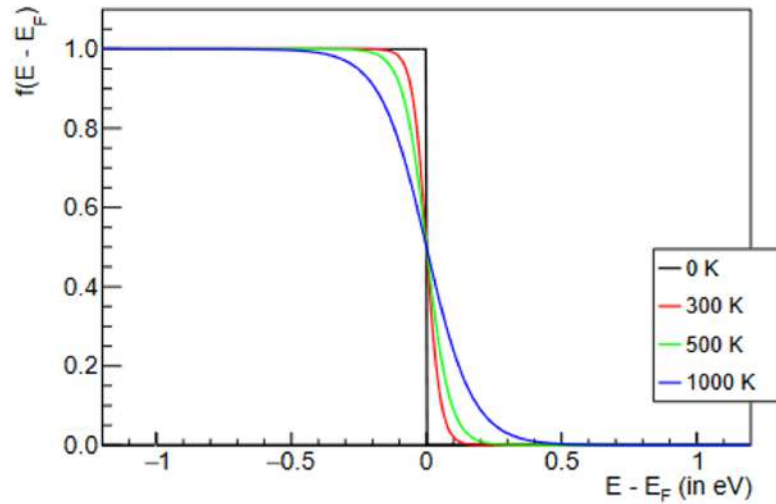


**Fig. 3.1** Fermi distribution for a range of temperatures [19]

where the **Fermi level**  $E_F$  denotes the energy at which  $E$  is occupied with a probability of 50%. At a temperature of  $T = 0\text{ K}$ , all states below  $E_F$  are fully occupied, while all states above  $E_F$  are empty. Fig. 3.1 shows eq. 3.2 for a range of different temperatures.

In a crystal lattice, the discrete electronic energy states that arise as a result of eq. 3.1 with a periodic potential can be treated as a quasi-continuum due to the large number of states within the crystal. The two bands on either side of the Fermi level, the conduction band (i.e. the lowest band that is not fully occupied in the ground state) and valence band (i.e. the band below the conduction band, and the highest band that is fully occupied in the ground state), are of particular importance as their position relative to each other plays a decisive role for the conductivity of the material. If they overlap, electrons and holes can freely move between the conduction and valence bands. Such materials are classified as metals. If the conduction and valence bands do not overlap, i.e. if there is a band gap  $E_G = E_C - E_V > 0$ , where  $E_C$  is the lowest state in the conduction band and  $E_V$  the highest state in the valence band, the charge carriers are initially confined to their respective bands. A fully occupied valence band does not contain the free states necessary to create charge movement, while an empty conduction band cannot conduct any charge since it is devoid of electrons. Hence, no current is conducted by default. If sufficient energy is introduced to the system, however, electrons in the valence band can be excited into the conduction band. Whether a material is classified as a semiconductor or an insulator therefore depends on the size of the band gap. While the precise value is not clearly defined in literature, the split is typically in the range of 3 to 4 eV, which is sufficiently small for electrons to move from the valence to the conduction band via thermal excitation.

### 3.1.1 Doping

The conductivity of semiconductors can be modified by deliberately introducing impurities to the crystal lattice. Such impurities can create additional energy states in the band gap, which makes thermal ionisation more likely, and increase the number of free charge carriers. It is common to choose dopants of main element groups adjacent to that of the pure semiconductor material. Depending on the type of majority charge carrier it introduces, the impurity is referred to as either a **donor** or **acceptor**. Donors, which are impurity atoms with more valence electrons than the base material, create **n-type** semiconductors by introducing excess electrons in the conduction band. Acceptors, i.e. atoms with fewer valence electrons, produce **p-type** semiconductors with holes as majority charge carriers in the valence band.

Silicon has four valence electrons and is typically doped with boron (group 3) or phosphorus (group 5), with doping concentrations that are orders of magnitude larger than the intrinsic charge carrier densities at room temperature. The addition of phosphorus creates donor levels  $E_D$  close to the conduction band, where  $E_C - E_D = 0.045$  eV. These are nearly completely ionised at room temperature, meaning that the electrons are transported to the conduction band. For boron, acceptor levels  $E_A$  close to the valence band are introduced, where  $E_A - E_V = 0.045$  eV. Electrons from the valence band will fill these almost completely, leaving behind holes.

### 3.1.2 The p-n junction

When two semiconductor materials of opposite types are brought into contact, a charge carrier-free zone forms at their junction. This area, known as a **depletion zone**, acts as a diode, and can be used to detect the passage of ionising particles. The formation and properties of the depletion zone are described below.

The additional energy states created via doping changes the Fermi level of a semiconductor. For intrinsic semiconductors, the Fermi level is given by

$$E_i = \frac{E_C + E_V}{2} + \frac{3k_B T}{4} \cdot \ln\left(\frac{m_p}{m_n}\right), \quad (3.3)$$

where  $m_p$  and  $m_n$  are the (unequal) effective masses of the electrons and holes [24]. In doped, or **extrinsic**, semiconductors, the level shifts as a function of the doping concentration. For n-doped semiconductors, the Fermi level is given by

$$E_F = E_C - k_B T \ln\left(\frac{N_C}{N_D}\right), \quad (3.4)$$

where  $N_D$  is the donor concentration. For p-type material, it is

$$E_F = E_V + k_B T \ln\left(\frac{N_V}{N_A}\right), \quad (3.5)$$

where  $N_A$  is the acceptor concentration.  $N_C$  and  $N_V$  are the effective densities of states in the conduction and valence bands, respectively.

Once the p- and n-type semiconductors are brought into contact, electrons from the n-doped region start to diffuse across the junction due to the difference in charge concentration. The movement is described by Fick's law of diffusion,

$$\vec{j}_{\text{diff}} = -qD\nabla n, \quad (3.6)$$

where  $\vec{j}_{\text{diff}}$  is the diffusion current,  $q$  the charge of a single charge carrier,  $D$  the diffusion constant, and  $n$  the charge carrier density.

Upon reaching the p-doped region, the electrons can recombine with local excess holes. The space charge between the newly occupied acceptor states and the positively charged holes left in the p-doped region creates an electric field that counteracts the diffusion. The potential difference is referred to as the **built-in voltage**

$$U_{\text{bi}} = \frac{k_B T}{q} \ln\left(\frac{N_A N_D}{n_i^2}\right), \quad (3.7)$$

where  $n_i$  is the intrinsic charge carrier density. For pure silicon, it is around 0.6 V [26]. The width of the depletion zone, once an equilibrium between drift and diffusion has been established, is given by

$$w = \sqrt{\frac{2\epsilon_r\epsilon_0}{q} \frac{N_D + N_A}{N_D N_A} |U_{bi}|}, \quad (3.8)$$

where  $\epsilon_0$  and  $\epsilon_r$  are the vacuum- and relative permittivity, respectively.

### The p-n junction under external voltage

The width of the depleted area can be modified by applying an external voltage  $U_{ext}$  between the two sides of the junction: a **reverse bias**, where the negative pole is connected to the p-type and the positive pole to the n-type region, increases  $w$ , while a **forward bias** decreases it (see fig. 3.2). Typically, semiconductors used for particle detection are operated in reverse bias in an effort to maximise the size of the depletion zone. The modified depletion width for small external voltages  $U_{ext} < U_{bi}$  is given by

$$w = \sqrt{\frac{2\epsilon_0\epsilon_r}{q} \frac{N_D + N_A}{N_D N_A} (U_{bi} - U_{ext})}. \quad (3.9)$$

For silicon sensors, eq. 3.9 can be approximated by

$$w \approx \sqrt{\frac{2\epsilon_0\epsilon_{Si}}{qN_D} |U_{ext}|} \quad (3.10)$$

since the junction typically consists of a shallow, highly-doped p<sup>+</sup> implant with  $N_A > 10^{18}$  cm<sup>-3</sup> in a low-doped bulk material with  $N_D \approx 10^{12}$  cm<sup>-3</sup>, and the built-in voltage of order 0.5 V is much smaller than the externally applied bias voltages [30].

The voltage necessary to extend the depleted region over the full width of the sensor is the **depletion voltage**  $U_{depl}$ . It is, according to eq.3.10, proportional to the square of the sensor thickness. This value is of particular importance as it often defines the minimum operating voltage of a device.

A sensor is **overdepleted** if the bias voltage exceeds the depletion voltage,  $U_{ext} > U_{depl}$ .

The electric field caused by the space charge is at its maximum at the junction and is given by

$$E_{max} = 2V/W \approx \sqrt{\frac{2qN_D}{\epsilon_0\epsilon_{Si}} |U_{ext}|} = \sqrt{\frac{2}{\epsilon_0\epsilon_{Si}\mu\rho}} \cdot |U_{ext}| \quad (3.11)$$

for silicon sensors. The last equality replaces the doping concentration with the substrate resistivity, which are related via

$$\rho = \frac{1}{q\mu N_D}, \quad (3.12)$$

where  $\mu$  is the majority charge carrier mobility.  $E_{max}$  decreases linearly from the junction to the end of the space charge region, where it vanishes. [30]

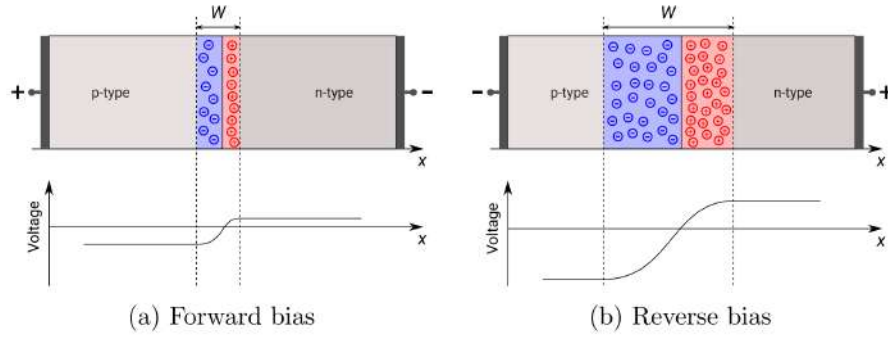


**Fig. 3.2** p-n diode under forward (a) and reverse (b) bias. [27]

### I-V characteristic and temperature scaling of the leakage current

The current of a diode in reverse bias is dependent on the external voltage, and is composed of several distinct components.

The first originates from the regions outside the depletion zone and is the result of the diffusion characteristics of minority carriers, whose density is exponentially dependent on the bias voltage. This current is calculated under the assumptions of an ideal diode, for which the following holds:

- The regions outside the depletion zone are neutral, and the boundary between regions is abrupt
- The charge carrier densities at the boundaries of the space-charge region are given by  $U_{bi} - U_{ext}$
- The low-injection condition holds, i.e. the density of injected minority carriers is much smaller than that of the majority carriers
- The net carrier generation and recombination in the depletion zone is zero and therefore the current across it constant.

Under these assumptions, the current of a diode is given by the **Shockley equation**

$$I_{ideal} = I_S (e^{\frac{qU_{ext}}{k_B T}} - 1), \quad (3.13)$$

where

$$I_S \approx qAn_i^2 \left( \frac{D_p}{N_D L_p} + \frac{D_n}{N_A L_n} \right) \quad (3.14)$$

is the **reverse-bias saturation current** with the junction area  $A$ , diffusion coefficients  $D_n$  and  $D_p$ , and diffusion lengths  $L_p$  and  $L_n$ .

For real, non-idealised detectors, two additional current sources must be taken into account. The first is the **surface current**, which is primarily caused by contamination or damage caused during the production or handling process. It is expected to scale linearly with the voltage and is assumed to be negligible within the context of this thesis.

The second and dominant contribution is the temperature-dependent **generation current** originating from the bulk volume. It stems from the thermal generation of electron-hole pairs in the depletion region and is given by

$$I_{gen} = qAw \frac{n_i}{\tau_g}, \quad (3.15)$$

where  $A$  is the area underneath the electrode.  $\tau_g$  is the charge carrier **generation lifetime**, which describes the time generated charge carriers need to return to the equilibrium state. The generation current depends on the temperature  $T$  since both  $n_i$  and  $\tau_g$  are temperature-dependent. The intrinsic carrier density  $n_i$  is strongly temperature-dependent via

$$n_i(T) \propto T^{3/2} \exp\left(-\frac{E_g}{2k_B T}\right). \quad (3.16)$$

The charge carrier generation lifetime  $\tau_g$ , on the other hand, can be approximated by considering that charges are generated most efficiently in traps close to the band gap energy  $E_g$ . The relevant trap energies therefore can be approximated by a single trap level  $E_t$ , for which

$$\tau_g = \frac{1}{N_t} \left( \frac{\exp\left(\frac{E_t - E_i}{k_B T}\right)}{v_{tp}\sigma_p} + \frac{\exp\left(\frac{E_t - E_i}{k_B T}\right)}{v_{tn}\sigma_n} \right), \quad (3.17)$$

where  $N_t$  is the trap density,  $v_{tn}$  and  $v_{tp}$  are the thermal velocities of the electrons and holes, respectively, and  $\sigma_n$  and  $\sigma_p$  their trapping cross-sections. Under the assumption that  $v_{tp}\sigma_p \approx v_{tn}\sigma_n$  and with  $v_t(T) \propto T^{1/2}$  [Chi1], [Chi2], this reduces to

$$\tau_g \propto T^{-1/2} \exp\left(\frac{E_t - E_i}{k_B T}\right). \quad (3.18)$$

Hence, the generation current scales with temperature via

$$I_{gen} \propto T^2 \exp\left(-\frac{E_a}{2k_B T}\right), \quad (3.19)$$

where  $E_a = E_g + 2(E_t - E_i)$  is the **activation energy** (also often referred to as **effective energy**  $E_{eff}$ ). The best-fit value for  $E_a$  found in literature is  $E_a = 1.21$  eV for silicon [Chi2].

The generation current is expected to increase with depletion depth. This means that it should increase until full depletion is achieved, and remain constant afterwards.

Taking into account the effects described above, the leakage current of a real, reverse-biased semiconductor is given by

$$I = I_{ideal} + I_{gen}. \quad (3.20)$$

### Breakdown voltage

Fig. 3.3 shows the voltage-dependent current of an ideal diode, which is given by eq. 3.13 for  $U > U_{BD}$ . The breakdown beyond  $U_{BD}$  is indicated with the dashed line. At reverse-bias voltages larger than  $|U_{BD}|$ , a sudden sharp increase in absolute current flow is observed. This breakdown is caused by two known mechanisms: the Zener effect, and the avalanche breakdown.

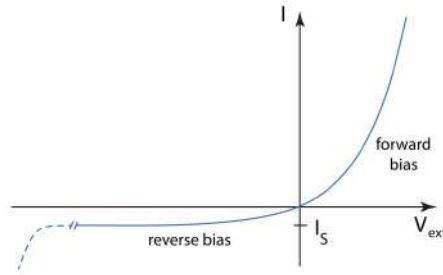


**Fig. 3.3** Current-voltage characteristic of an ideal diode. [26]

The **Zener breakdown** is caused by the movement of electrons from the valence band to the conduction band: at sufficiently high bias voltages, the occupied energy levels in the valence band of the p-type material match the unoccupied levels in the p-side conduction band. A potential barrier of height  $E_g$  and width  $E_g/q\mathcal{E}$  prevents uninhibited movement of electrons from the valence to the conduction band, where  $\mathcal{E}$  is the electric field of the potential barrier. Quantum-mechanical tunneling, however, allows electrons to cross over with a probability of

$$\Theta \approx \exp \left[ \frac{-4\sqrt{2m}E_g^{3/2}}{3q\hbar\mathcal{E}} \right]. \quad (3.21)$$

The Zener current can be estimated with

$$I_{\text{Zener}} \approx qA\mathcal{N}v\Theta, \quad (3.22)$$

where  $A$  is the cross section of the device,  $\mathcal{N}$  is the electron density, and  $v$  the electron velocity [24]. The tunneling probability increases for higher temperatures, and hence the Zener breakdown voltage decreases for larger temperatures.

An **avalanche breakdown** is induced by charge carriers that are sufficiently accelerated by the electric field in the depletion zone to generate new electron-hole pairs via impact ionisation. This process can form an avalanche of free charge carriers if the gain exceeds the absorption. The probability of inelastic scattering, which counteracts the avalanche process by limiting the amount of energy available for the creation of electron-hole pairs, increases with increasing temperature. As a result, the avalanche breakdown voltage increases for higher temperatures.

### 3.1.3 MOSFETs

Transistors, of which p-n junctions are a key component, are fundamental to modern electronics. Their main function is to control a current via an external voltage. The most common type of transistor is the metal oxide semiconductor field-effect transistors (MOSFET), which is composed of four terminals: a source, a drain, a gate, and a substrate. N- and p-doped materials can be combined into two basic types of MOSFET: the n-channel NMOS, and the p-channel PMOS. These are created by embedding two strongly doped source and drain regions in a lightly doped substrate, and placing a gate electrode over the area that separates them. The gate is insulated from the other terminals, typically by a thin layer of  $\text{SiO}_2$ . As a result, no current flow is possible between source and drain by default. The gate functions as a conductor between them: if the voltage applied between substrate and gate exceeds the threshold voltage at which the number of free electrons equals that of the holes in the substrate, i.e.  $U_{gs} > U_{th}$ , minority charge carriers accumulate below the insulator and form a conductive channel that allows for a current

flow  $I_{ds}$ . Depending on the applied voltages, the MOSFET can be operated in two distinct regimes:

- If  $U_{ds} < U_{gs} - U_{th}$ , the channel is ohmic and therefore  $I_{ds} \propto U_{ds}$ . This is the **linear region**.
- If  $U_{ds} \geq U_{gs} - U_{th}$ , the voltage is sufficiently high to drag the electrons towards the source. This creates a gradient in charge carrier concentration that is sufficiently steep to pinch off the channel at the drain when  $U_{ds} = U_{gs} - U_{th}$ . This regime is known as the **saturation region**.

Fig. 3.4 (a) illustrates the structure of MOS transistors.

NMOS and PMOS transistors can be implemented in a common substrate to form complementary CMOS transistors, which is shown in fig. 3.4 (b)

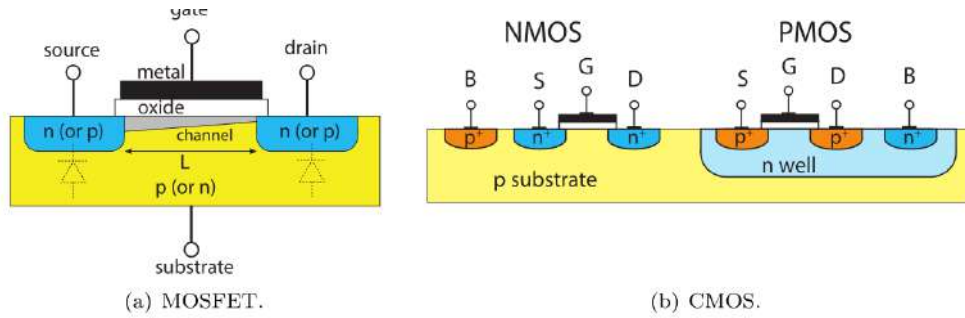


**Fig. 3.4** Basic structure of a MOSFET [26]

## 3.2 Pixel sensors

### 3.2.1 Signal generation

Silicon pixel sensors detect radiation by measuring the current that is generated when particles interact with their substrate: When an incident particle imparts sufficient energy to the substrate in the depleted region of a p-n junction, it can create a free electron-hole pair. The electric field across the junction separates the charge carriers and drifts them towards their respective collection electrodes, and the electron motion generates an electric current via induction. The current is described by the **Shockley-Ramo theorem**

$$I = \frac{q_0}{d} \mu_{n, p}(E(x)) \times E(x), \quad (3.23)$$

where  $\mu_{n, p}$  is the carrier mobility, and the field strength  $E$ , which depends on the depth  $x$  in the detector. A capacitance  $Q$  within the detector is charged by  $I$ , which results in a measurable voltage.

The mean energy deposited by an ionising particle is given by the Bethe-Bloch eq. 2.1. If the number of interactions is large enough for the central limit theorem to hold, i.e. for very thick sensors, the deposited energy is expected to follow a Gaussian distribution if the total energy loss is small compared to the original particle energy. For thinner sensors with a smaller number of interactions, on the other hand, a tail towards higher energies forms due to statistical fluctuations. Mathematically, this is described by a Landau distribution (see also Ch. 2).

The number of electron-hole pairs expected to be generated by a passing particle can be calculated by considering the amount of energy deposited in a sensor of given thickness, and the energy necessary to create an electron-hole pair. For a silicon sensor of 100  $\mu\text{m}$

thickness, the most probable energy deposited by a MIP is 30 keV [?]. With an average ionisation energy of 3.6 eV in silicon, this amounts to an estimated 8300 electron-hole pairs. Multiplying this with the electron charge of  $q_e \approx 1.602 \times 10^{-19}$  C, this corresponds to an expected charge of 1.3 fC.

### 3.2.2 Readout electronics

After a signal is generated in the p-n junction by a passing particle, it is routed to the sensor's readout electronics, amplified, and finally discriminated. The readout infrastructure can be implemented on either a separate Application-Specific Integrated Circuit (ASIC) or on the sensor substrate itself. Which sensor architecture is most suitable depends on e.g. the expected necessary radiation tolerance and required sensor size for the intended application. An overview of three types of pixel sensor commonly used in HEP is given below.

#### Hybrid pixel sensors

In hybrid pixel detectors, the charge-detecting sensor chip and the readout chip containing the front-end electronics are separate entities. Each sensor pixel is coupled to a corresponding readout pixel via an electrode, which typically take the form of solder bumps. The chips are created in a commercial CMOS process and joined using *flip chip* technology.

This approach allows for the individual optimisation of charge collection and processing. As the sensor chip merely contains the sensor diodes, it is possible to apply high bias voltages without compromising the readout infrastructure. The full thickness of the substrate can therefore be exploited as a detection volume, which makes for an excellent signal yield. A major disadvantage to the two-chip process, however, is the large amount of material involved: the process of connecting two chips requires a certain rigidity of the material, which necessitates a thicker layer of silicon. Two wafers also means double the thickness, on top of the material added by the bump bonds themselves. All this means a thicker layer of material for particles to pass through, and reduces the resolution by increasing the chances of multiple scattering. Aside from physics considerations, budgeting concerns must also be taken into account as the bump bonding process is quite expensive and difficult.

#### Monolithic Active Pixel Sensors (MAPS)

Unlike hybrid pixel detectors, where the sensor element and readout electronics are located on separate chips, monolithic pixel detectors combine the infrastructure for charge collection and signal processing within the same substrate. The in-pixel readout is implemented by implanting wells of varying doping in the bulk substrate, such that each sensor pixel contains both dedicated signal amplification and digitisation circuits. Merely the configuration, monitoring, and input/output circuitries are relegated to the chip periphery.

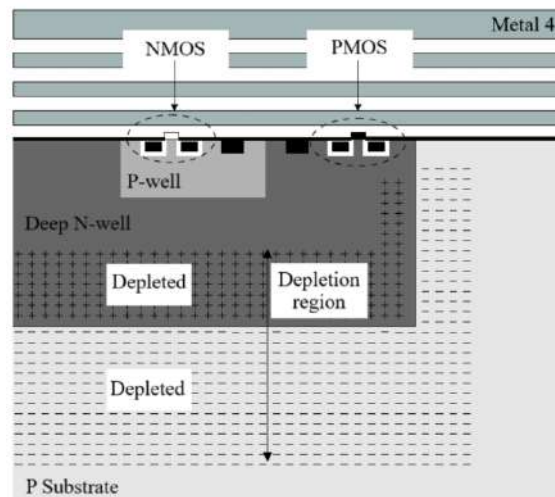
Compared to hybrid pixel sensors, this approach avoids the costly bump-bonding process and significantly reduces the material budget: not only is the second chip made redundant, the remaining chip can also be thinned since it is no longer necessary for the material to be sufficiently rigid for bonding. An additional advantage is the lower power consumption.

Like hybrid sensors, MAPS are commonly produced in commercial CMOS processes and therefore benefit from a lower production cost than for custom manufacturing. The commercial production process, however, comes with the disadvantage that the MAPS substrate can not be biased to very high voltages. This leads to a smaller depletion zone and therefore poorer signal yield. The limited bias voltage also means that the charge carriers

are largely collected via diffusion rather than drift, which reduces the time resolution and further lowers the signal yield and radiation tolerance as not all charges are expected to be collected in time – or at all, given that some additional signal loss may occur due to trapping processes, which are at least somewhat counteracted by high bias voltages.

### HV-MAPS detectors

The limitations to the commercially produced MAPS sensors can be remedied by constructing the pixels in a way that allows for strong biasing, effectively combining the advantages of the hybrid sensor and MAPS technologies. For a p-type substrate, this is done by embedding a lowly doped deep n-well within the p-substrate, such that it is insulated from biased regions. PMOS transistors are in direct contact with the deep n-well, while NMOS transistors are surrounded by an additional shallow p-well. This type of floating structure is visualised schematically in fig. 3.5. It allows for the implementation of complex CMOS readout circuits within the deep n-well that can be used for signal amplification and processing. At the same time, this nested architecture ensures that the substrate can be safely biased to high voltages, enabling large depletion depths and fast charge collection via drift. The collection time is shortened from the order of  $\mu\text{s}$  (for diffusion) to ns, the radiation tolerance increased, and a sensor thickness of  $50\ \mu\text{m}$  can be achieved.



*J. Perić. Nucl. Instrum. Meth. A, 582:876-885, 2007.*

**Fig. 3.5** Floating logic. [25]

Fig. 3.6 illustrates the full detector concept for four pixels. It should be noted that there are no insensitive areas between the pixels as their depletion zones overlap.

HV-MAPS are manufactured in commercial HV-CMOS processes that were originally developed for use in, for example, the automotive industry.

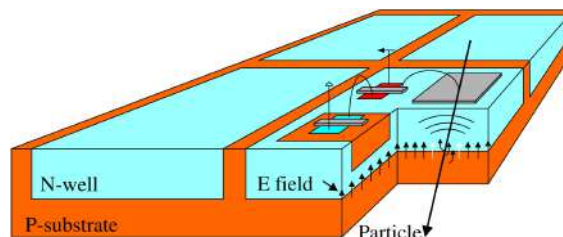


**Fig. 3.6** HV-MAPS concept [25]

### 3.2.3 Electronic noise

Current and voltage in electronic circuits are subject to fluctuations, primarily due to three physical sources:

**Thermal noise** is caused by Brownian motion and therefore increases with temperature, as well as quadratically with the sensor capacitance.

**Shot noise** is a result of the statistical fluctuations in the number of charge carriers capable of overcoming a potential barrier. It is directly proportional to the current in the system.

**1/f noise** is a widespread phenomenon that is thought to potentially be of a fundamental statistical origin. In MOSFETs, the primary cause is the trapping of charge carriers in the transistor channel. Like thermal noise, it is expected to increase quadratically with the sensor capacitance.

In pixel detectors, these noise sources can impact e.g. the amplifier output, the threshold, and the baseline of the comparator. Fluctuations in these components may cause an accidental crossing of the threshold and lead to noise hits. [26]

# Chapter 4

## ATLASPix 3.1

The ATLASPix 3.1 (AP3.1) is one of several HV-MAPS detectors currently under investigation in the HEP community. It was developed by the ATLAS collaboration with the intention of using it as part of their inner tracker.

### 4.1 Sensor architecture

As a HV-MAPS sensor, the AP3.1 is structurally separated into two sections: a pixel matrix containing the active pixel cells responsible for the recognition and pre-processing of hits, and a periphery containing the readout circuitry tasked with generating relevant hit information. The sensor layout is shown in fig. 4.1.

#### 4.1.1 Active pixel matrix

The pixel matrix consists of 49,104 pixels, each measuring  $150 \times 50 \mu\text{m}^2$ . The pixels are arranged in 132 columns and 372 rows, covering an active area of  $19.8 \text{ mm} \times 18.6 \text{ mm}^2$ .

At the core of each pixel is a charge-collecting diode that acts as the sensing element. It is accompanied by in-pixel electronics, which includes a PMOS charge-sensitive amplifier (CSA) that amplifies each charge pulse, a source follower (SF) stabilising the signal, an NMOS comparator which digitises the analogue amplifier output, and Random-Access Memory (RAM) circuitry storing the value of both the individually tunable in-pixel threshold and that of a mask bit to disable the pixel in question.

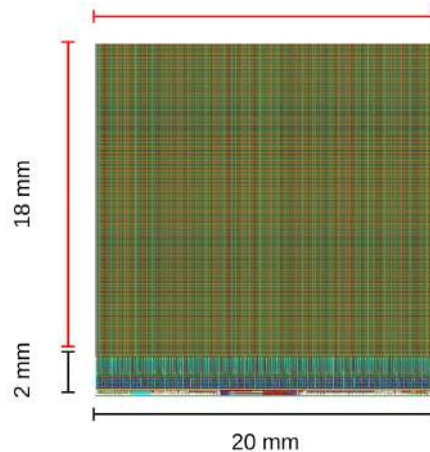


**Fig. 4.1** Layout of ATLASPix 3 with the pixel matrix at the top, and the periphery at the bottom. [36]



threshold voltage. The threshold voltage is determined by two DAC values: a global threshold  $Th$  applied to all pixels, and a 3-bit tune DAC  $TDAC$  by which the global threshold can be shifted on an individual basis to correct for pixel-to-pixel variations. The range of applicable TDAC values can be specified using the DAC parameter  $VNDAC$ . The threshold is typically chosen such that noise signals are suppressed. If the signal height exceeds the threshold voltage, the comparator outputs a rectangular pulse whose high and low levels are determined by the externally supplied voltages VDD and VMinus, respectively.

### 4.1.2 Periphery

The resulting digital signal is sent to the periphery along the columns by the line driver, where each pixel has a dedicated readout cell containing a receiver and a hit buffer. The readout cells are arranged in a double-column structure and equip each signal with the relevant hit information. This includes the digital hit address assigned to each pixel, as well as the timestamps of the leading and trailing edges of the incoming comparator signal. The timestamps are stored in the hit buffer of each readout cell and are used to reconstruct the time of arrival (ToA) and time over threshold (ToT) of a hit. The latter describes the duration of each signal and is discussed in detail in section 4.2. The input level of the receiver can be tuned using the DAC parameters  $VNBiasRec$  and  $VPBiasRec$ .

Before the hits are sent to the DAQ system, they are assembled and processed by the final state machine (FSM) located in the sensor periphery.

### 4.1.3 Readout scheme

The ATLASPix 3.1 can be operated in two readout modes, which are each implemented as a separate circuit.

In the untriggered readout mode, the the hit information of each pixel within a given column is shifted to a single end-of-column structure, which handles the subsequent processing, at a rate of one hit per column per FSM readout cycle. This occurs simultaneously for each column containing non-empty hit buffers. From there, the information is 8b/10b aurora-encoded by the FSM and subsequently sent to the DAQ system at a nominal rate of 1.28 GBit/s.

In the triggered readout mode, the hit information of up to 80 hits per column is stored together in a single content-addressable memory (CAM) trigger buffer. If a trigger with a matching timestamp is found in the trigger table containing the timestamps of external trigger events, the hits in the trigger buffer are collectively sent to an EoC structure for further processing by the FMS. The hits are 64b/66b aurora-encoded and finally sent to the DAQ system.

A schematic of the ATLASPix 3.1 readout structure is provided in fig. 4.3.

All measurements presented in this work were taken using the untriggered readout mode. The DAQ infrastructure used to process the data is described in detail in Ch. 6.1.1.

### 4.1.4 Test outputs

Dedicated test circuits offer direct access to the amplified analogue pulses of row-0 pixels via the *AmpOut* test line, as well as to the digitised comparator outputs of each pixel column using the *HitBus* test output. These test signals can be observed using an oscilloscope, which acts a window to the raw signals during various processing stages.

The signal response of each pixel can be tested using artificial pulses injected into its analogue circuit. This is implemented using the capacitor  $C_{inj}$ , which discharged into the

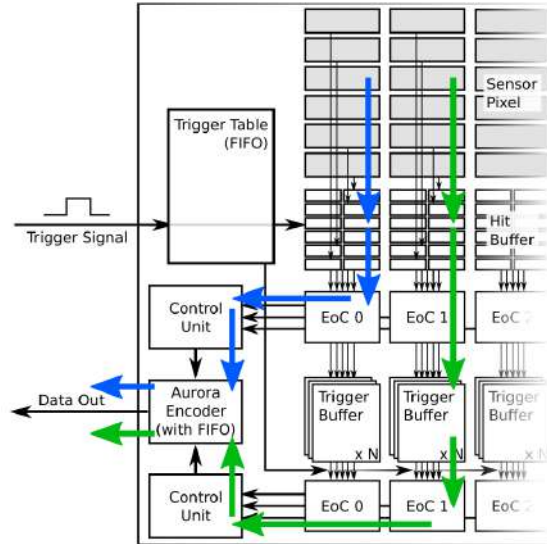


**Fig. 4.3** Schematic of the ATLASPIX 3.1 triggered and untriggered readout schemes [19]

pixel n-well. The strength of an injection pulse is controlled using VDAC parameter  $Inj$ . Alternatively, the injection pulse can be generated using an external pulse generator.

## 4.2 Time over Threshold

The digitisation of an analogue signal pulse is an essential step in the signal processing chain of a pixel detector. In the ATLASPIX 3.1, this task is accomplished by a comparator, which compares the incoming amplified signal to a threshold commonly custom-set to reduce noise. The comparator outputs a high level for as long as the signal height exceeds the threshold, such that the resulting signal is a rectangular pulse with a height given by the high level supplied to the comparator. The duration of the signal is known as the Time-over-Threshold (ToT), and is given by the time difference between the leading (TS1, or ToA) and trailing (TS2) edges of the comparator output,

$$\text{ToT} = \text{TS2} - \text{TS1}. \quad (4.1)$$

For a given threshold, the ToT is dependent on the pulse height of the signal. Since signal amplitude is determined by the amount of charge arriving at the CSA, the ToT contains information about the energy spectrum of impinging particles. The energy dependence of the ToT may not be linear due to saturation effects in the amplifier circuit.

## 4.3 Breakdown voltage

While the term *breakdown* most commonly refers the Zener breakdown and the avalanche breakdown mentioned in Ch. 3.1.2, it is believed that this is not the effect observed in the ATLASPIX 3.1 since the observed breakdown occurs far below the nominal value of approx. 120 V, and does not develop as abruptly as expected. Instead, the breakdown mentioned throughout this thesis is hypothesised to be an effect within the pixel structure itself, where sufficiently strong fields could conceivably lead to local charge avalanches. This is, however, just a hypothesis; further studies are required to determine both the precise location and cause of the observed breakdown.

# Chapter 5

## Radiation damage

The high density, low ionisation energy, and short drift pathways in silicon semiconductors result in a high detection resolution and makes this type of detector a popular choice for tracking and vertexing in HEP. At the particle fluences necessary for HEP experiments, however, the environment is inherently high in radiation and can damage the sensor over time, limiting the lifetime of such detectors.

The mechanisms via which radiation can damage a silicon detector can broadly be classified into two categories: non-ionising (NIEL) and ionising energy loss (IEL). Both can occur anywhere in the detector, but because the detector is structurally different in its bulk than at the surface and at the interfaces between the silicon and the SiO<sub>2</sub>, the impact of the two energy loss types on distinct parts of the detector differs. While the electronics close to the surface of silicon devices primarily suffer from ionising radiation, the bulk structures are mainly subject to effects related to NIEL. Macroscopically, these damage processes affect detector properties like the leakage current, breakdown voltage, and signal strength. The study of these characteristics is therefore an essential tool for understanding the behaviour of silicon detectors in high-radiation environments, and for testing their viability under the necessary conditions.

The following chapter outlines the mechanisms involved in the radiation damage seen in silicon semiconductor detectors and provides an overview of the expected changes in detector behaviour, as well as of the implications for detector operation.

### 5.1 Substrate damage

The ionisation of the substrate volume by impinging particles is a mostly reversible process and, indeed, part of the detection mechanism employed by silicon detectors (see also Ch. 2). IEL processes are therefore not expected to cause permanent damage to the bulk of the detector volume. Particles interacting directly with the atomic nuclei of the silicon lattice, however, can cause various forms of displacements that lead to altered sensor characteristics by changing the electrical properties of the substrate. The fraction of NIEL interactions leading to lattice-altering displacements depends on the energy of the impinging particle; the majority of the energy dissipates in the form of phonons and does not damage the detector.

The primary source of substrate damage are high-energy hadrons and leptons, where charged particles Coulomb-scatter off atomic nuclei, and neutrons interact with the nuclei via elastic and inelastic scattering. These interactions can lead to the displacement of lattice atoms if the imparted energy exceeds a threshold energy of  $E_d \approx 25$  eV, the energy at which lattice atoms are displaced with a probability of 50% [26]. The energy of the

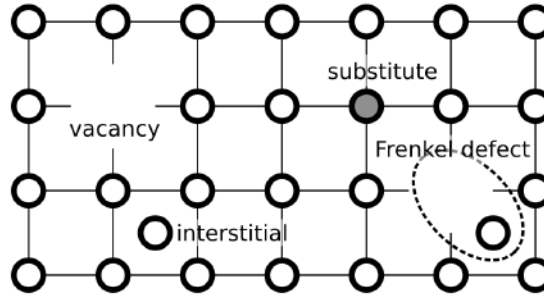


**Fig. 5.1** Different types of point defects caused by impinging radiation. [26]

resulting **primary knock-on atoms** (PKA) determines the specific type of defect created: **Primary point defects** include unoccupied lattice positions (**vacancies**), atom in inter-lattice positions (**interstitials**), combinations of vacancies and interstitials (**Frenkel defect**), and the substitution of a lattice atom with atoms of a different element. Fig. 5.1 illustrates these different types of point defect.

The maximum energy that can be transferred to a recoil atom via elastic scattering by a particle of mass  $m_P$  and a kinetic energy of  $E_P$  is given by

$$E_{R, max} = 4 E_P \frac{m_P m_{Si}}{(m_P + m_{Si})^2}. \quad (5.1)$$

As a consequence, the minimum energy needed for the production of a Frenkel pair in silicon is  $\sim 185$  eV for neutrons, and  $\sim 255$  keV for electrons. As vacancies and interstitials are very mobile in the silicon lattice at  $T > 105$  K, the majority ( $\sim 60\%$  [26]) of Frenkel defects produced above this temperature recombine before causing permanent damage to the detector. The remaining defects can migrate through the lattice and may become trapped at impurities and defects. In HEP experiments, the energy imparted by impinging nuclei can feasibly exceed the displacement threshold energy of the impacted lattice atoms by multiple orders of magnitude, and hence the recoiling PKA itself can create further defects along its path via the same mechanisms as mentioned above. For high-energy particles, **defect clusters** consisting of a concentrated accumulation of defects can develop along the direction of impact and at the end of a PKA's recoil range.

### 5.1.1 Annealing

If the vibrational energy of the crystal lattice exceeds the binding energy of a defect, the defect can become mobile. The mobility of defects increases with their thermal energy and can have both beneficial and damaging consequences for the detector: a defect migrating through the crystal lattice can recombine with its counterparts and undo traps and changes to the energy level caused by the defect. On the short term, such annealing processes can recover some of the damage sustained by the sensor. On longer time scales, however, more complex stable defects can form and permanently damage the detector. A more detailed description of the relevant annealing mechanisms can be found in the corresponding sections in Ch. 5.1.3.

### 5.1.2 NIEL Hypothesis

Particle fluences are often cited in literature in terms of **1 MeV neutron equivalents**, or **1 MeV n<sub>eq</sub>**. This approach normalises radiation damage caused by any particle to the damage created by an equivalent fluence  $\phi_{eq}$  of 1 MeV neutrons, and builds on the assumption that any substrate damage sustained by a detector scales linearly with the NIEL and the amount of primary defects caused by it. Under this **NIEL hypothesis**,

the distribution of the defects over energy and space is of no consequence for the outcome of the irradiation.

NIEL can be quantified using

$$\left. \frac{dE}{dx} \right|_{\text{NIEL}}(E) = \frac{N_A}{A} D(E), \quad (5.2)$$

where  $N_A$  is the Avogadro constant and  $A$  the atomic mass of the target material. The **damage function**  $D(E)$  depends on the particle type and its energy, and is given by

$$D(E) = \sum_i \sigma_i(E) \int_{E_d}^{E^{max}} f_i(E, E_R) P(E_R) dE_R, \quad (5.3)$$

where  $E$  and  $E_R$  denote the kinetic energies of the impinging and the recoiling particle, respectively. For 1 MeV neutrons,  $D(E)$  corresponds to 95 MeV mb. [26] Fig. 5.2 shows the damage function for a neutrons, protons, pions, and electrons in an energy range between  $10^{-1}$  and  $10^4$  MeV.

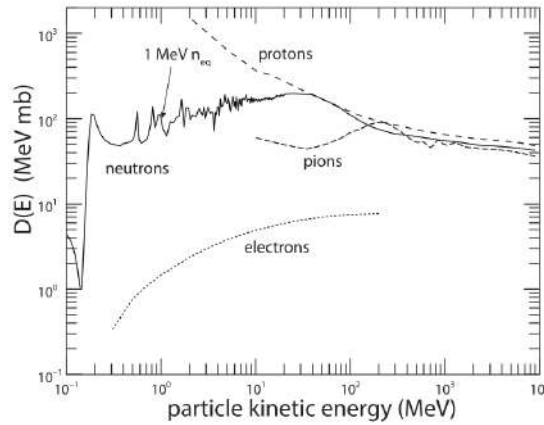


**Fig. 5.2** Damage function for atom dislocations in a silicon lattice for different particles. [26]

Particle fluences  $\phi$  can be converted to their 1 MeV neutron equivalent using

$$\phi_{eq} = \kappa \phi, \quad (5.4)$$

where

$$\kappa = \frac{\int_{E_{min}}^{E_{max}} D_x(E) \phi(E) dE}{D_n(1 \text{ MeV}) \int_{E_{min}}^{E_{max}} \phi(E) dE} \quad (5.5)$$

is the **hardness factor**.

### 5.1.3 Effect of substrate damage on sensor properties and implications for detector operation

Defects in the silicon lattice alter its electrical properties at the damage sites, resulting in a deterioration of macroscopic detector characteristics. The majority of these effects can be attributed to the introduction of additional energy levels within the band gap. The influence on the sensor is largely determined by the type of generated defect centre

and the position of its energy level in the band gap, and boils down to three affected key characteristics of the sensor: its depletion voltage, the leakage current, and the signal strength.

The impact on the detector performance is commonly quantified within the framework of Shockley-Read-Hall (SRH) statistics, which provides a mathematical description of the generation-recombination processes undergone by defects that interact with the conduction and valence bands. Given knowledge about the capture cross sections for holes and electrons, the type of defect, its concentration, and its position in the band gap, SRH statistics make it possible to calculate the theoretical impact of each defect. A detailed breakdown of this framework can be found in [14].

### Depletion voltage

Defects with energy levels close to the valence or the conduction band act as donor and acceptor centres. Their presence changes the **effective doping concentration**

$$N_{\text{eff}} = N_D - N_A \quad (5.6)$$

of the substrate, potentially to the point of type inversion.

The radiation-dependent change in effective doping concentration is given by the **stable damage factor**

$$N_C(\phi) = N_{C,0}(1 - e^{-c\phi}) + g_c\phi \quad (5.7)$$

[17], where  $\phi$  is the fluence of the impinging radiation and  $c$  is known as the **material-dependent removal constant**.

As the reverse-bias voltage necessary for full detector depletion is proportional to the effective doping concentration,

$$U_{\text{dep}} = \frac{q|N_{\text{eff}}|d^2}{2\epsilon\epsilon_0}, \quad (5.8)$$

these defects have an impact on the depletion voltage. With an increase in  $N_{\text{eff}}$ , the voltage necessary to achieve full detector depletion approaches — and eventually exceeds — the breakdown voltage of the sensor. To avoid risking a diode breakdown, the sensor must therefore be operated in partial depletion once a certain effective doping concentration has been reached. As a consequence, the amount of collected charge and therefore the signal strength is expected to decrease as the total irradiation fluence increases.

Fig. 5.3 below shows the depletion voltage and the effective doping concentration as a function of the radiation fluence for an FZ<sup>1</sup> n-type silicon detector [22].

---

<sup>1</sup> Float-zone silicon is a type of pure silicon produced by heating silicon wafers to create a molten zone in which impurities are removed. FZ silicon is generally more resistant to radiation damage than silicon produced in competing processes. [26]

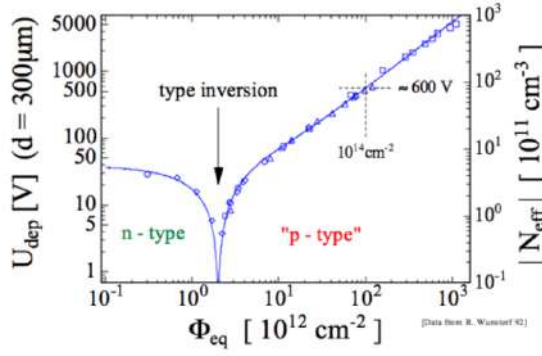


**Fig. 5.3** Fluence dependence of depletion voltage and effective doping concentration. [22]

For p-type devices – like most HV-MAPS detectors – in particular, the radiation-dependent change in  $N_{\text{eff}}$  manifests as an **acceptor removal** effect. Microscopically, this is caused by the transformation of electrically active shallow acceptors into defect complexes that no longer act as acceptors. Analogously to eq. 5.7, the acceptor removal-specific fluence-dependence of  $N_{\text{eff}}$  can then be parameterised using

$$N_{\text{eff}}(\phi_{\text{eq}}) = N_{A,0} \exp(-c_A \phi_{\text{eq}}) + g \phi_{\text{eq}}, \quad (5.9)$$

where  $c_A$  is the **acceptor removal coefficient** and  $g$  the **introduction rate**, which covers all other radiation-induced space charge generation mechanisms. It should be noted that  $c_A$  is, in fact, dependent on the initial acceptor concentration, and that the exponential function does not take into account defect kinetics. [31]

The effective doping concentration in a series of  $n^+ - p$  diodes produced on epitaxial silicon wafers were measured for different substrate resistivities as a function of proton and neutron fluence in [31] and are shown in fig. 5.4, where the dashed lines represent fits to the data following eq. 5.9. The acceptor removal coefficient resulting from these fits are shown in fig. 5.5 as a function of the initial doping concentration  $N_{\text{eff},0}$ .

It was found that the acceptor removal process is faster and stronger for irradiation with protons than neutrons, indicating a heavy involvement of point defects [31].

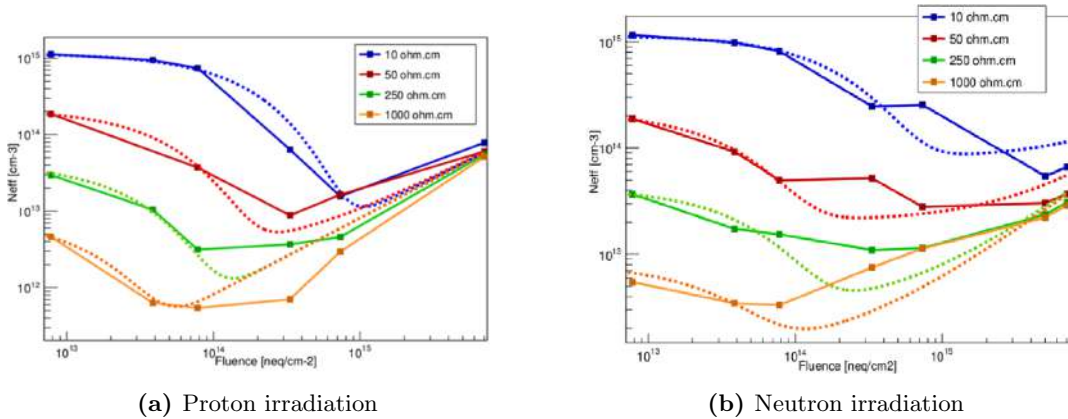


**Fig. 5.4** Effective doping concentration for p-type diodes made from epitaxial silicon with various resistivities as function of fluence. [31]

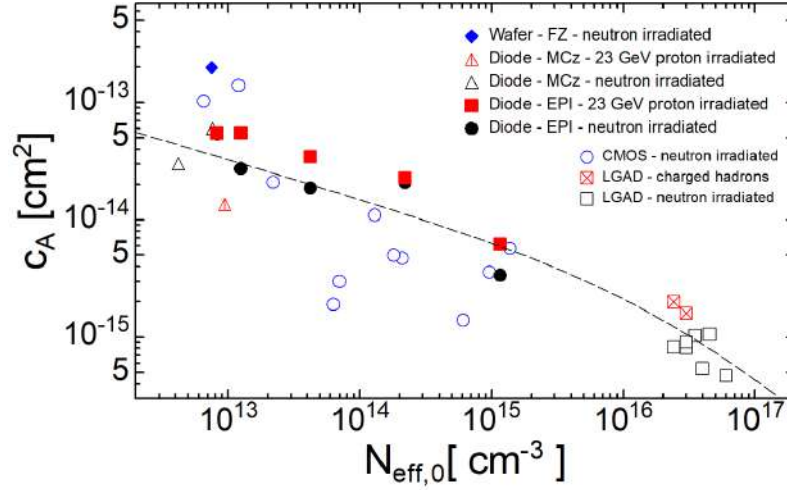


**Fig. 5.5** Acceptor removal coefficient as a function of initial doping concentration for p-type silicon sensors. [31]

Changes to the effective doping concentration can occur even after the irradiation of a sensor. This highly temperature-dependent annealing process can be both beneficial and detrimental to the detector. Mathematically, the effect is parameterised using two additional components  $N_a$  and  $N_y$ , where  $N_a(\phi, T_a, t) = g_a \phi \exp(-t/\tau_a)$  describes the **short-term** or **beneficial annealing**, and  $N_y(\phi, T_a, t) = g_y \phi (1 - \exp(-t/\tau_y))$  the **reverse annealing**, with space charge introduction rates  $g_a$  and  $g_y$ . The time constants  $\tau_a$  and  $\tau_y$  are depend on the annealing temperature  $T_a$  and have been found to follow the Arrhenius eq. [14].

Taking into account the stable damage factor (eq. 5.7), the total change to the effective doping concentration adds up to

$$\Delta N_{\text{eff}} = N_a(\phi, T_a, t) + N_y(\phi, T_a, t) - N_C(\phi). \quad (5.10)$$

### Leakage current

Defects close to the middle of the band gap increase the probability of electron-hole pair generation by serving as midway points between the valence and conduction bands, and function as generation or recombination centres. The higher generation rate of charge carriers contributes to the leakage current. This leads to an increase in detector noise and can, in a worst-case scenario, potentially create a feedback loop ("thermal runaway"), which can ultimately destroy a detector.

The radiation-induced increase of the leakage current is directly proportional to the fluence  $\phi_{\text{eq}}$  of the impinging radiation and is independent of the material properties of the silicon [14].

$$I_{\text{vol}} = I_{\text{vol}, 0} + \alpha \phi_{\text{eq}} V \quad (5.11)$$

Eq. 5.11 quantifies this proportionality, where  $V$  is the volume under the electrode, and  $\alpha$  is known as the **current-related damage factor**. It was observed in [21] that for radiation producing mainly point defects, the fluence-dependency of the leakage current deviates from the linear proportionality and instead becomes strongly dependent on the impurity content. For photon irradiation, this corresponds to a quadratic dependency on the photon fluence, and is predominantly influenced by the oxygen concentration in the silicon lattice [21].

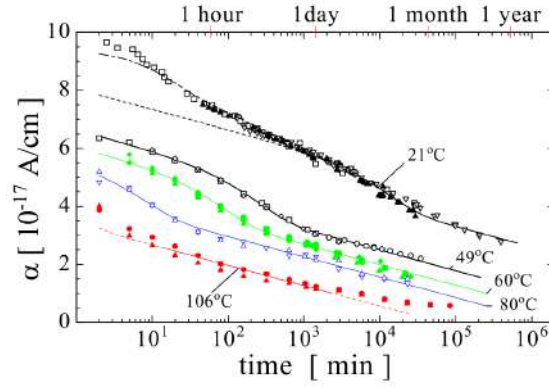


**Fig. 5.6** Evolution of current-related damage factor  $\alpha$  with annealing time. Figure taken from [13]

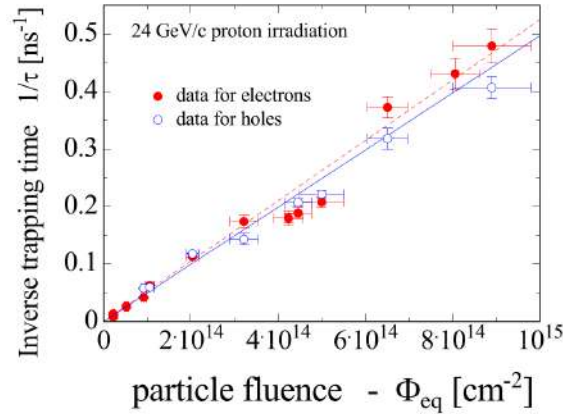


**Fig. 5.7** Dependence of inverse trapping time on particle fluence. Figure taken from [13]

It was shown in [18] that the current-related damage factor is subject to annealing effects and decreases over time. The observed behaviour can be parameterised using a combination of an exponential and a logarithmic term,  $\alpha = \alpha_1 \cdot \exp(-t/\tau_1) + \alpha_0 - \alpha_2 \cdot \ln(t/t_0)$ . It is believed that the exponential part can be attributed to defect dissociation. The logarithmic component, however, still lacks a physical explanation [18]. Fig. 5.6 shows the time evolution of  $\alpha$  at several different annealing temperatures.

Since the leakage current generated in the substrate volume is also inherently dependent on the temperature (recall eq. 3.19  $I(T) \propto T^2 \exp(-E_a/2k_bT)$ , see Ch. 2), cooling is an essential tool for the operation of irradiated sensors that prevents their premature destruction and significantly lowers the noise during operation.

### Charge collection efficiency and signal strength

Defects can trap drifting charge carriers before they are collected. If the timescale of re-emission is longer than the shaping time of the electronic signal, the trapped electron or hole can only create a delayed signal that contributes to the noise level, while the original signal suffers a charge collection deficiency.

The effective trapping time  $\tau_{\text{eff}}$  is inversely proportional to the particle fluence  $\phi_{\text{eq}}$ ,

$$1/\tau_{\text{eff}} = 1/\tau_{\text{eff}, 0} + \beta\phi_{\text{eq}}, \quad (5.12)$$

where  $\tau_{\text{eff}, 0}$  is the carrier lifetime before radiation, and  $\beta$  is the **effective trapping constant**. Fig. 5.7 illustrates this relationship for both holes and electrons.

As both the trapping probability  $1/\tau_{\text{eff}}$  and defect concentration grow with increasing particle fluence, the SNR of a detector is expected to deteriorate over time. For high-

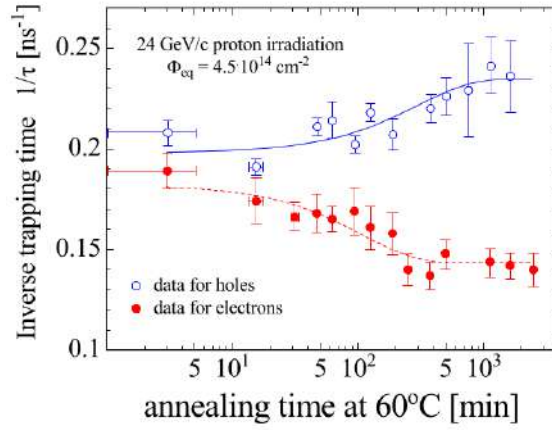


**Fig. 5.8** Dependence of inverse trapping time on annealing time. Figure taken from [13]

fluence applications, charge trapping becomes the limiting factor for detector operation [14].

After irradiation, annealing processes have an impact on the effective trapping time that markedly differs for electrons and holes: while  $1/\tau_{\text{eff}}$  decreases for electrons, it increases for holes [13]. This translates to less electron-, and more hole-trapping over time. Fig. 5.8 shows this behaviour.

It has been shown that the trapping time is only weakly temperature-dependent.

## 5.2 Surface damage

Impinging particles displacing atoms in NIEL-processes are of little relevance to  $\text{SiO}_2$  since the oxide structure is inherently amorphous. Damage to the surfaces of silicon detectors are therefore expected to be largely caused by IEL. Unlike in the substrate bulk, where IEL is mostly reversible and actually part of the detection process, ionisation can permanently alter the detector material at the interfaces. The cumulative amount of energy deposited in the detector volume via ionising radiation is referred to as the **Total Ionising Dose** (TID) and is commonly measured in units of gray, where  $1 \text{ Gy} = 1 \text{ J/kg}$ . TID damage predominantly impacts the readout circuitry and causes threshold shifts, increased leakage current, changes in sensor parameters, and unwanted parasitic currents between transistors. The damage can largely be traced back to the formation of positive charges in the gate oxide, which is caused by two separate effects.

One significant source of the change in oxide charge are the high electric fields of the MOS transistors: any charge carriers created via ionisation are separated by the fields and prevented from immediately recombining. Because the capture cross section of holes by shallow levels in the silicon oxide is large, their mobility within the oxide is very low. The effect is exacerbated by their own lattice potential, which creates local lattice dislocations that move alongside the hole itself. If the gate bias is positive, the holes move towards the Si-SiO<sub>2</sub> interfaces and remain there due to the large number of mismatch-induced oxygen vacancies. As the mobility of electrons in the SiO<sub>2</sub> is a factor of  $\sim 10^6$  higher than that of holes, they can eventually leave the gate oxide; the trapped holes, however, generate a positive space charge in the oxide.

The second element contributing to the formation of a positive oxide charge is the lattice mismatch between the Si and SiO<sub>2</sub>. The OH<sup>-</sup> atoms saturating the dangling bonds of trivalent silicon atoms are easily separated by radiation. The outer electrons left dangling can then be removed by scattering off other electrons, leaving behind a hole.

As a result of the positive oxide charge, the threshold voltage of transistors can be altered

such that conductive channels underneath the gate become either permanent (as is the case for nMOS transistors, where the threshold voltage decreases) or harder to form (for pMOS transistors, where the threshold voltage increases). Ultimately, this can prevent transistors from switching.

Aside from changing the oxide charge, the separation of the  $\text{OH}^-$  can also lead to further trapping of electrons or holes from the silicon bulk. The resulting charge accumulation in the oxide layers can reduce the efficiency for signal detection, as well as increase the leakage current of the detector.

Despite the existence of some knowledge about the mechanisms behind surface damage, these effects are highly dependent on the foundry and the bias conditions during the irradiation. A rigorous theoretical framework to quantify and predict the outcomes of TID damage is difficult to achieve and as such, results are heavily reliant on experimental observations. [23]

# Chapter 6

## Measurement Infrastructure

### 6.1 DAQ systems and measurement infrastructure

#### 6.1.1 GECCO readout system

The processing of the hit data collected by the ATLASPix sensor requires a dedicated DAQ infrastructure. The framework used for the measurements presented in this work is the GECCO (GEneric Configuration and Control) [45] system developed by Felix Ehrler and Rudolf Schimassek at the Karlsruhe Institute of Technology. Its hardware is distributed across three physically separable boards: the DUT (Device Under Test) carrier board housing the ATLASPix sensor itself, the GECCO board through which the power is supplied, and an FPGA (Field-Programmable Gate Array) responsible for all tasks related to sensor configuration and data processing.

An overview of the assembled GECCO setup is shown in fig. 6.1.

The DUT carrier board to which the ATLASPix 3.1 is bonded also contains the shift registers used to write the desired configuration to the sensor. In addition, several probe pins connected to the external voltages are implemented for testing purposes.

The necessary voltages are supplied to the sensor using the GECCO board, which is connected to the carrier board via a PCIe  $\times$  64 connector. Additionally, it contains the LVDS receivers used to facilitate communication between the sensor and the FPGA. [19] The FPGA used within the scope of this thesis is a commercial Artix-7 housed on a Nexys video development board. It is connected to the GECCO board via a low pin-count FPGA Mezzanine Card (LPC-FMC) connector.

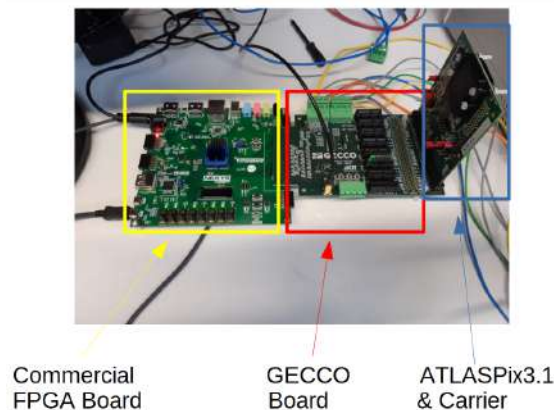


**Fig. 6.1** GECCO readout system [36]

### 6.1.2 PCIe power adapters

As the low voltage power connections of the AP 3.1 are implemented in the PCIe interface of the motherboard, the low voltages are typically supplied via the GECCO carrier board introduced in section 6.1.1. The layout of the full readout system is, however, unsuitable in test settings where spatial constraints must be taken into account.

While sensor configuration of the AP 3.1 is only possible with a dedicated DAQ environment like the GECCO system, to simply supply the low voltages it is sufficient to connect the power supplies to the appropriate PCIe terminals via an adapter.

In order to meet the geometric requirements at the Bonn Isochronous Synchrotron introduced in section 6.2.2, several custom-made power adapters catering to different prospective experimental layouts were commissioned to and produced by the electronics workshop at the Heidelberg Institute of Physics. Two iterations are shown in fig. 6.2, the first of which was used during the initial proof-of-principle irradiation campaign described in Ch. 9.2. Its successor (shown in fig. 6.2 b) features a greatly improved stability, and was used in all measurements involving the cooling setup described in section 6.1.4 that did not specifically require the use of the data readout provided by the GECCO DAQ system.

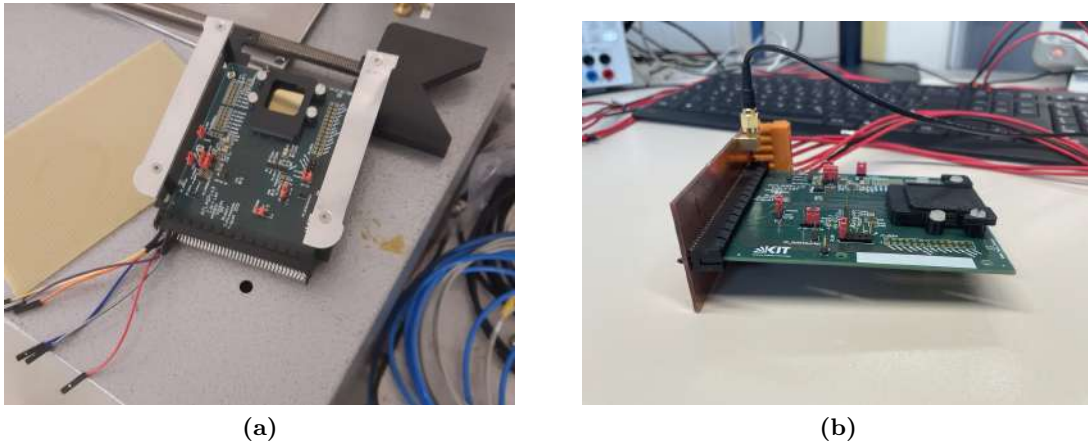


**Fig. 6.2** Custom-made PCIe power adapters for the ATLASPix 3.1

### 6.1.3 PixMon slow control system

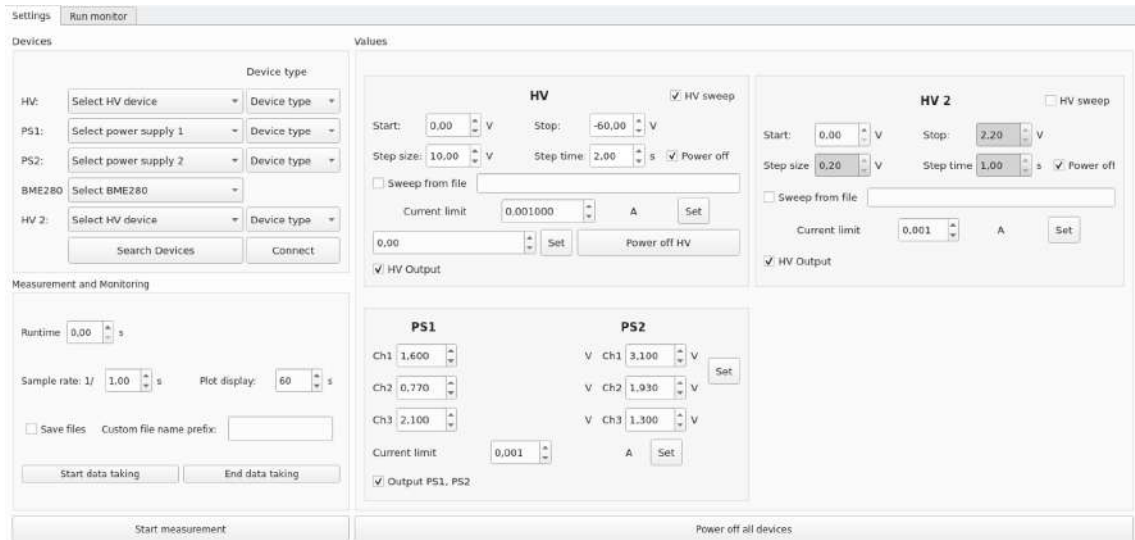
The slow control software **PixMon** ("PixelMonitor") was built to enable continuous remote monitoring and control of the ATLASPix currents and voltages. It is currently implemented to simultaneously read and control up to four power supplies, including source measure units from the Keithley 2600 and 2200 series, and the Rohde & Schwarz HMP4000 power supply series.

In addition to the communication with power supplies, PixMon is capable of monitoring ambient conditions using an Adafruit BME280 sensor for temperature, relative humidity, and pressure measurements.

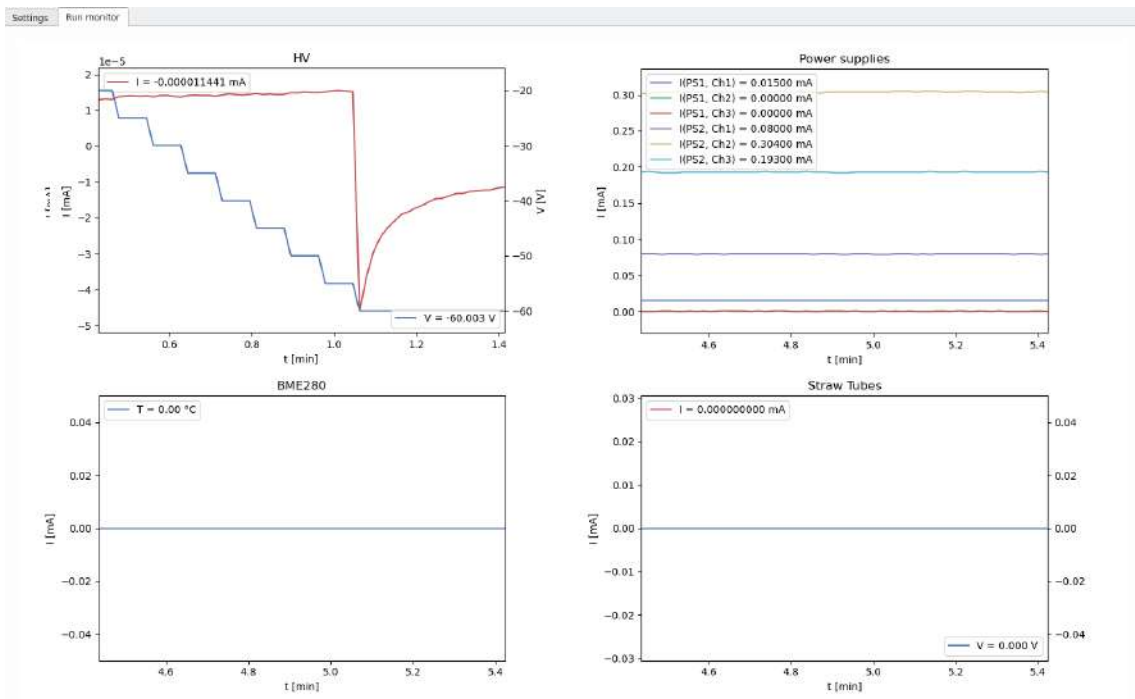
Screenshots of the PixMon user interface are shown in fig. 6.3.

### 6.1.4 Cooling setup and temperature monitoring

The damage sustained by a silicon pixel sensor after irradiation can lead to an increase in noise due to the increased leakage current. As the leakage current is temperature-dependent (see Ch. 5), cooling the sensor can reduce the noise and ensure that it remains operational.



(a)



(b)

Fig. 6.3 User interface of the PixMon slow control system



(a)



(b)

**Fig. 6.4** Cooling setup at Heidelberg University

Additionally, radiation-induced defects have the potential to self-heal via annealing (see Ch. 5), which is a process that is accelerated at higher temperatures. Considering that a rigorous study of radiation damage effects requires a damaged sensor to remain in the damaged state for as long as possible, it is necessary to prevent annealing via cooling.

To achieve this, dedicated cooling infrastructure was built in a laboratory at Heidelberg University. Irradiated samples can be stored and operated in an ELCOLD laboratory freezer capable of cooling to  $-40$  °C. To ensure that the sensor is operated in a dry environment, a custom cooling box with sufficient space for desiccant bags was 3D-printed (shown in blue in fig. 6.4). The box is equipped with an Adafruit BME 280 sensor that allows for the remote monitoring of the conditions inside. The PCIe connector of the ATLASPix motherboard extends through a slot in the sensor cooling box and remains accessible, allowing for full sensor operation using the GECCO system. A separate box (clear box in fig. 6.4) housing the FPGA and GECCO carrier board protects the readout infrastructure from the conditions inside the freezer.

## 6.2 Particle sources

The MightyPix sensor proposed for the upgrade-II LHCb inner tracker is expected to be exposed to a large amount of both ionising and non-ionising radiation. The successful implementation of the detector requires a good understanding of the sensor response to different radiation types. To simulate the expected radiation environment in a testbeam and tabletop setting, a number of different particle sources are employed and their impact on the DUT studied.

### 6.2.1 X-ray tube

X-ray tubes produce photons in the X-ray spectrum by accelerating electrons in a vacuum. These are generated by cathode filaments, which releases the electrons via thermionic emission when heated. The electrons are accelerated towards an anode by a high voltage applied between the cathode and the anode, where their collision with the anode material can produce X-rays via two mechanisms:

Bremsstrahlung photons are created when an electron loses kinetic energy in the electric field of matter, and the energy difference is carried away in the form of photons. The resulting spectrum is continuous, with a maximum energy given by the kinetic energy of the impinging electrons.

Photons with a characteristic spectrum are emitted when an inner shell electron in the anode material is ejected by impinging radiation, and the resulting hole is subsequently filled by an outer shell electron. The energy difference between the shells is compensated for by the emission of a photon.

As a result, the observed X-ray spectrum is the superposition of a continuous Bremsstrahlung spectrum and a characteristic spectrum, and depends on both the anode material and the strength of the accelerating voltage.

All X-ray measurements carried out within the scope of this thesis were performed using a PHYWE XR 4.0 X-ray tube, set to the maximum available acceleration voltage of 35 kV. The anode current of the device can be adjusted between 0.01 and 1 mA in increments of 0.01 mA. The device is equipped with three different anode materials — tungsten, copper, and molybdenum —, as well as a range of collimators of different sizes and materials.

The X-ray setup is located at Heidelberg university and shown in fig. 6.5.



**Fig. 6.5** X-ray setup at Heidelberg University. This setup was used for all X-ray measurements presented in this thesis.

### 6.2.2 Proton beam at the Bonn Isochronous Cyclotron

Unlike photons, which are expected to cause only IEL damage, protons can damage a pixel detector via both IEL and NIEL. To study the combination of both damage mechanisms in an ATLASPix 3.1, it was irradiated with protons at the Isochronous Cyclotron operated by the Helmholtz Institute for Radiation and Nuclear Physics in Bonn.

The Bonn Isochronous Cyclotron can provide protons in an energy range between 7 and 14 MeV/nucleon and has a typical beam diameter of  $< 1$  cm. The beam parameters are measured at extraction using an online monitoring system.

An insulated DUT box is mounted on a 2D motorstage and can house a DUT with a maximum size of  $19 \times 11$  cm<sup>2</sup>. A built-in nitrogen gas line allows for the cooling and drying of the DUT. The temperature inside the DUT box is continuously monitored via two NTC thermistors. A picture of the beam area is shown in fig. 6.6.



**Fig. 6.6** Beam area of Bonn Isochronous Cyclotron

The beam is aligned using a combination of fluorescence screens, cameras, and a beam monitor. The DUT is irradiated by row-wise scanning, with rows separated by a distance of  $\Delta y \approx 1$  mm. The beam velocity  $v$  is adjustable and typically on the order of 70 mm/s. Homogeneous irradiation of the DUT is ensured by overscanning the DUT; a schematic of the scanning pattern is provided in fig. 6.7.

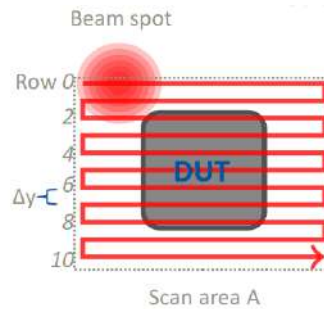


**Fig. 6.7** Scanning pattern of proton beam at Bonn Isochronous Cyclotron [40]

The resulting proton fluence is given by

$$\phi_p = \frac{I_{\text{beam}}}{q_e \cdot v \cdot \Delta y} \quad (6.1)$$

and is associated with an uncertainty on the order of  $\sqrt{3}\%$ . [40]

### 6.2.3 $^{55}\text{Fe}$

To evaluate the signal response of the ATLASPix 3.1, an  $^{55}\text{Fe}$  source was employed as a signal source.

The radioactive isotope  $^{55}\text{Fe}$  decays into  $^{55}\text{Mn}$  via electron capture and with a half-life of 2.74 years. While the dominant decay product of this process is an Auger electron, the electron cannot leave the source due to its low energy of 5.2 keV. Within the scope of this thesis,  $^{55}\text{Fe}$  can therefore be considered a monoenergetic source emitting photons with an energy of 5.9 keV. [41]

The source used for the measurements presented in this work has an estimated activity of 250 kHz/sr [36].

## Chapter 7

# Simulating LHCb rates with a tabletop X-ray tube

The mean particle rate in the prospective LHCb MightyTracker is expected to be on the order of  $125 \text{ kHz/mm}^2$  in the hottest region. For the prospective MightyPix sensor to be a viable detector candidate for its innermost region, it must therefore be able to cope with a hit rate of around  $50 \text{ MHz/chip}$ . To study the sensor performance under such conditions, it is proposed to use an X-ray tube to operate the ATLASPix setup at high rates in a tabletop laboratory environment.

As a proof-of-principle measurement to confirm that the rate capability of the Heidelberg X-ray tube introduced in Ch. 6.2.1 matches the rate of operation required of the MightyPix, the rate of emitted photons was determined as a function of the X-ray anode current. Given that there is no currently implemented method of measuring the photon rate of the X-ray tube using an independent system, it was determined using the ATLASPix 3.1 itself.

The premise behind the measurement is simple: the number of photons arriving within a well-defined window of time is counted, and subsequently divided by the size of the time bins. A bin size of  $25 \text{ ns}$  is chosen since the clock of the readout used during this measurement runs at a speed of  $40 \text{ MHz}$ , making the size of a single timestamp the most natural unit of time available.

As the emission of the X-ray photons is expected to follow a Poisson distribution, the hit distribution is validated with a series of statistical cross-checks described in section 7.3.

### 7.1 Setup

The radiation-sensitive depleted volume of the pixel matrix is located closer to the front side of the AP 3.1, which has a thickness of  $600 \mu\text{m}$ . To minimise signal loss from the conversion of photons in the insensitive bulk area of the silicon, it is therefore desirable to orient the chip with its front side facing the beam. Due to the geometric constraints of the readout infrastructure, which includes the GECCO readout system in addition to an FPGA, the sensor was placed at a distance of around  $30 \text{ cm}$  from the beam exit. To protect the sensor periphery from radiation, two  $2 \text{ mm}$  collimators were placed between sensor and beam exit.

A schematic of the setup is provided in fig. 7.1, along with the hitmap of a beamspot in fig. 7.2.

All rate measurements were made using a tungsten anode, and at an anode rate between

0.01 mA and 1 mA.

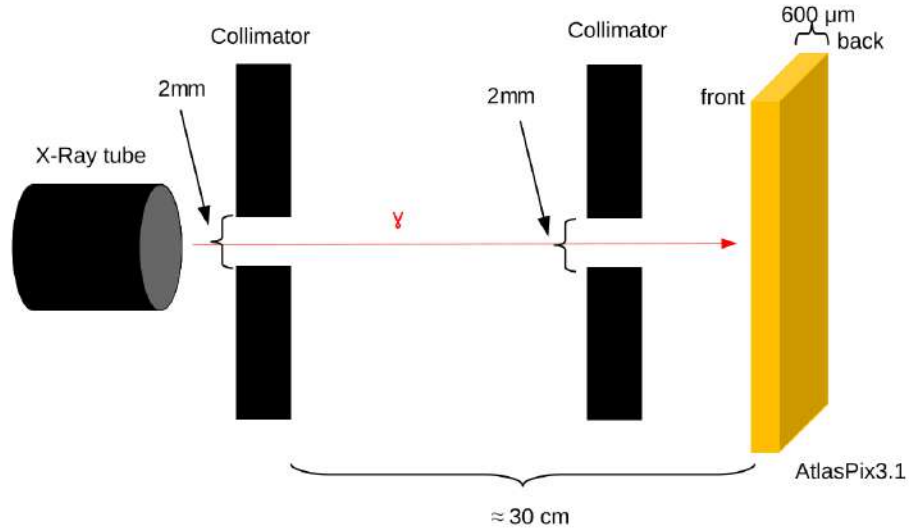


**Fig. 7.1** Schematic of the X-ray setup [36]

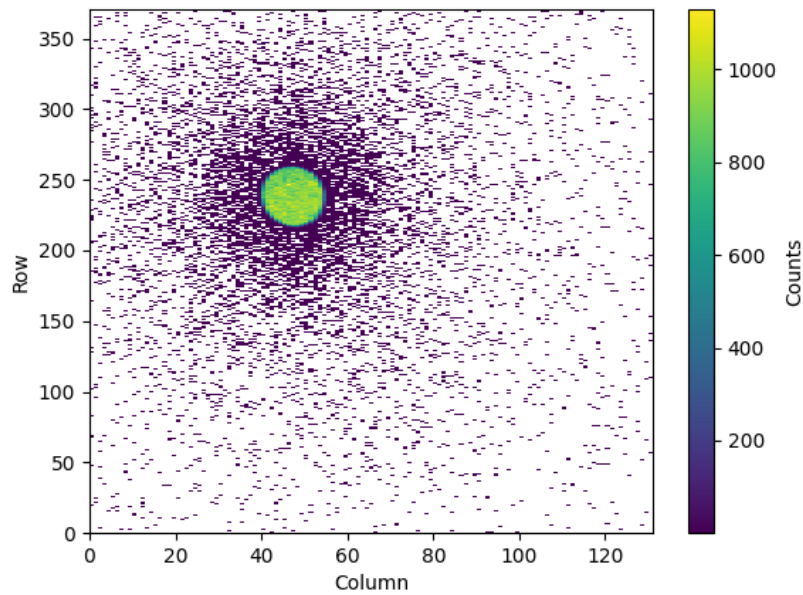


**Fig. 7.2** Hitmap of a beamspot. Measurement performed using a 2 mm collimator and a tungsten anode.

## 7.2 Cluster corrections

It is expected that a subset of photons can trigger hits in multiple adjacent pixels due to charges diffusing into the depleted regions of neighbouring pixels. A second effect that can lead to single impinging photons appearing as multiple hits is crosstalk along the transmission lines between pixel matrix and periphery.

For a hit rate measurement to accurately reflect the number of photons converting in the depletion zone, it is therefore necessary to correct for multi-hit clusters — where a cluster is defined as any collection of hits that appear within the same timestamp, and that are spatially distributed along adjoining pixels — that originate from a single photon. As there are otherwise no known features that unambiguously distinguish charge sharing and

crosstalk events from physical hits, the spatial distribution of such clusters plays a decisive role in inferring the origin of a hit: While crosstalk is expected to occur only along columns due to the implementation of the readout structure, charge sharing can trigger connected hits across both columns and rows. As the likelihood for charge sharing increases the closer a traversing particle is to a pixel border, the occurrence of such events along rows and columns is expected to reflect the pixel geometry. Given that an ATLASPix pixel has a height of  $50 \mu\text{m}$  and a width of  $150 \mu\text{m}$ , a charge sharing ratio of 1:3 is expected along rows vs. along columns. For the same reason, the size of clusters originating from charge sharing is not expected to exceed 2 pixels.

To determine whether all clusters can be assumed to originate from single photons, a dedicated analysis investigating their spatial distribution was carried out.

Of the  $\lesssim 0.5\%$  of events that were found to be multi-hit clusters, no three-event clusters were found along rows. This matches the expectation given that only charge sharing, which should have a maximum cluster size of two, is thought to occur along rows. It was further found that  $> 80\%$  of clusters extend along columns, which is consistent with the 1:3 row-to-column ratio expected for charge sharing under the assumption that the excess hits along columns are caused by crosstalk. If all assumptions holds true, it can be inferred from the  $\sim 20\%$  of multi-hit clusters along rows that  $60\%$  of all multi-hit clusters occur along columns due to charge sharing, leaving  $20\%$  of all multi-hit clusters to crosstalk. It can therefore be broadly estimated that multi-hit clusters caused by charge sharing outnumber those caused by crosstalk at a ratio of 4:1.

As the the spatial distribution of all identified clusters is consistent with either charge sharing or crosstalk, a cluster correction is applied to all X-ray rate measurements under the assumption that all adjacent hits appearing within the same timestamp can be traced back to a single photon.

### 7.3 Sanity checks

The number  $n$  of events that is expected to occur during a specified time interval when the rate of occurrence  $\theta$  is constant is given by the Poisson distribution

$$P(n) = \theta^n \frac{e^{-\theta}}{n!}. \quad (7.1)$$

Assuming that photons are emitted by the anode of the X-ray device in a random fashion, the number of photons arriving within a given timeframe is therefore expected a Poisson distribution [39]. As a result, the distribution of photons recorded for each timestamp can serve as a cross-check for systematic effects such as a potential saturation of the sensor readout or instabilities of the X-ray tube.

Figure 7.3 is used to visualise this concept and shows the distribution of the number of photons arriving within each time bin at an anode current of 0.9 mA. As the data was taken using the hit-driven readout of the AP 3.1, empty time bins are not recorded and the number of bins with zero hits is not known a priori. While it is possible to improve statistics by inferring the number of bins with no entries from the number of timestamps missing in the data between the first and last recorded hit, it was observed in several spot checks that a Poisson fit with this additional information agrees within 2% with the fit without the first data point. The difference is deemed negligible and therefore this additional step is omitted going forward.

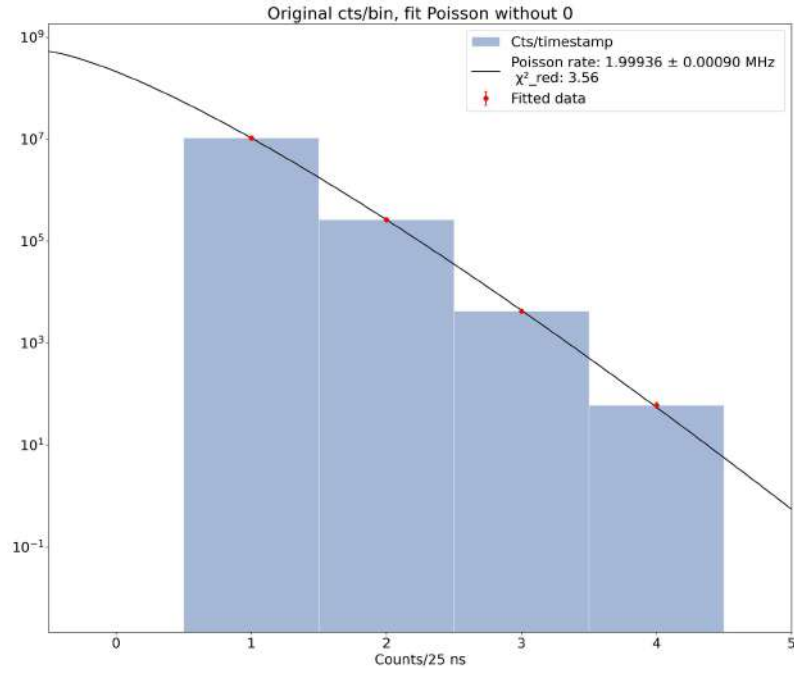


**Fig. 7.3** Distribution of the number of photons arriving within a single timestamp bin of 25 ns.

The process described above is used to validate the random nature of photon arrival for X-ray anode currents in the full available range of 0.01 to 1 mA. The data was corrected for multi-hit clusters following the approach introduced in section 7.2 prior to the Poisson fit.

Fig. 7.4 shows the reduced  $\chi^2$  statistic for the applied fits. The Poisson distribution was found to agree well with data taken across all photon rates, with no systematic deviations observed.

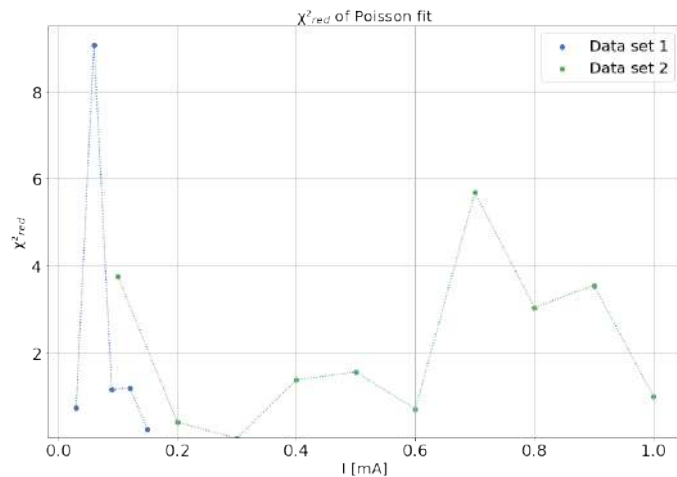


**Fig. 7.4** Reduced  $\chi^2$  statistic of Poisson fit applied to the distribution of photons arriving within 25 ns time bins as a function of the anode current. Two data sets with measurements taken on different days are included.

It is a property of Poisson-distributed random counts described by eq. 7.1 that the time between events  $x$  is described by an exponential function

$$f(x) = \theta e^{-\theta x}, \quad (7.2)$$

where  $\theta$  is the expected constant rate of occurrence [39]. This mathematical peculiarity can be exploited to serve as an additional cross-check for unexpected effects like readout dead time.

The fit function given by eq. 7.2 was applied to the distribution of timestamps between hits, an example of which is shown in fig. 7.5. Overall, it was found that the time constant  $\theta$  of the exponential fit matches that resulting from the Poisson fit. A closer look, however, reveals an excess of counts in the first five to ten timestamps. As is shown in fig. 7.6, which visualises the deviation between the observed number of timestamp between hits and the number expected from the applied fit as a function of the anode current, this effect is less pronounced at higher rates <sup>1</sup>.

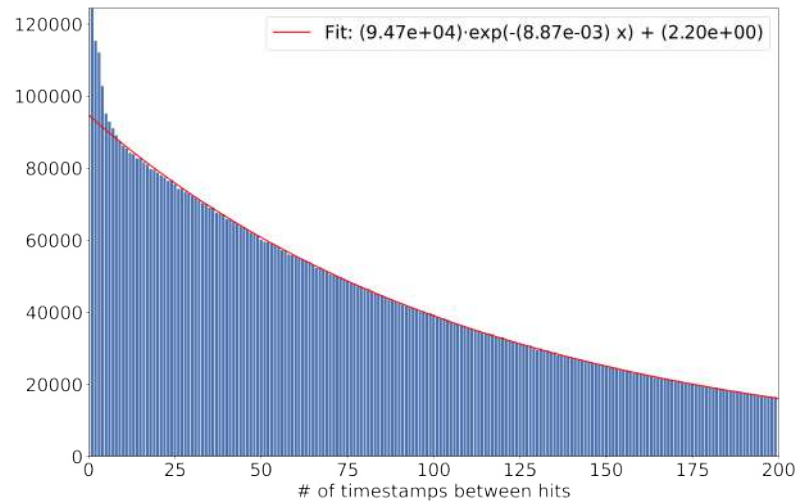


**Fig. 7.5** Distribution of timestamps between hits. Data taken with an X-ray anode current of  $I_{anode} = 0.1$  mA.

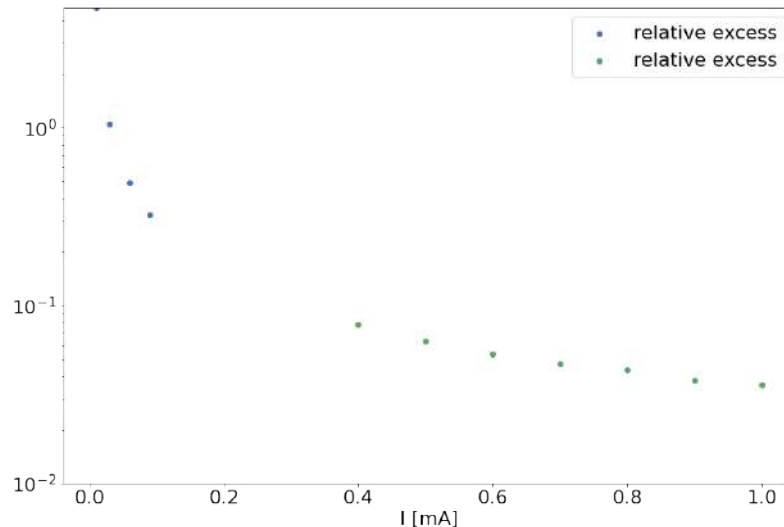


**Fig. 7.6** Deviation of number of observed timestamps between hits from expectation deriving from fit

An analysis of the spatial distance between the excess counts in question shows that the overwhelming majority of hits appearing in neighbouring timestamps have an absolute pixel-to-pixel distance of 1, and are predominantly located in the same column and in adjacent rows. This is reflected in the single peak in the column distance and the double

<sup>1</sup> As is shown in 7.4, the photon rate scales linearly with the anode current.

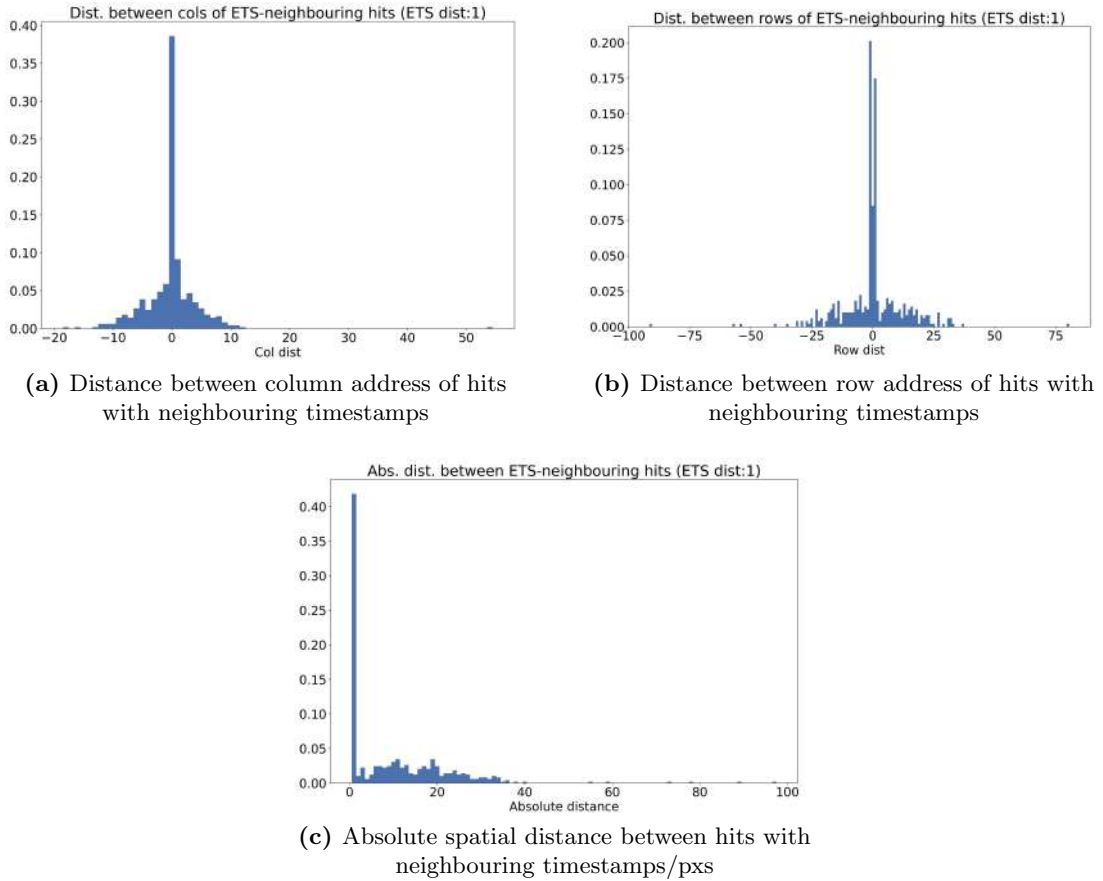


**Fig. 7.7** Spatial distribution of hits in neighbouring timestamps

peak in the row distance seen in the the example of the spatial distribution analysis shown in fig. 7.7.

While the origin of the observed excess has not been conclusively identified at this point, the spatial distribution of the hits in question is consistent with charge sharing. Given that the hits are recorded across multiple timestamps, this observation implies that spatially adjacent hits appearing up to ten timestamps apart should be considered part of the same cluster, and be corrected for accordingly.

## 7.4 Achievable hit rate

After correcting for multi-cluster hits following the approach described in section 7.2<sup>2</sup>, the hit rate measured with the AP 3.1 is found to scale linearly with the X-ray anode. As seen in fig. 7.8, two fits were applied for the two measurement series taken on different days and for different anode current ranges. Bearing in mind that the sensor response is more reliable at lower hit rates<sup>3</sup>, it may be assumed that the fit through data set 1 is more accurate. Given the resulting fit function of

$$\text{Rate} = 2.4 \cdot 10^{-3} \times I_{\text{anode}} - 0.009 \text{ MHz}, \quad (7.3)$$

in the beam spot, which has an area of  $3.8 \text{ mm}^2$ , the hit rate at the maximum anode current

<sup>2</sup> It should be mentioned that the insights regarding the large temporal dispersion of clusters across multiple timestamps came after the analysis presented in this section was completed and was therefore not taken into account.

<sup>3</sup> This was studied in detail in [36] and can be attributed to readout limitations.

of 1 mA is determined to be around 630 MHz/mm<sup>2</sup>. This exceeds the expected LHCb rate of 125 kHz/mm<sup>2</sup> by a factor of five and confirms the viability of the X-ray tube as a high-rate tabletop setup capable of matching the rate expected for the MightyPix.

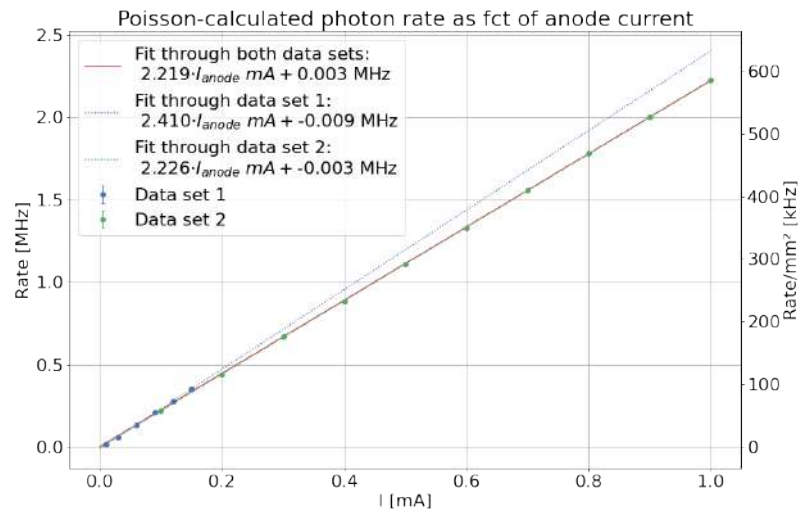


**Fig. 7.8** Poisson-calculated photon rate as function of anode current

## Chapter 8

# Energy calibration of the ATLASPix 3.1

As described in Ch. 4.2, the ToT of a signal created in the depleted area of an ATLASPix 3.1 by an impinging particle is related to the particle's energy. Since the energy dependence of the ToT depends on the function of several electronic in-pixel components like the CSA and the comparator, monitoring for changes in the ToT response of a sensor can serve as a measure for radiation damage sustained by the in-pixel electronics. While an energy calibration can in theory also be achieved using only the in-pixel injection pulses, the processing of charges deposited by physical sources involves the entire chain of operation in a more realistic setting.

Within the scope of this thesis, the Heidelberg X-ray tube introduced in Ch. 6.2.1 is investigated regarding its suitability as a particle source for energy calibrations. As an accurate assessment of a detector's energy response requires knowledge of the amount of energy deposited in its sensitive volume, the expected energy spectrum of photons originating from different anodes (Cu, Mo, W) and filtered through different collimators (Ni, Zr) is studied. Given that an energy calibration is easiest to achieve using monenergetic sources, suitable anode-collimator combinations are found and used in conjunction with a  $^{55}\text{Fe}$  source for a test calibration.

### 8.1 Setup

The energy spectrum of radiation detected by a silicon detector depends not only on the size of its sensitive volume, but also on the amount of bulk material the radiation must traverse before reaching and subsequently converting in the sensitive area.

While the depletion depth of the fully biased ATLASPix 3.1 sensors used for the work presented in this thesis was not measured in laboratory setting and has not been conclusively determined, it is roughly estimated to be around  $50\ \mu\text{m}$  [42]. To experimentally assess the energy spectrum of the photons expected to convert in the radiation-sensitive depleted area, the radiation was sent through silicon bulk material of various thicknesses and recorded using a Geiger-Müller counter. The energy resolution was obtained by exploiting the relationship between the wavelength  $\lambda$  of light and the incidence angle  $\theta$  of the X-ray beam on a crystal lattice with a grating constant  $d$ , which — according to Bragg's law — leads to constructive interference only if

$$2 \cdot \sin(\theta) = n \cdot \lambda, \tag{8.1}$$

where  $n \in \mathbf{N}$ . The energy as a function of the incidence angle is then given by

$$E(\theta) = \frac{hc}{2 \cdot d \cdot \sin(\theta) \cdot q_e}. \quad (8.2)$$

Using a LiF crystal mounted on a goniometer, the X-ray beam was collimated through a 2 mm collimator and the photon rate recorded as a function of a changing incidence angle using a Geiger-Müller counter.

To approximate the spectrum of photons that is expected to convert within the depleted zone of the ATLASPIX 3.1, the incident beam was filtered through silicon bulk material of varying thickness. This was achieved by taping an increasing number of discarded silicon sensors to a collimator. The difference between spectra obtained through different bulk layers corresponds to the spectrum of the radiation that converted in the intermediate bulk material.

The approach is visualised in Fig. 8.1, where X-ray photons originating from a molybdenum anode were sent through 100  $\mu\text{m}$  of silicon.

Due to the fragile nature of the thinned sensors used as bulk material, the minimum thickness of the chips that could be reliably taped to the collimator — and therefore the closest approximation to the depleted zone of a fully biased ATLASPIX 3.1 — was 100  $\mu\text{m}$ .

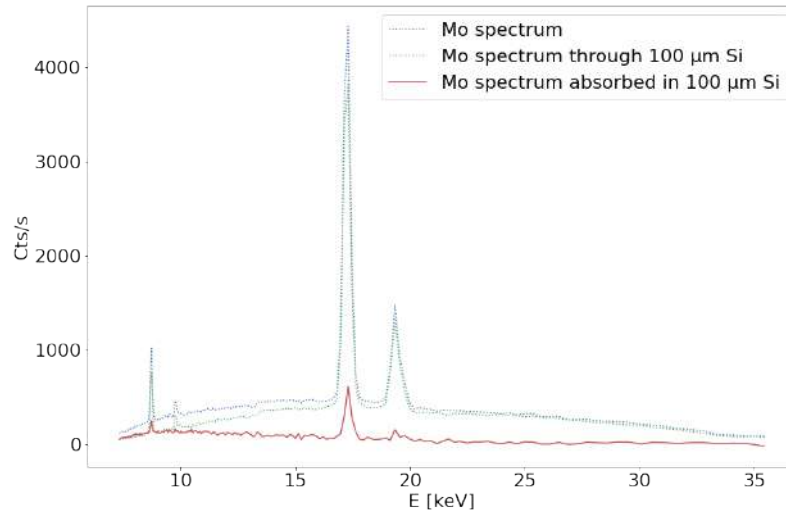


**Fig. 8.1** X-ray spectra from a molybdenum anode recorded with and without 100  $\mu\text{m}$  intermediate silicon bulk material.

## 8.2 Expected energy spectrum of X-ray photons

It was found for all three anodes used that while filtering the radiation through nickel and zirconium filters almost fully suppresses the Bremsstrahlung spectrum of the photons, leading to a spectrum with clearly defined energies, the remaining peaks of the characteristic spectrum were also heavily reduced. It was determined that the silicon bulk material itself removes a sufficient portion of the Bremsstrahlung spectrum without also sacrificing the signal-to-noise ratio to forgo the use of filters altogether for the energy calibration discussed in section 8.3. The resulting spectra in 100  $\mu\text{m}$  silicon are shown in fig. 8.2, along with the energies of the primary characteristic lines for each anode.

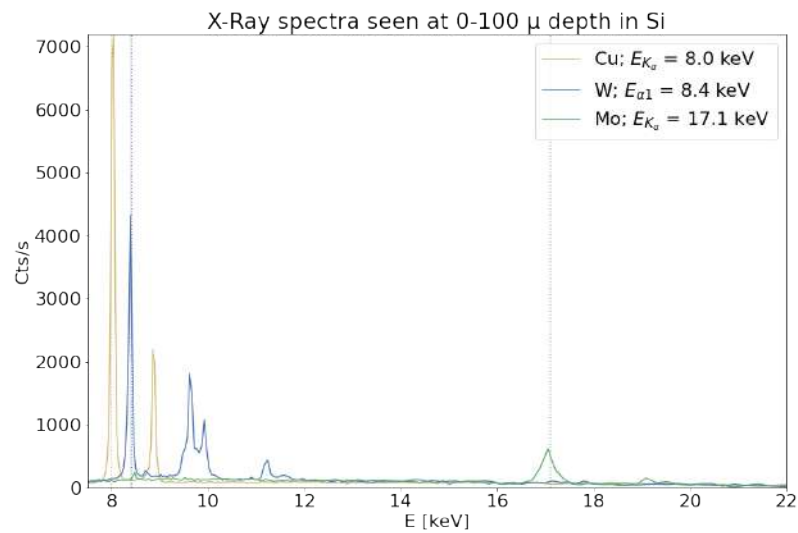
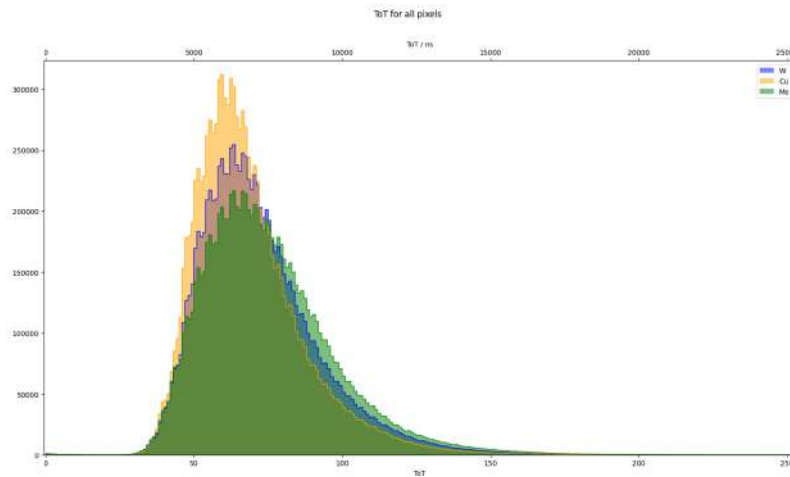


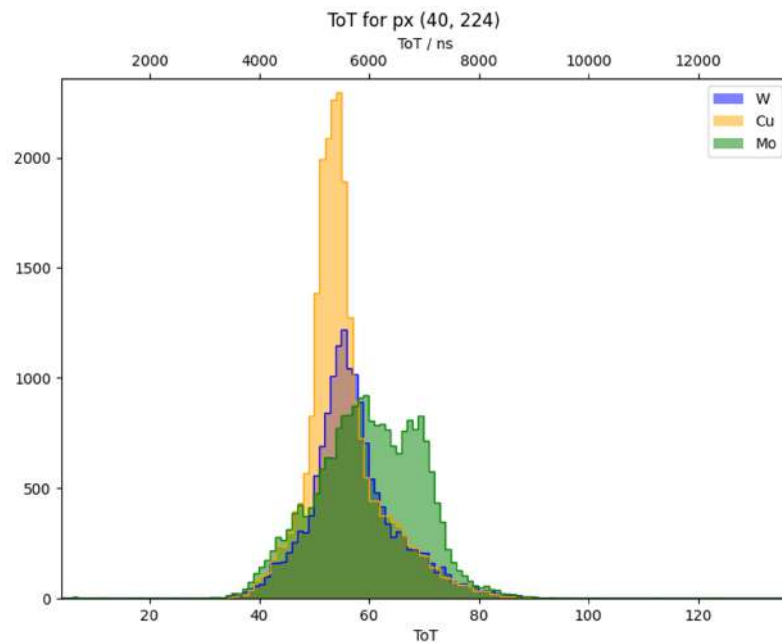
**Fig. 8.2** Expected X-ray spectra from a W, Mo, and Cu anode in 100  $\mu$ m silicon.

### 8.3 Energy dependence of ToT

The suitability of an X-ray tube as a radiation source for prospective ToT stability measurements depends on whether the ToT response of the ATLASPix 3.1 has sufficient energy resolution to distinguish the individual energy peaks of the X-ray spectra shown in fig. 8.2.



(a) Combined ToT spectra of all pixels in beamspot



(b) ToT spectrum of a single pixel

**Fig. 8.3** ToT recorded by ATLASPix 3.1 under irradiation with X-ray photons from different anodes.

To determine the energy dependence of the ToT, a previously largely unirradiated AP 3.1 was irradiated with X-ray photons originating from a molybdenum, copper, and tungsten anode. As a result of pixel-to-pixel variations, the ToT response of the AP 3.1 can only be determined on an individual pixel basis. For a direct comparison, fig. 8.3 shows the ToT recorded by all pixels within the beamspot of the X-ray beam combined (a), as well as the spectrum as recorded by a single arbitrarily chosen pixel (b). It is clearly visible that the energy resolution of the ToT of all pixels combined is inferior to that of a single pixel, which demonstrates that energy calibrations must be conducted for each pixel individually.

While the origin of the first molybdenum peak is not currently clear, it is assumed that the second peak is the 17.1 keV  $K_{\alpha}$  peak.

An energy calibration of the ToT was carried out for six arbitrarily chosen pixels. The peak positions of the Cu  $K_{\alpha}$ , W  $L_{\alpha}$ , and Mo  $K_{\alpha}$  lines were determined by fitting a combined Gaussian and Landau function. The ToT response to an  $^{55}\text{Fe}$  source was used as a fourth calibration point in addition to the three spectra taken using the X-ray tube. The resulting

calibration is shown in fig. 8.4.

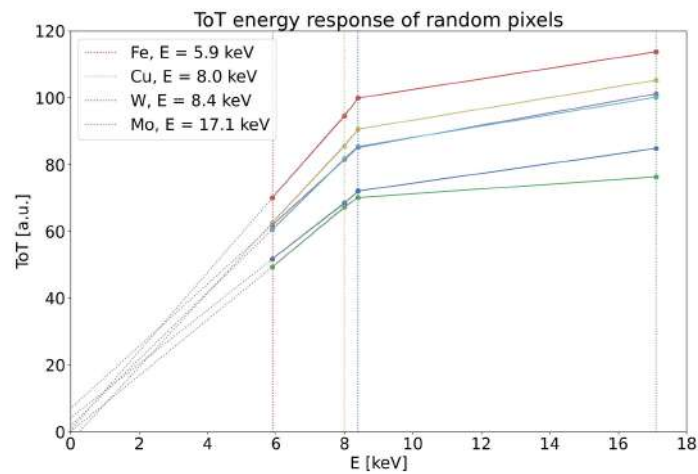


**Fig. 8.4**

In view of the small sample size of six pixels combined with the small number of calibration energies, the result must, of course, be taken with a grain of salt. Nevertheless, two qualitative observations can be made: firstly, the energy response becomes nonlinear towards higher energies. This is in line with previous observations and may be attributed to a saturation of the amplifier circuit [42]. Secondly, the pixel-to-pixel variation of the dynamic range is large, again confirming that pixels need to be calibrated individually.

It can be concluded that the X-ray tube, ideally in conjunction with an  $^{55}\text{Fe}$  source, may serve as a useful tool to monitor changes in the energy dependence of the ToT.

## Chapter 9

# Studies on radiation damage

As described in Ch. 5, there are many ways for radiation to inflict damage on silicon pixel sensors. The two main types of energy loss, NIEL and IEL, cause damage to different parts of the sensor and have different implications for detector operation and radiation hardening. In order to improve the radiation hardness of prospective particle detectors and ensure their successful implementation, it is therefore important that the impact of the expected radiation environment and the contributions of different damage mechanisms are well understood.

Irradiation campaigns where only NIEL damage is expected are common and usually involve neutron irradiation at reactor facilities. These campaigns, however, have two disadvantages: because of the logistics surrounding reactor facilities, sensors are typically sent directly to the irradiation site and returned after the irradiation process is completed. It is therefore not generally feasible to measure the performance of an individual sensor for multiple radiation doses. The entire radiation dose is also deposited in a short amount of time.

An alternative approach to disentangling the damage caused by NIEL and IEL is investigating the effect of proton and photon irradiation. Since photons are expected to cause only IEL while protons cause both IEL and NIEL, comparing the two should provide pointers regarding the origin of any observed radiation effects. The infrastructure surrounding proton- and photon irradiation features several additional assets that make these measurements worth pursuing: The easy accessibility of the tabletop X-ray setup located directly at Heidelberg University (see Ch. 6.2.1) makes it possible to study long-term IEL damage over time. The geometry of the setup also allows for the separate irradiation of the sensor substrate and periphery, enabling investigations of effects on different sensor areas. The cyclotron facility in Bonn has the advantage of allowing for the powering and biasing of the sensor during proton irradiation, which has been difficult to achieve for irradiation campaigns to date.

Control data before and after the irradiation procedures were taken using the dedicated cooling setup in Heidelberg described in Ch. 6.1.4. This was done to both prevent annealing after irradiation, and to reduce the chip noise such that it remains operable.

This section focuses on two separate irradiation campaigns using X-ray photons and protons, with the end goal of gathering sufficient data to disentangle the effects of IEL and NIEL damage. The work carried out within the scope of this thesis serves primarily as a pilot study aimed at the development of a suitable measurement infrastructure and characterisation regimens, and is intended as a precursor to future studies.

## 9.1 Systematic limitations

Given that the work presented in this thesis consists primarily of pathfinder experiments, certain systematic limitations to the methods used only emerged over the course of the investigation. Some of these, like the temperature dependence of the leakage current discussed in section 9.2.4, are corrected for during analyses. Others, like the light sensitivity of the leakage current, are not, and will only be briefly mentioned at this point along with some lessons learned during the development of the experimental methods. The effects mentioned below are generally not systematically studied and should be taken as qualitative caveats.

### 9.1.1 Impact of SMU measure range

The Keithley 2611 source measure unit (SMU) used as a HV power supply features a current range setting allowing for the custom specification of the intended measure range. While it was originally assumed that the smallest possible range still accommodating the measured current would yield the most precise results, it emerged during I-V measurements that range settings below  $100 \mu\text{A}$  reproducibly led to unexplained and unphysical jumps in specific voltage ranges. This issue did not appear at a range setting of  $1 \text{ mA}$ , which was, as a consequence, used in all measurements presented unless otherwise specified.

Fig. 9.1 shows an example of the current jump seen during I-V curves taken of an ATLASPix 3.1 while actively under X-ray irradiation. The measurement is shown for two different X-ray anode current settings.

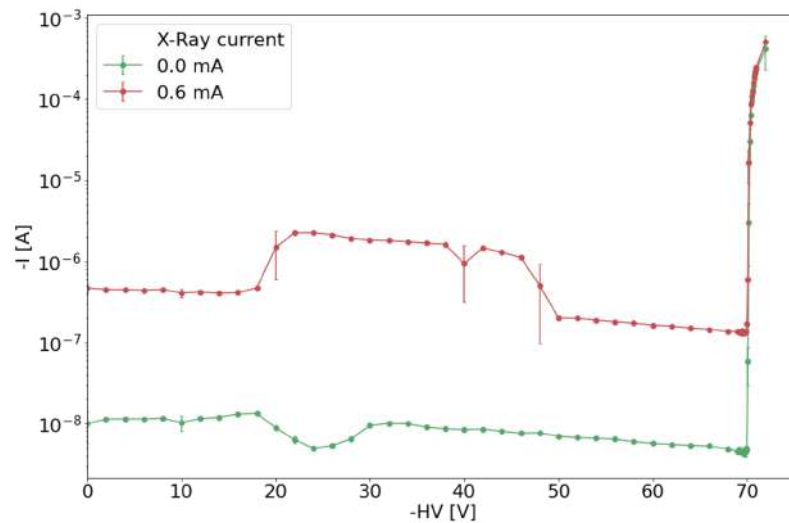


**Fig. 9.1** Unexplained current jumps at a current measure range setting of  $100 \mu\text{A}$  during I-V curves taken at two different X-ray anode current settings.

### 9.1.2 Delay of temperature sensor

Given that the AP 3.1 itself does not feature a temperature sensor, its temperature was estimated using an Adafruit BME 280 sensor installed in the blue cooling box described in Ch. 6.1.4. It is expected that the temperature sensor and the AP 3.1 are not immediately in equilibrium with the ambient temperature when changing the latter, and that a small lag due to the differing materials and powering between the two must be accounted for. To estimate the uncertainty of the recorded temperature, the temperature dependence of the leakage current discussed in Ch. 9.2.4 was exploited by making long-term measurements where the sensors were left to cool to an approximate temperature of  $-20^\circ$  in the freezer, while recording both the temperature and the leakage current. These are compared against similar long-term measurements of the sensors warming back to room temperature. For an

immediate and identical temperature response, the curves are expected to overlap; given that this is not the case – as shown in fig. 9.2 –, the temperature uncertainty is estimated to be  $\pm 3$  °C from the deviation.

It should also be noted that a powered sensor is expected to produce some heat, therefore the temperatures reported throughout this thesis are likely subject to an offset and underestimate the true sensor temperature.

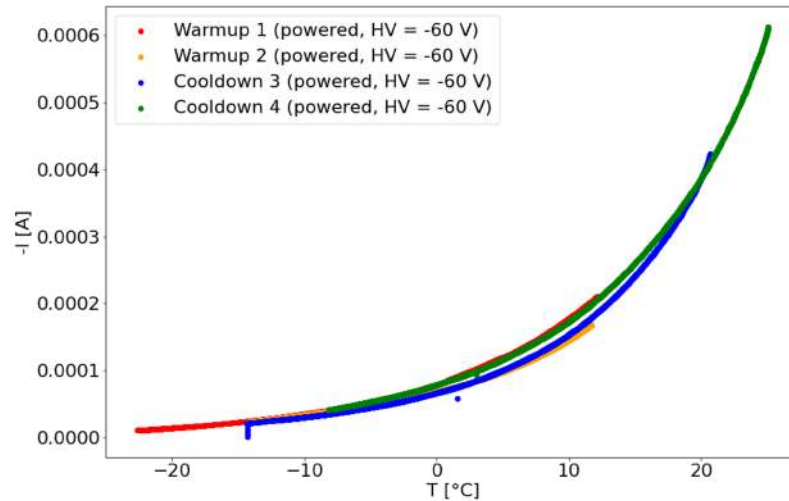


**Fig. 9.2** Leakage current measurements as a function of temperature taken while sensors were warmed up vs. cooled down.

### 9.1.3 Impact of light sensitivity on leakage current

Despite the use of a protective black cap covering the ATLASPix 3.1 sensor, it was observed that the leakage current was increased by up to 500 nA when turning on the light. This is shown for two different temperatures in fig. 9.3. This effect was not taken into account during measurements or analyses.

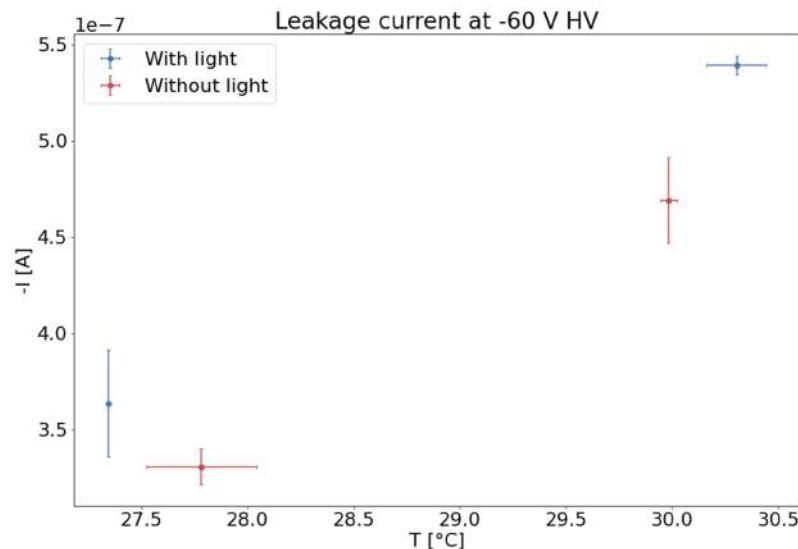


**Fig. 9.3** Leakage current of sensor with and without ambient light for two temperatures.

### 9.1.4 Impact of chip configuration on leakage current

While the sensor was powered using the custom adapters described in 6.1.2 during most measurements presented in this work, it was observed in leakage current measurements

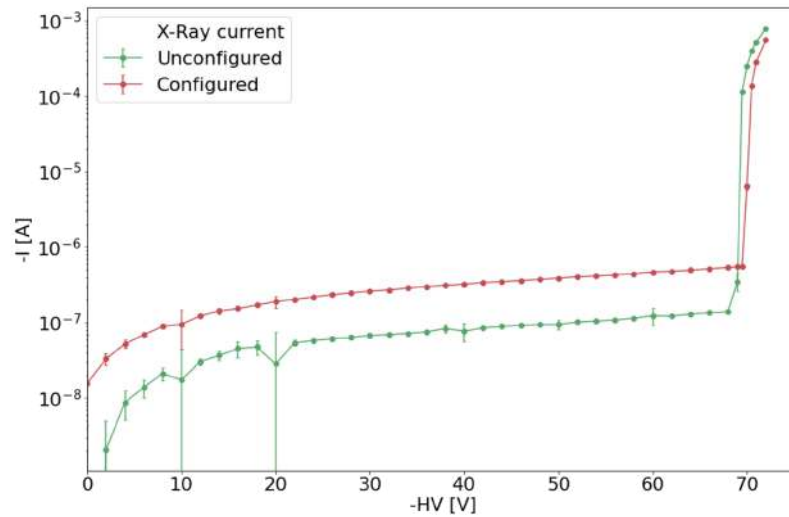


**Fig. 9.4** I-V curves of sensor when configured vs. unconfigured.

using the GECCO system that the leakage current of a configured sensor was up to four times higher than that of an unconfigured sensor. Given that the use of a power adapter makes it difficult to determine the precise state of configuration the sensor is in, this effect may be relevant when comparing different leakage current measurements. The I-V curves of the sensor is shown in fig. 9.4 for an unconfigured and a configured measurement.

## 9.2 Proton irradiation of a powered ATLASPix 3.1

### 9.2.1 Setup

In a first proof-of-principle measurement, a powered and HV-biased ATLASPix 3.1 was irradiated at the Isochronous Cyclotron facility in Bonn in July 2022. A set of characterisation measurements was taken before and after the irradiation. These include the breakdown voltage, leakage current, S-Curves<sup>1</sup>, and the sensor response to <sup>55</sup>Fe irradiation.

#### Cooling

At the irradiation facility, the Device Under Test (DUT) was placed in a dedicated cooling box in line with the proton beam, with its front side facing the beam. The DUT was cooled to an estimated  $-15^{\circ}\text{C}$  using  $\text{N}_2$  gas during the irradiation procedure. The temperature in the cooling box was monitored using two sensors provided by the facility; one was placed close to the pixel sensor at the top of the chip (seen in yellow in fig. 9.5), one at the bottom. Due to the flow of nitrogen within the box, a temperature difference of around  $15^{\circ}\text{C}$  was seen between the sensors. It is assumed that the temperature recorded by the sensor at the top is a more accurate reflection of the true temperature of the chip due to their proximity. Fig. 9.6 shows a snapshot of the temperature monitoring.

<sup>1</sup> See Ch. 9.2.6

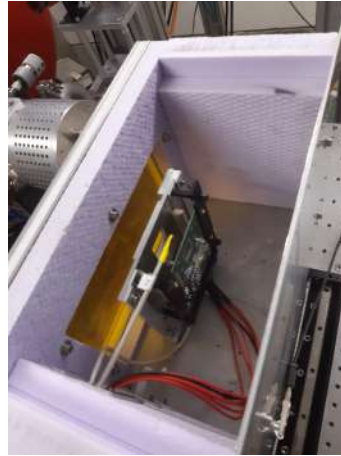


**Fig. 9.5** Insulated DUT box containing an ATLASPix 3.1 at the Isochronous Cyclotron in Bonn.

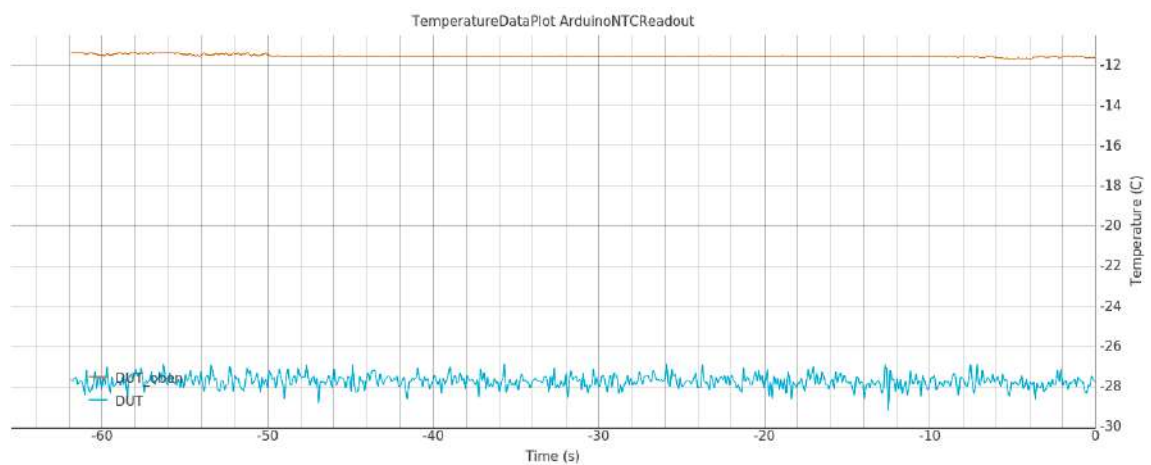


**Fig. 9.6** Snapshot of temperature monitoring during proton irradiation. Temperature data was recorded using two sensors placed at opposite ends of the cooling box; it is assumed that the temperature shown in orange is closer to the true sensor temperature. Image provided by the Isochronous Cyclotron irradiation facility.

### Powering and slow control

The DUT was powered and biased using the custom-made PCIe adapter shown in fig. 6.2 (a), i.e. without use of the GECCO readout system. The adapter was connected to three power supplies located on the gallery adjacent to the beam area via pre-installed BNC cables with a length of 20 m. The low voltages  $V_{dd}$ ,  $V_{ssa}$ ,  $V_{minus}$ , and gate were supplied by two Rohde & Schwarz HMP 4040 power supplies, the HV by a Keithley 2611B SMU.

All voltages applied to the DUT and the associated currents were continuously monitored throughout the irradiation process using the PixMon slow control system introduced in Ch. 6.1.3. The data was collected at a rate of one measurement per second.

### 9.2.2 Irradiation protocol

As the first campaign irradiating a powered sensor with protons, it was necessary to approach the full depletion voltage step-wise given there was no previous knowledge about the amount of radiation the sensor would be able to withstand while under full depletion.

The irradiation procedure was split into two portions:

During the first portion ("fast scan"), the sensor was irradiated with a scanning speed of 60 mm/s and with a constant irradiation current of  $I_{\text{proton}} = 40$  nA. Starting at 0 V, the bias voltage was increased by -10 V between each irradiation step until the full operation bias voltage of -60 V was reached<sup>2</sup>. An I-V curve was taken between each irradiation step. During the fast scan, the sensor was exposed to a total proton fluence of  $\phi_p = 1.9 \times 10^{13}$  protons/cm<sup>2</sup>, or  $\phi_{eq} = 7.8 \times 10^{13}$  neq/cm<sup>2</sup>.

After the fast scan, a second set of irradiations ("slow scan") was carried out where the bias voltage was kept constant at -60 V. Instead of varying the voltage, the irradiation current was reduced with each step, and the scanning speed decreased to 12 mm/s, i.e. lowered by a factor of five lower compared to the fast scan. The slow scan comprises three irradiation steps, with an irradiation current of 40 nA, 30 nA, and 20 nA, respectively. An I-V curve was taken only after the last of the slow scan steps, none between.

The total fluence experienced by the sensor after the full irradiation procedure is  $\phi_p = 2.56 \times 10^{13}$  protons/cm<sup>2</sup>, or  $\phi_{eq} = 1.05 \times 10^{14}$  neq/cm<sup>2</sup>, which is around a fifth of the lifetime fluence of  $\phi_{eq} = 6 \times 10^{14}$  neq/cm<sup>2</sup> expected for the MightyPix.

An overview of the irradiation protocol is shown in table 9.1. The proton fluences are converted to neutron equivalents according to eq. 5.4, and were provided directly by the Isochronous Cyclotron facility.

| $U_{ext}$ during irradiation | $\Phi_{eq}$ [neq/cm <sup>2</sup> ] | $\Phi_p$ [1/cm <sup>2</sup> ] | $I_{\text{proton}}$ [nA] | Scanning speed |
|------------------------------|------------------------------------|-------------------------------|--------------------------|----------------|
| 0 V                          | 5.11e12                            | 1.25e12                       | 40 nA                    | 60 mm/s        |
| 0 V                          | 1.14e13                            | 2.79e12                       | 40 nA                    | 60 mm/s        |
| -10 V                        | 2.32e13                            | 5.66e12                       | 40 nA                    | 60 mm/s        |
| 0 V, LV off                  | 3.16e13                            | 7.7e12                        | 40 nA                    | 60 mm/s        |
| -30 V                        | 4.00e13                            | 9.77e12                       | 40 nA                    | 60 mm/s        |
| -40 V                        | 4.76e13                            | 1.16e13                       | 40 nA                    | 60 mm/s        |
| -50 V                        | 6.11e13                            | 1.49e13                       | 40 nA                    | 60 mm/s        |
| -60 V                        | 7.8e13                             | 1.90e13                       | 40 nA                    | 60 mm/s        |
| -60 V                        | Unknown                            | Unknown                       | 40 nA                    | 20 mm/s        |
| -60 V                        | Unknown                            | Unknown                       | 30 nA                    | 20 mm/s        |
| -60 V                        | 1.05e14                            | 2.56e13                       | 20 nA                    | 20 mm/s        |

**Table 9.1** Irradiation protocol at the Isochronous Cyclotron in Bonn. The fluences during the intermediate steps of the slow scan are not known.

### 9.2.3 Beam-induced current

The current output of the HV supply was continuously monitored throughout the irradiation procedure. The current limit of the HV power supply was set to 10 mA, ensuring that the current did not saturate at any time during the irradiation procedure.

Given the current  $I_p$  of the proton beam and the size  $w$  of the depleted area, it is possible to calculate the theoretically expected beam-induced current  $I_{b-i}$  using

$$I_{b-i} = I_p \cdot N_e, \quad (9.1)$$

where

<sup>2</sup> It should be noted that a mistake caused all power supplies to turn off during the irradiation step with an intended bias voltage of -20 V. This irradiation step is therefore excluded in some analyses below.

$$N_e = \frac{dE}{dx} \Big|_{14 \text{ MeV}} \cdot \frac{\rho_{\text{Si}} w}{E_{eh}}, \quad (9.2)$$

is the number of electrons produced per proton. With an estimated substrate resistivity of  $370 \Omega \text{ cm}$ , the assumed depletion depth  $w$  of an ATLASPix 3.1 supplied with a bias voltage of  $-60 \text{ V}$  is approx.  $50 \mu\text{m}$  following eq. 3.10 [42]. This value is, however, highly uncertain and difficult to determine precisely without dedicated measurements using e.g. C-V curves, which are not obtainable for the AP 3.1 due to a lack of the necessary electrodes on the sensor.

Given the total stopping power of 14 MeV-protons in silicon  $\frac{dE}{dx} \Big|_{14 \text{ MeV}} \approx 26.7 \text{ MeV cm}^2/\text{g}$ , the density of silicon  $\rho_{\text{Si}} \approx 2.31 \text{ g/cm}^3$ , and the average energy necessary for the creation of an electron-hole pair  $E_{eh} \approx 3.65 \text{ eV}$ , this yields an expected current of approx.  $I_{b-i} \approx 3.4 \text{ mA}$  for a beam current of  $I_p = 40 \text{ nA}$ ,  $I_{b-i} \approx 2.5 \text{ mA}$  for  $I_p = 30 \text{ nA}$ , and  $I_{b-i} \approx 1.7 \text{ mA}$  for  $I_p = 20 \text{ nA}$ .

It should be emphasised that this calculation holds true only *given that a proton passes the depleted area in the first place*. This has implications for a sensor whose depletion zone has not reached full lateral extension: as not the entire surface area of the sensor can be assumed to be sensitive to radiation to the same extent, the expected current must be scaled relative to the depleted area of a pixel if it can be assumed that a particle passing through undepleted bulk material does not contribute to the observed current.

Figure 9.7 shows an overview of the observed HV current during the irradiation process (red), along with the voltages used to bias the sensor (blue) and the calculated current  $I_{b-i, th.}$  (dashed horizontal lines). The shading of the background reflects the strength of the beam current  $I_p$ . The full irradiation protocol is listed in Table 9.1 for reference.

Leakage current during proton irradi.

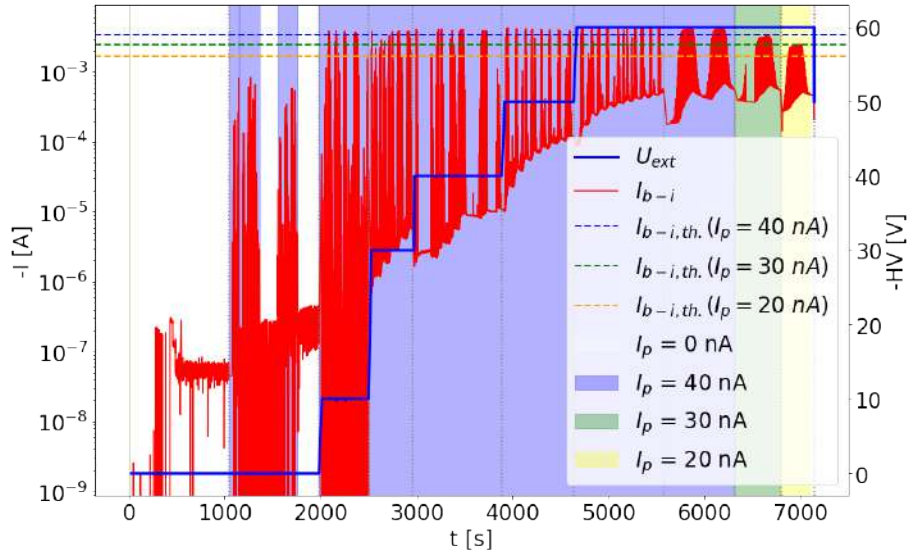


**Fig. 9.7** Beam-induced current (red) and bias voltage (blue) during the irradiation process as a function of time. The vertical gray dotted lines represent the division between the radiation steps. Between each radiation step, an I-V curve was taken and the bias voltage changed.

Fig. 9.7 contains a wealth of information and is worth an in-depth discussion.

Firstly, it is observed that the spill structure of the proton beam is clearly visible in the beam-induced current.

Secondly, the leakage current between the spills increases over time. This is discussed in section 9.2.4.

Thirdly, for a proton beam current of  $I_p = 40$  nA, where the bias voltage  $U_{\text{ext}}$  was varied between 0 V and  $-60$  V, the associated observed beam-induced current is  $I_{\text{b-i}} \approx 0.5$  mA for  $U_{\text{ext}} = 0$  V, and  $I_{\text{b-i}} \approx 4$  mA for  $U_{\text{ext}} \geq 10$  V. For  $I_p = 30$  nA and  $I_p = 20$  nA, the bias voltage was kept at  $U_{\text{ext}} = -60$  V. The observed beam-induced currents are approx.  $I_{\text{b-i}} \approx 3$  mA and  $I_{\text{b-i}} \approx 2$  mA, respectively.

Compared to the theoretically calculated values based on an assumed depletion width of  $w \approx 50$   $\mu\text{m}$  (visualised in fig. 9.7 as dashed lines), the observed leakage current at a bias voltage of  $-60$  V is larger than expected, but scales linearly with the proton beam current as predicted by eq. 9.1. Given that the width of the depletion zone is an estimate associated with large uncertainties, it is not surprising that an offset is found between theory and observation. Reverse-engineering  $w$  under the assumption that the observed beam-induced currents follow equation 9.1 yields a true depletion depth of  $w = 60$   $\mu\text{m}$ , for which the observations would precisely match the expectation.

Theory and experiment diverge, however, when taking into account the increasing bias voltages applied at a proton beam current of  $I_p = 40$  nA. Given that  $w \propto \sqrt{U_{\text{ext}}}$  according to eq. 3.10, it is expected that the depletion width of a sensor with a thickness of  $600$   $\mu\text{m}$  increases continuously for bias voltages between 0 and  $-60$  V. The beam-induced current, which is linearly dependent on  $w$ , should, therefore, exhibit a  $\sqrt{U_{\text{ext}}}$ -dependence. As is shown in fig. 9.7, this is clearly not the case: the beam-induced current is constant for all bias voltages between  $-10$  and  $-60$  V. Considering that the current limit of the HV power supply was set to  $10$  mA throughout the irradiation process, and that the beam-induced current scales with the proton beam current as expected, it is unlikely that the beam-induced current is limited by a current saturation of the power supply. The observation implies that the depletion width is constant at all bias voltages above  $-10$  V. Assuming that the depletion width calculated from the observed currents at  $U_{\text{ext}} = -60$  V is correct, this means that  $w$  is larger than expected for all bias voltages below  $-60$  V.

The alternative scenario consistent with both eq's 3.10 and 9.1 and the observed independence of the beam-induced current from the bias voltage is that there is a mechanism that counteracts the increase of the depletion volume. This mechanism must be independent from the beam-induced current and either limit the depletion width to an absolute value regardless of the bias voltage, implying a saturation effect, or increase in strength proportionally to the bias voltage, thereby keeping the resulting depletion width constant.

Considering the large amount of free charge carriers produced by the proton beam, however, it may also be argued that the assumptions on which the calculation of the depletion voltage depends no longer hold true. A back-of-the-envelope calculation is instructive to estimate the potential effect of the beam-induced increase in charge carriers:

It is shown in [10] that the lifetime of electrons in silicon with a doping concentration on the order of  $10^{13}$   $1/\text{cm}^2$ , as is the case for a boron-doped silicon semiconductor with a resistivity  $370$   $\Omega\text{cm}$ , is on the order of  $1$  ms. The approximate number of electrons generated by the proton beam per second is given by eq. 9.1 and 9.2; taking into account the  $1$  ms lifetime of electrons, the full width of the silicon sensor  $w \approx 600$   $\mu\text{m}$ , and normalising to a proton beam diameter of  $< 1$  cm, yields on the order of  $10^{15}$  electrons contributing to the space charge within the silicon bulk at any given moment. Given that this is two orders of magnitude larger than the doping concentration, the beam-induced space charge has the potential to significantly modify the width of the depletion region. While the exact implications of this large change to the space charge and to what extent it contributes to the observed deviation of the observed from the expected beam-induced current is not clear, it is an effect that must be taken into account and is worth investigating further.

### 9.2.4 Leakage current

#### Leakage current between spills

The beam-induced current in Figure 9.7 exhibits a discrete spill structure, which reflects the scanning pattern of the beam. The valleys between each spill therefore represent the leakage current of the sensor.

The leakage current can be isolated from the beam-induced current by determining the lower envelope of the overall current recorded during the irradiation process. This is demonstrated in fig. 9.8, where the upper envelope containing the beam-induced current is shown in green, and the lower envelope representing the leakage current in red.

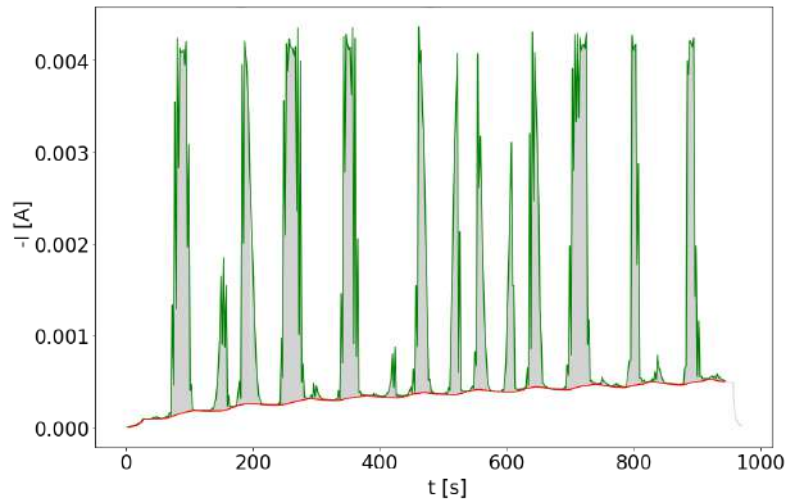


**Fig. 9.8** Spill structure of the proton beam at the Isochronous Cyclotron. The lower envelope is shown in red, the upper envelope in green.

The resulting leakage currents during the slow scan irradiation are shown in fig. 9.9 as a function of time, where the x-axis reflects the de facto time that passed since the beginning of the first measurement in order to capture the downtime between measurements. Two effects are of note: firstly, the leakage current between spills increases with the total radiation fluence. Secondly, it decreases again after the end of each spill, albeit at a lower rate than it increases. These two effects combined lead to the saw tooth structure of the leakage current and its overall increase over time, which is indicative of a charge-up effect. Exploring the timescale of the discharging would be of interest for future measurements.

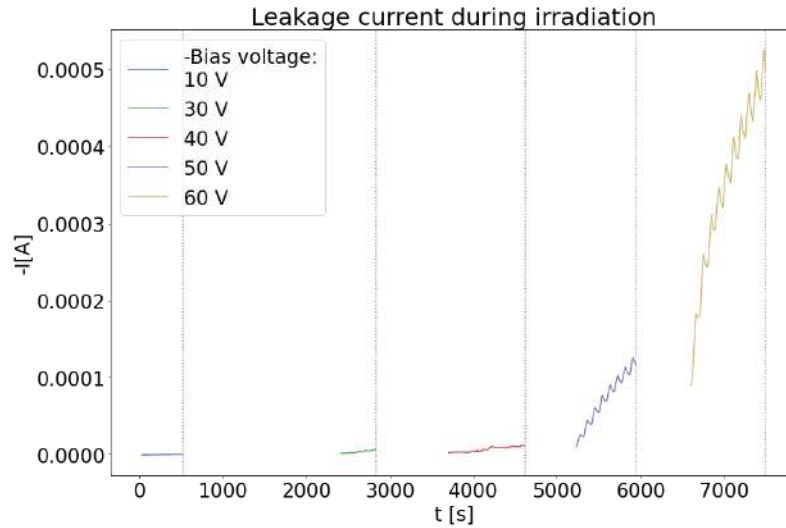


**Fig. 9.9** Time evolution of the leakage current between spills.

### Fluence dependence

In order to measure the breakdown voltage and leakage currents, an I-V curve of the irradiated sensor was taken between each irradiation step while the proton beam was off. Comparing the currents at specific voltages allows us to follow the evolution of the leakage current for increasing fluences.

Following eq. 5.11, it is expected that the NIEL-induced leakage current scales linearly with the radiation fluence  $\phi_{eq}$  and with the width  $w$  of the depletion region, which is inversely proportional to square of the effective doping concentration  $N_{eff}$  as per eq. 3.8. If eq. 5.11 holds true, any deviation from linearity in fluence-dependence would therefore be attributed to changes in  $N_{eff}$ .

Fig. 9.10 shows the I-V characteristics taken between individual irradiation steps. The leakage current  $I_{leak}$  recorded at -60 V bias voltage is shown as a function of the total proton fluence in fig. 9.11. It can be seen that  $I_{leak}$  increases nearly linearly with the fluence until  $\phi_{eq} = 4.76 \cdot 10^{13} \text{ neq/cm}^2$ , then rises steeply, and flattens again.

This observation implies a sudden decrease in the effective doping concentration  $N_{eff}$  between  $\phi_{eq} \approx 5 \cdot 10^{13} \text{ neq/cm}^2$  and  $\phi_{eq} \approx 8 \cdot 10^{13} \text{ neq/cm}^2$ .

While the amount of data available at this point is not sufficient to claim a definitive explanation for this phenomenon, it is qualitatively consistent with the radiation-induced acceptor removal observed in [31]: as was shown in fig. 5.4, an epitaxial silicon wafer with a resistivity between 250 and 1000  $\Omega \text{ cm}$  irradiated with 23 GeV protons experiences a radiation-induced decrease in  $N_{eff}$ , which reaches its minimum value at a fluence between  $5 \cdot 10^{13}$  and  $1.5 \cdot 10^{14} \text{ neq/cm}^2$ . Given a nominal resistivity of 200 - 400  $\Omega \text{ cm}$  and bearing in mind that some differences between the irradiation of epitaxial silicon with 23 GeV protons and that of a HV-MAPS sensor with 14 MeV protons are expected, this is in line with the sharp increase in  $I_{leak}$  seen in fig. 9.11 from  $\phi_{eq} \approx 5 \cdot 10^{13} \text{ neq/cm}^2$  onward.

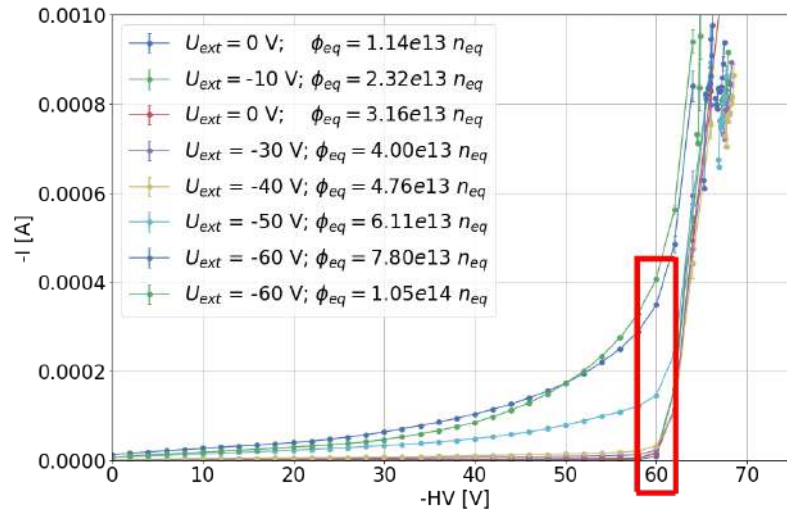


**Fig. 9.10** I-V curves recorded between irradiation steps. The current at -60 V (red box) is used to study the fluence dependence of the leakage current.

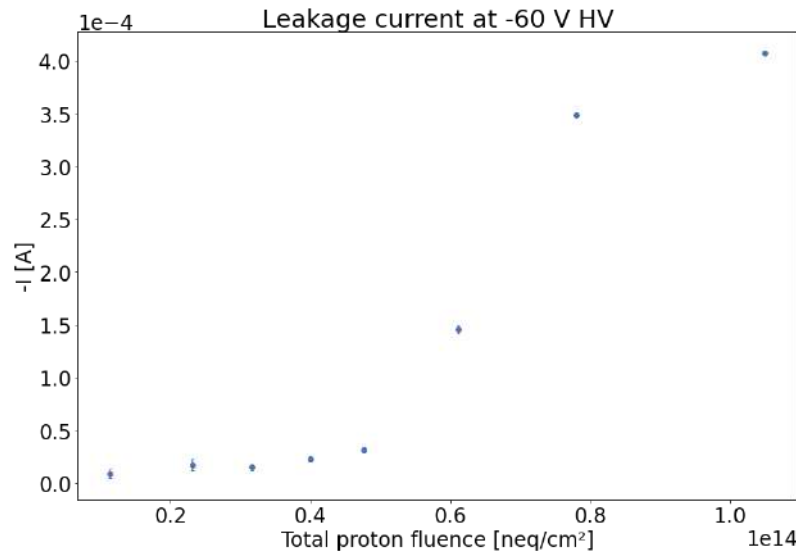


**Fig. 9.11** Leakage current at a bias voltage -60 V, which is recorded during I-V curves between spills, as a function of the total proton fluence.

### Temperature dependence

Aside from the damage-induced dependence on the irradiation fluence, the leakage current is also inherently expected to scale with the square of the temperature due to the temperature dependence of the intrinsic carrier density discussed in Ch. 3.1.2. This dependence is quantified in eq. 3.19. In order to determine whether eq. 3.19 accurately describes the temperature scaling of the AP 3.1 before and after irradiation, and whether irradiation changes the sensor response to temperature variation, the leakage current was measured as a function of temperature.

Using the cooling setup described in Ch. 6.1.4 and the custom power adapter described in section 6.1.2, the proton-irradiated sensor was powered, biased to  $-60$  V, and cooled from room temperature to approximately  $-15$  °C overnight. As the infrastructure for measurements involving cooled sensors was built only after the proton irradiation campaign had been completed, a comparable control measurement of the chip before irradiation unfortunately does not exist. Instead, a second sensor that had not previously been exposed to proton irradiation is used as reference. It should be noted that around 5% of

the sensor area was exposed to a total dose of  $\sim 900$  Gy of X-ray radiation 5 months prior to the measurement<sup>3</sup>.

The data below were taken three months after the completion of the proton irradiation, during which time the proton-irradiated sensor was largely kept at sub-zero temperatures to prevent annealing. It should be noted that the temperature recorded by the dedicated temperature sensor is expected to both lag behind the true temperature by a maximum of 3 °C, and likely also be somewhat lower than the temperature of the irradiated sensor since the chip was powered. This is briefly discussed in section 9.1.2.

Figures 9.12 and 9.13 below show the temperature dependence of the proton-irradiated and the unirradiated chip, respectively. It is immediately clear that the irradiation process caused a sizable increase in leakage current; this effect is of around 3 orders of magnitude. Eq. 3.19 is fitted to the measured data in order to obtain a value for  $E_{\text{eff}}$ , for which the empirical best-fit values are  $E_{\text{eff}} = 1.19 - 1.21$  eV [26].

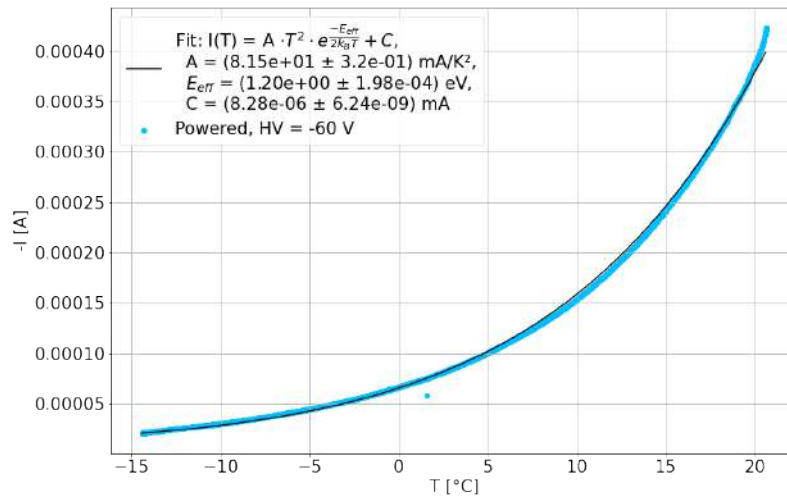


**Fig. 9.12** Leakage current of the proton-irradiated sensor as function of temperature. Data taken around three months after irradiation with a total fluence of  $\phi_{\text{eq}} = 1.05 \times 10^{14}$   $n_{\text{eq}}/\text{cm}^2$ .

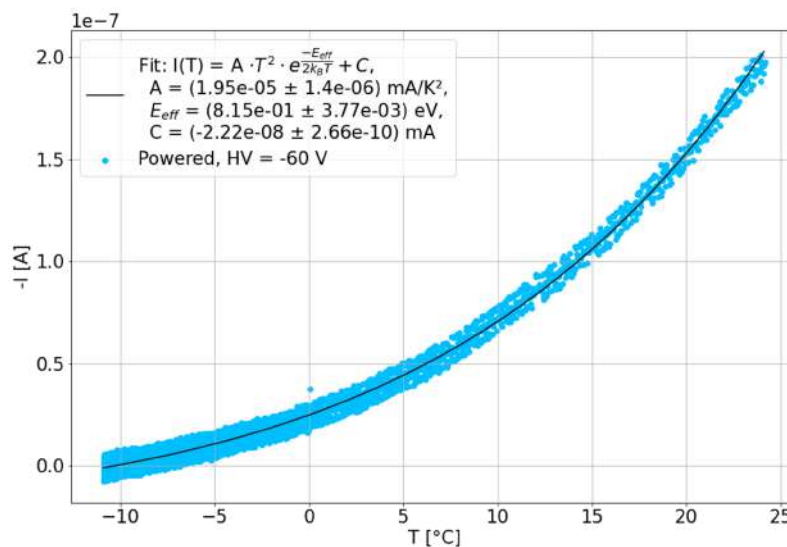


**Fig. 9.13** Leakage current of an unirradiated sensor as a function of temperature.

<sup>3</sup> The X-ray campaign was performed using a 5 mm collimator, therefore only a small part of the sensor is expected to have been impacted by the radiation. The measurement in question is described in detail in Ch. 9.3.2

The fit value found for the proton-irradiated sensor is  $E_{\text{eff}} = (1.20 \pm 2 \cdot 10^{-4})$  eV, which is consistent with the empirical best-fit value. The best fit for the unirradiated sensor, however, is  $E_{\text{eff}} = (0.83 \pm 40 \cdot 10^{-4})$  eV and therefore lower than expected.

While the reason for this deviation is not currently understood, it is worth pointing out that the leakage current of the unirradiated sensor is several orders of magnitude below that of the irradiated sensor and close to the detection limit of the power supply. It is not clear what impact this may have on the measurement accuracy, and it can be assumed that the measurement of the irradiated sensor is more reliable.

The observed temperature dependence of the irradiated sensor indicates that the leakage current after proton irradiation is dominated by thermal electron-hole generation in the silicon bulk, as that is the underlying mechanism from which eq. 3.19 derives.

### 9.2.5 Breakdown voltage

The I-V characteristic of a HV-MAPS sensor is expected to broadly follow the characteristic of a diode.

In order to monitor the breakdown voltage over the course of the irradiation process, an I-V curve of the chip was taken between each irradiation step. This was done in 2-V steps between 0 and -72 V, with ten measurements taken at each voltage point. The first and last point are trimmed in order to remove jumps in the data originating from voltage switching, leaving a total of eight data points per voltage. Their standard deviation is used as the statistical uncertainty. The reference data of the unirradiated chip, as well as the I-V curves taken of the irradiated sensor after the irradiation process, were taken using a smaller step size of 0.5 V in the continuous regions and 0.1 V in the breakdown regime. Five measurements were taken in 1-second intervals at each voltage step. The sensors were powered during the measurements, but not configured. All I-V curves taken outside the irradiation facility were taken using the cooling setup described in section 6.1.4, and with the PCIe adapter described in section 6.1.2.

#### Determination of the breakdown voltage

The breakdown voltages were found using the **k factor** initially introduced in [28], which is given by

$$k(I, U) = \frac{\Delta I}{\Delta U} \cdot \frac{U}{I}. \quad (9.3)$$

Following this approach, the breakdown voltage  $U_{BD}$  is given by the maximum voltage for which  $k$  is lower than a limit value  $k_{BD}$ . A limit of  $k_{BD} = 4$  was empirically found to yield good results for smooth breakdowns in [28], and is therefore used in this work as well. This method is favourable to a linear extrapolation since it is more consistent for breakdowns featuring smooth continuous increases rather than the abrupt breakdown expected from avalanche breakdowns. A value of  $k = 1$  corresponds to ohmic behaviour, while  $k \gg 1$  is found for avalanche breakdowns. Fig. 9.14 shows an example of the evolution of the k factor in a generic I-V curve. The dotted gray line represents the cutoff value of  $k_{BD} = 4$ .

Due to the difference between the voltage step sizes in the I-V curves taken of the irradiated and the unirradiated sensors, the errors in  $U_{BD}$  are estimated to be  $\pm 2$  V for a step size of 2 V, and  $\pm 1$  V for the finer-grained measurements.

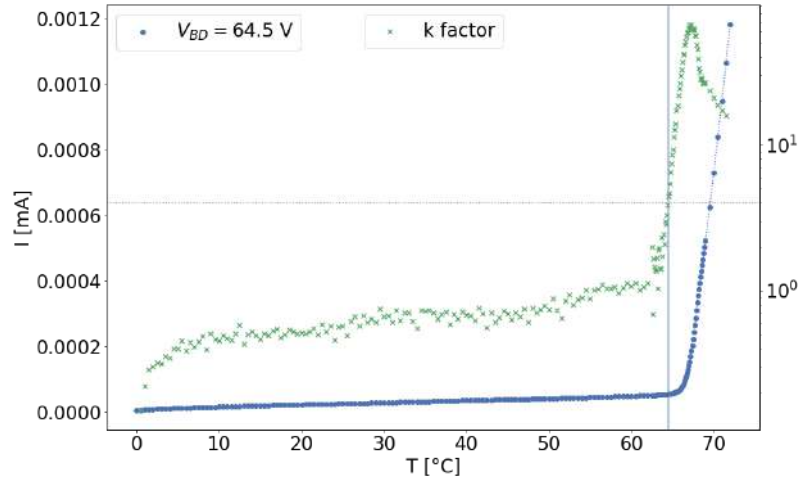


**Fig. 9.14** Determination of the breakdown voltage using the k factor. The horizontal dotted gray line represents the cutoff value of  $k_{BD} = 4$ , the vertical blue line the associated breakdown voltage  $V_{BD}$ .

### Fluence dependence

The breakdown voltages of the I-V curves taken between the individual proton irradiation steps are shown as a function of the neutron-equivalent proton fluence in fig. 9.15. The breakdown voltage found at room temperature before and after the irradiation are included in red and green, respectively; the remaining data points (blue) were taken at approx.  $-15$  °C. The associated I-V curves can be found in fig. 9.10. All measurements shown in fig. 9.15 were taken using the remote setup described in section 9.2.1. The sensor was not moved between measurements.

While the temperature difference between the measurements taken before and during the irradiation process is expected to have some impact on the breakdown voltage, this effect is shown to be on the order of  $\mathcal{O}(1)$  V in section 9.2.5. The steep drop by  $\sim 10$  V observed after the first irradiation step, during which the sensor was irradiated with a fluence of  $\phi_{eq} \approx 5 \cdot 10^{12}$   $n_{eq}/cm^2$  at a bias voltage of  $U_{ext} = 0$  V, significantly exceeds this value.  $U_{BD}$  is then seen to decrease by a further 2 V, before stabilising at  $\sim 56$  V until the end of the fast scan. The data point at around  $6 \cdot 10^{13}$   $n_{eq}/cm^2$  is assumed to be an outlier. The measurement at  $\phi_{eq} \approx 1 \cdot 10^{14}$   $n_{eq}/cm^2$  was taken after the full slow scan at lower beam intensities was completed, which brought the breakdown voltage out of the plateau and decreased it by another 4 V.

One final measurement was taken after the chip had been left to warm to room temperature overnight. During this time, the sensor seems to have partially recovered, and a breakdown voltage of  $\sim 62$  V is observed.

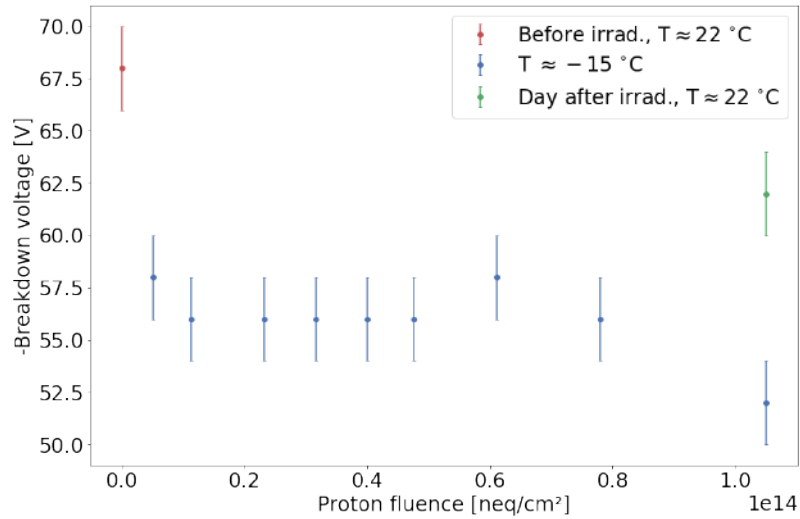


**Fig. 9.15** Evolution of the breakdown voltage taken between irradiation steps as function of total proton fluence.

Like the observations of the beam-induced current, finding a sound interpretation of the fluence-dependence of the breakdown voltage is not straightforward.

Previous proton irradiation campaigns have yielded conflicting results regarding the breakdown behaviour of silicon semiconductor detectors, where certain sensors exhibit an increased breakdown voltage after proton irradiation, and some a decrease (see eg. [32], [33]). It was shown in [33], where the breakdown behaviour of several different ATLASPix1 and ATLASPix2 — predecessors of the ATLASPix 3.1 — prototypes were investigated, that the geometry of the pixel design has a strong impact on the fluence dependence of the breakdown voltage. It is, however, not clear whether a direct comparison between these measurements and those carried out within the scope of this thesis can be made given that these measurements were carried out at higher fluences of  $\phi_{\text{eq}} > 5 \times 10^{14} \text{ neq/cm}^2$ , and were made using unpowered, older prototypes. More recent neutron irradiation campaigns featuring unpowered ATLASPix 3.1 sensors at  $\phi_{\text{eq}} > 3 \times 10^{14} \text{ neq/cm}^2$  have yielded an increase in breakdown voltage [34], which is phenomenologically consistent with observations made in [33].

With the limited amount of data available and lack of knowledge about the precise origin of the observed breakdown (see discussion in Ch. 4.3), we are left to speculate about the cause for the shift in breakdown voltage.

One difference between the proton irradiation at the Isochronous Cyclotron and the neutron irradiation campaigns to date is the powering and biasing. While it is not clear to what extent the powering of the sensor plays a role in the way radiation damage manifests, it should be pointed out that the largest drop in breakdown voltage occurred even before a bias voltage was applied. Meanwhile, any increase in bias voltage afterwards does not seem to have had an effect, as the breakdown voltage plateaued until the maximum bias voltage of  $U_{\text{ext}} = -60 \text{ V}$ . Barring an impact of the low voltages and any effects that may occur only at higher fluences, this leaves the inherently different nature of the energy loss of protons, which cause TID damage in silicon, and neutrons, which do not.

The second drop in breakdown voltage at  $\phi_{\text{eq}} \approx 1 \cdot 10^{14} \text{ neq/cm}^2$  is another observation that has no immediate clear explanation. While it is possible that this effect is related to the higher fluence, the lack of any obvious fluence dependence of the breakdown voltage between  $\phi_{\text{eq}} \approx 1 \cdot 10^{13} \text{ neq/cm}^2$  and  $\phi_{\text{eq}} \approx 8 \cdot 10^{13} \text{ neq/cm}^2$  at least does not suggest that a continuous damage process is responsible. Given that a lower beam intensity is unlikely to cause an increase in damage rate, the alternative explanation is the change in scanning speed from  $\phi_{\text{eq}} \approx 8 \cdot 10^{13} \text{ neq/cm}^2$  onward. It is possible that charge-up effects induced by the beam cause a temporary change in breakdown voltage that reaches

an equilibrium for specific spill frequencies, and that the more continuous spill structure of the slow scans causes a stronger shift in the breakdown voltage. Whether the partial recovery of the breakdown voltage within 24 hours can be attributed to annealing effects or may be related to a discharging of such potential charge-up effects is difficult to tell without additional data.

I-V curves taken three months after the irradiation campaign (see section on temperature dependence below) showed a continued recovery of the breakdown voltage to  $U_{BD} = -65.5$  V at room temperature. While the sensor was stored at sub-zero temperatures after proton irradiation, it was frequently removed for measurements and warmed up to room temperature for short periods of time, such that annealing effects cannot be ruled out in this case, either.

Even in the absence of a definitive explanation for the observed radiation-induced shift and subsequent recovery of the breakdown voltage, it can be concluded that the irradiation procedure caused an overall decrease in breakdown voltage, and that more measurements are needed in order to find a time constant of the recovery.

### Temperature dependence

The breakdown voltage of the proton-irradiated sensor was measured at different temperatures three months after the irradiation campaign, and compared to the corresponding breakdown voltages of an unirradiated sensor. An overview of the I-V curves of the irradiated sensor is shown in fig. 9.16, the breakdown voltages of both sensors in fig. 9.17.

It is evident from fig. 9.17 that the breakdown voltage of both the irradiated and the unirradiated sensor exhibits a dependence on the temperature. A linear fit is applied for both; it is found that the fitted slopes are compatible within their standard deviations and the temperature dependence of the breakdown voltage does not change significantly after proton irradiation up to  $\phi_{eq} \approx 1 \cdot 10^{14}$  n<sub>eq</sub>/cm<sup>2</sup>.

As the precise mechanism of the early AP 3.1 breakdown is not known, it is difficult to find a definitive explanation for its observed temperature dependence. Under the assumption that the breakdown is an avalanche effect, however, it may be speculated that the temperature dependence is related to a change in electron mobility: for an avalanche effect to occur, the charge carriers must have sufficient kinetic energy to continue ionising surrounding atoms. In a semiconductor with an electric field  $E$ , the velocity of a charge carrier is given by

$$v = \mu E, \quad (9.4)$$

where  $\mu$  is the charge carrier mobility. It is shown in [38] that for a substrate resistivity of  $\rho > 0.04$  Ωcm and for temperatures between 250 and 500 K, the probability of electron-electron scattering increases. This leads to a decrease in electron mobility, and, given that the strength of the electric field is not expected to be temperature-dependent, consequently to a decrease in charge carrier velocity.

Since the observation is phenomenologically consistent with what would be expected of an avalanche effect, it may serve as an indicator regarding the nature of the ATLASPix breakdown.

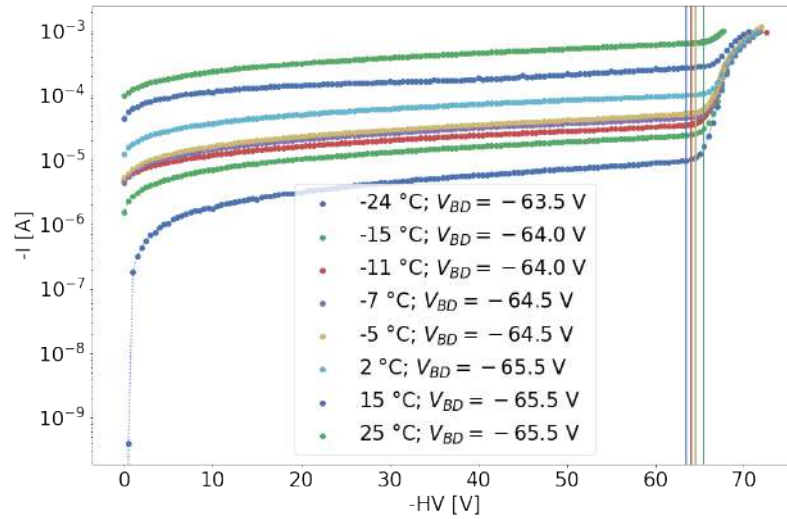


**Fig. 9.16** I-V curves of proton-irradiated sensor at different ambient temperatures. Data taken three months after irradiation with a total fluence of  $\phi_{eq} = 1.05 \times 10^{14}$  n<sub>eq</sub>/cm<sup>2</sup>.

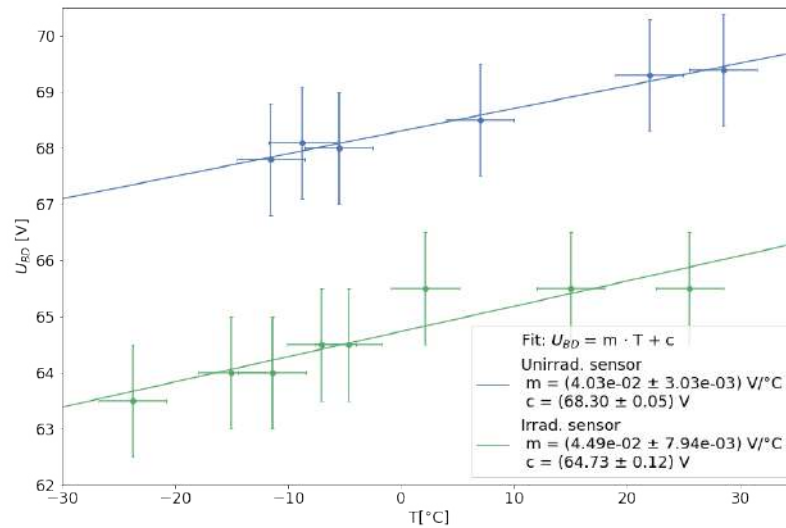


**Fig. 9.17** Breakdown voltage of a proton-irradiated and an unirradiated sensor as a function of temperature.

### 9.2.6 S-Curves

The individual in-pixel thresholds above which a signal is registered can be determined using **S-Curves**. These are obtained by injecting a set number  $N_{inj}$  of pulses at voltages of increasing strength into the amplifier circuit of each pixel, and plotting the number  $N$  of hits recorded against the injected voltage  $V_{inj}$ . The resulting curve is expected to follow the shape of a smeared-out step function, which, using the Gaussian error function erf, can be described using

$$N(V_{inj}) = \frac{N_{inj}}{2} \left( 1 + \operatorname{erf} \left( \frac{V_{inj} - \mu}{\sqrt{2}\sigma} \right) \right). \quad (9.5)$$

The threshold is then given by  $\mu$ , which is the value at which 50% of the injected pulses are registered as hits, while  $\sigma$  describes the Gaussian noise. An example of an S-Curve fit is shown in fig. 9.18.

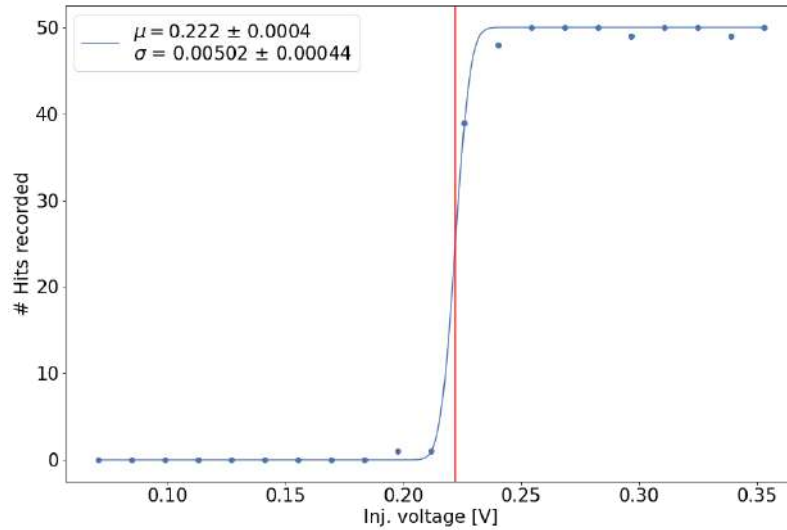


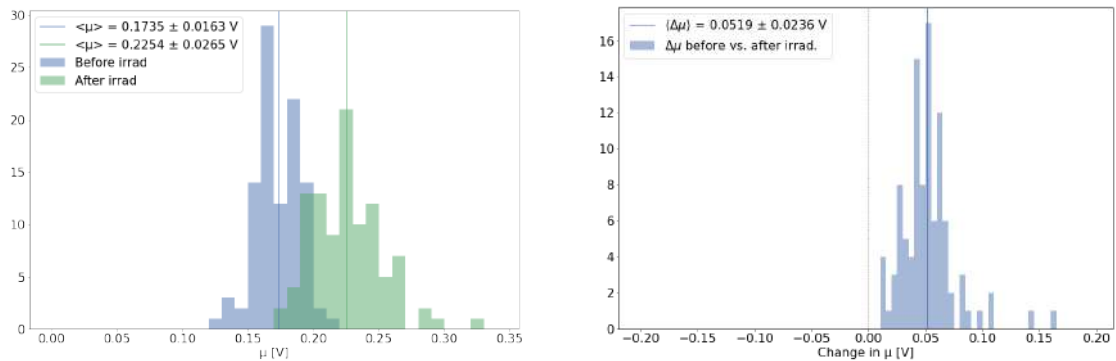
**Fig. 9.18** Example of an S-Curve.

In an effort to monitor for any potential shifts in the in-pixel thresholds post-proton irradiation, 100 pixels were selected at random and their S-Curves measured before and after the proton irradiation campaign.

The reproducibility of the S-Curve measurements was confirmed by repeating the procedure under the same conditions, i.e. by measuring the irradiated sensor at  $-15\text{ }^{\circ}\text{C}$  in the freezer. Comparing the resulting values on a pixel-to-pixel basis, it was found that the threshold and noise deviated by an average of  $\langle\Delta\mu\rangle = (-0.0035 \pm 0.0160)\text{ V}$  and  $\langle\Delta\sigma\rangle = (-0.0010 \pm 0.0040)\text{ V}$ , which is not statistically significant.

Similarly, measurements at two different temperature points of  $-5\text{ }^{\circ}\text{C}$  and  $-15\text{ }^{\circ}\text{C}$  showed no significant temperature dependence, where the thresholds recorded for each pixel differed by an average of  $\langle\Delta\mu\rangle = (-0.0024 \pm 0.0163)\text{ V}$ , and the Gaussian noise by  $\langle\Delta\sigma\rangle = (-0.0001 \pm 0.0044)\text{ V}$ .

Comparing the values found for the irradiated sensor to those of the unirradiated sensor, however, reveals a significant shift in the threshold. This is visualised in fig. 9.19, which shows the measured threshold distribution. It is found that the threshold increased by  $\langle\Delta\mu\rangle = (0.0519 \pm 0.0236)\text{ V}$  after proton irradiation. A similar comparison of the Gaussian noise shows no significant difference, where  $\langle\Delta\sigma\rangle = (0.0030 \pm 0.0038)\text{ V}$ .



**(a)** Threshold distribution before and after irradiation. The average thresholds are indicated with the vertical blue and green line, respectively.

**(b)** Distribution of pixel-to-pixel threshold deviation. The baseline of 0 is indicated in gray.

**Fig. 9.19** Comparison of in-pixel threshold before and after proton irradiation.

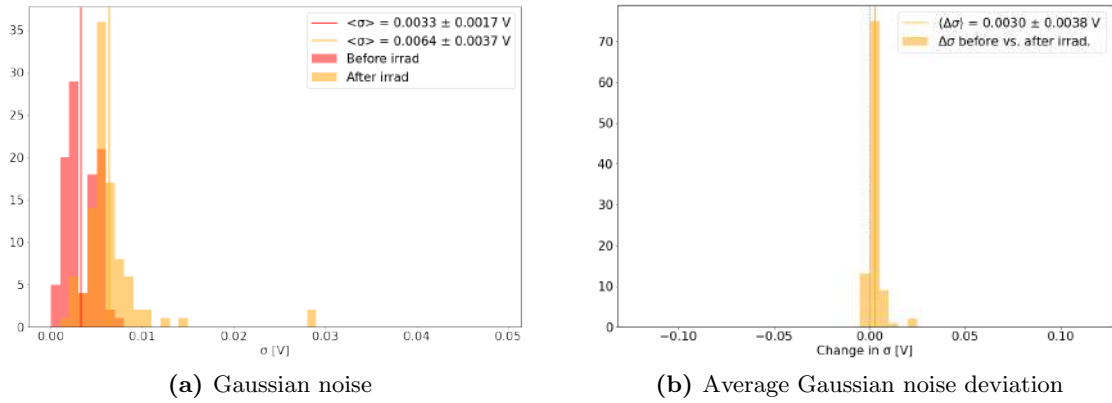


**Fig. 9.20** Comparison of Gaussian noise distribution before and after proton irradiation.

### 9.2.7 VDAC response

As described in Ch. 4, the amplified pulses in an ATLASPix are capacitively coupled to globally tunable voltages *baseline* and *threshold*. A shift in these voltages would therefore be indicative of damage sustained by the digital circuitry of the sensor and could lead to e.g. undesired signal loss or noise.

To assess whether the proton irradiation campaign at the Isochronous Cyclotron caused any obvious damage to the digital circuitry, the VDACs *Bl* and *Th*, as well as the VDAC *Inj* used to tune the injection test pulses, were measured using an oscilloscope. As no pre-irradiation control measurements exist for the irradiated sensor, the values found are compared to those of another, unirradiated chip.

The voltages in question were measured against ground and without applying an external bias voltage. Each data point is the statistical average of 500 samples; the errors are given by their standard deviation.

Fig's 9.21, 9.22, and 9.23 show the voltage response of the baseline, threshold, and injection voltages, respectively, to digital tuning. The direct comparison between the measured voltages of the unirradiated and the irradiated sensor shows a linear dependency for both, where all fit values are compatible within the standard deviations.

Given the good agreement between the measurements pre- and post-irradiation, it may be concluded that while damage to the digital circuitry cannot be ruled out, it can be assumed that its basic functionality remains intact and that the shifts observed in the in-pixel threshold (see section 9.2.6) are not caused by a global shift in threshold, baseline, or injection strength.

### 9.2.8 Noise

As described in Ch. 3.2.3, the temperature and leakage current of a sensor are expected to have an impact on its noise level due to fluctuations in amplifier output, baseline, and threshold shifts. Given that the damage sustained by irradiation also has the capacity to affect these sensor components, comparing the noise rate-dependence of an irradiated sensor to that of an unirradiated sample may provide pointers regarding the origin of the noise.

Using the cooling setup described in Ch. 6.1.4 in conjunction with the GECCO readout system, 60-second noise maps were taken of the irradiated sensor at  $0\text{ }^{\circ}\text{C}$  and  $-6\text{ }^{\circ}\text{C}$  and at bias voltages between 0 and  $-60\text{ V}$ . A reference measurement of the unirradiated chip was made at  $0\text{ }^{\circ}\text{C}$ . The data presented below was taken 4 months after completion of the proton irradiation campaign.

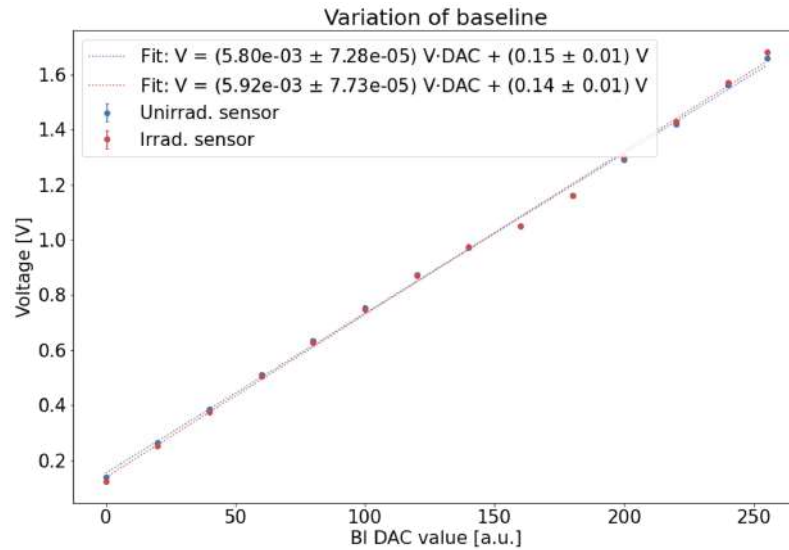


**Fig. 9.21** Sensor response to changes in the baseline DAC value  $Bl$ . Voltages measured using an oscilloscope.

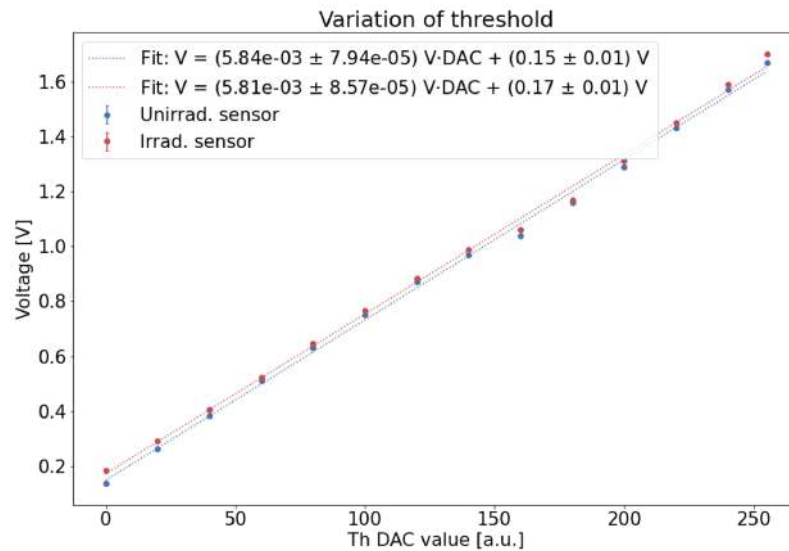


**Fig. 9.22** Sensor response to changes in the threshold DAC value  $Th$ . Voltages measured using an oscilloscope.

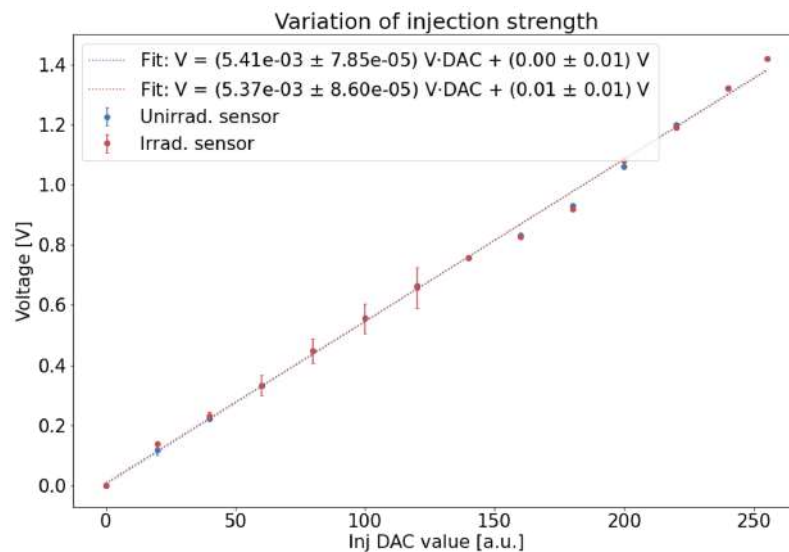


**Fig. 9.23** Sensor response to changes in the injection strength  $Inj$ . Voltages measured using an oscilloscope.

As a qualitative example, fig. 9.24 shows 60-second noise hit maps taken at  $T \approx 0^\circ\text{C}$  and  $U_{\text{ext}} = -40\text{ V}$  of the unirradiated and the irradiated sensor, respectively.

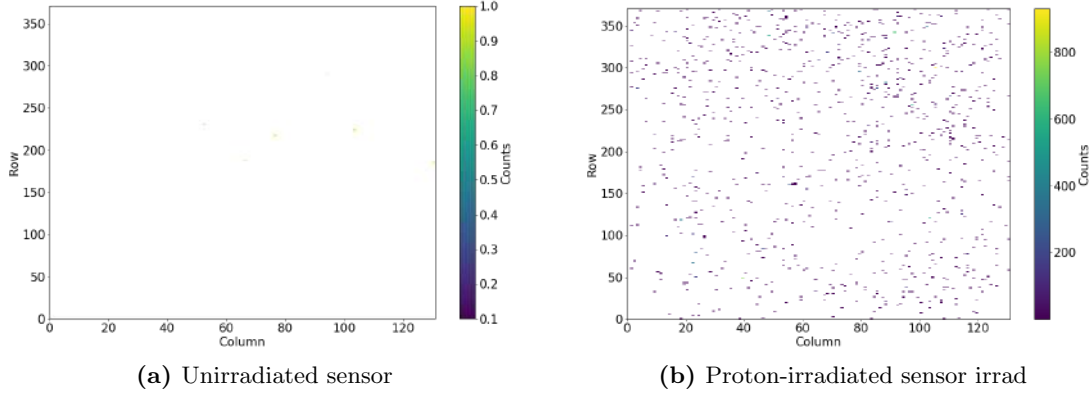


**Fig. 9.24** 60 second-noise maps taken at  $T \approx 0^\circ\text{C}$ ,  $HV = -40\text{ V}$

The increase in noise after proton irradiation is apparent. An overview of all measurements at both temperatures and including the reference measurement of the unirradiated sensor is provided in fig. 9.25 as a function of the applied bias voltage  $U_{\text{ext}}$ .

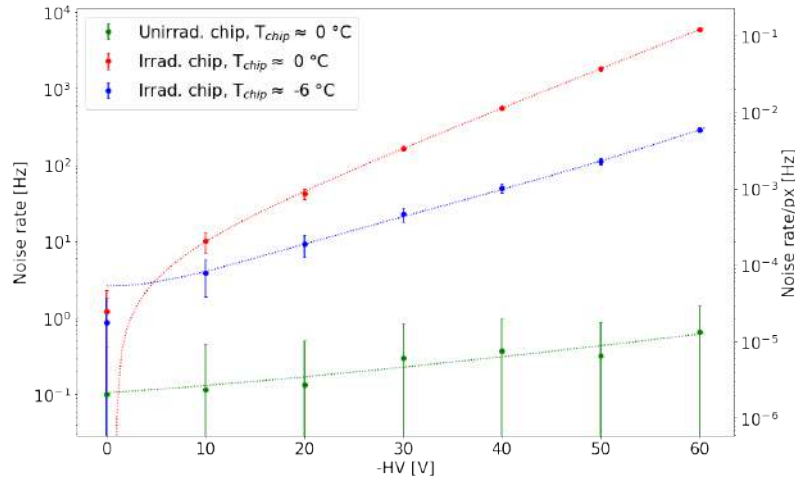


**Fig. 9.25** Noise rate of the proton-irradiated and an unirradiated sensor as a function of the applied bias voltage.

As expected, the noise rate of the irradiated sensor is consistently higher than that of the unirradiated chip, and lower at  $-6^\circ\text{C}$  than at  $0^\circ\text{C}$ .

An empirical fit was found that describes the observed data well. The fit function used was

$$r = m \cdot g^{(-t \cdot U_{\text{ext}})^n} + b, \quad (9.6)$$

where  $r$  is the noise rate in Hz. The fit parameters found are listed in table 9.2.

|                             | m     | t    | b      | g    | n    |
|-----------------------------|-------|------|--------|------|------|
| Irrad., $-6^\circ\text{C}$  | 18.19 | 0.08 | -15.58 | 0.99 | 2.01 |
| Irrad., $0^\circ\text{C}$   | 3.64  | 1.07 | -4.19  | 0.87 | 0.95 |
| Unirrad., $0^\circ\text{C}$ | 0.09  | 1.46 | 0.02   | 0.99 | 1.14 |

**Table 9.2** Fit parameters of empirical fit eq. 9.6 found for the temperature dependence of the sensor noise rate.

While an increase in noise is expected due to the physical noise sources discussed in Ch. 3.2.3, their contributions are difficult to disentangle. Moreover, a breakdown of the noise hits reveals a more complete picture of their origin:

Fig. 9.26 shows, for the same measurement shown in fig. 9.24 (a), the number of hits per pixel as a fraction of the total number of noise hits. It can be seen that a large number of pixels remains noise-free despite the high noise rate, while the majority of hits can be attributed to only a handful of pixels ( $\sim 3\%$  of the total number of pixels). This is quantified for all measurements in fig. 9.27, where the pixel occupancy — here defined as the fraction of pixels recording at least one noise hit — is shown as a function of the bias voltage.

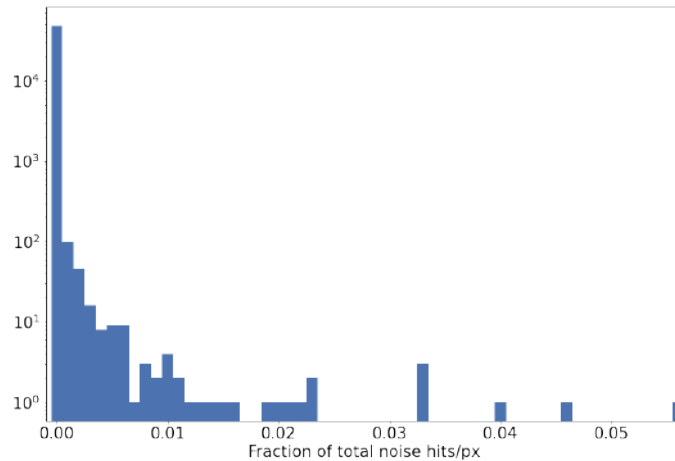


**Fig. 9.26** Number of noise hits per pixel as a fraction of the total number of noise hits.

A full understanding of the implications requires the context of the expected pixel occupancy given the number of noise hits recorded. This is taken into account in fig. 9.28, which shows the observed pixel occupancy as a fraction of the expected occupancy under the assumption that the recorded noise is distributed evenly across all available pixels. The kink at 50 V onwards for the sensor at 0 °C is explained by the expected occupancy saturating at 100%.

Taken together, figures 9.27 and 9.28 imply the following:

- The noise is not distributed evenly across the sensor but rather primarily originates from specific pixels
- The number of pixels crossing a certain noise threshold increases with the applied bias voltage
- The increasing deviation from unity in fig. 9.28 shows that the noise rate grows disproportionately to the number of affected pixels, i.e. the noise emitted by specific pixels increases with the bias voltage at a higher rate than the number of pixels affected by noise.

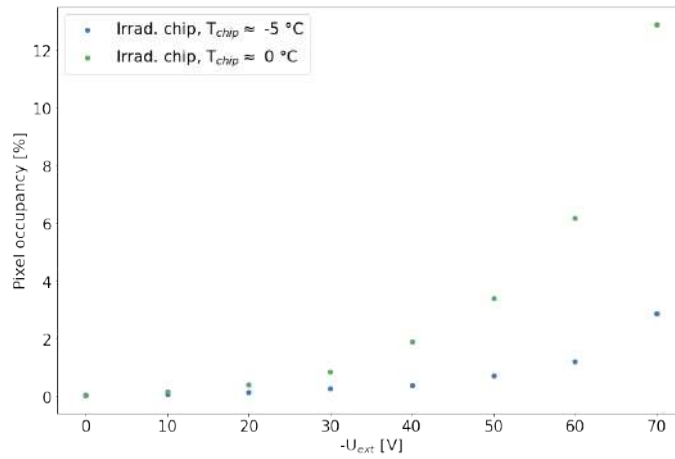


**Fig. 9.27** Noise pixel occupancy, i.e. the fraction of pixels recording at least one hit, as a function of the bias voltage.

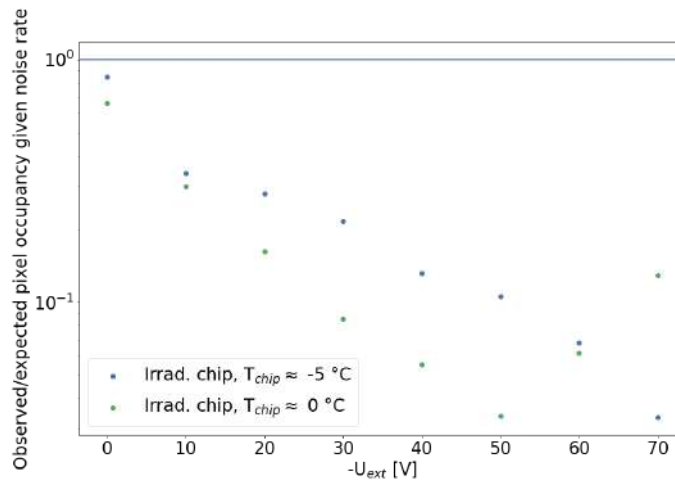


**Fig. 9.28** Observed noise pixel occupancy as a fraction of the expected occupancy under the assumption that the recorded noise is distributed evenly across all available pixels.

The pixel occupancy is shown as a function of the total number of hits recorded in fig. 9.29, which confirms the last point. A square root dependency of the occupancy on the number of hits is found, where

$$\text{Pixel occupancy} = \sqrt{m \cdot N}. \quad (9.7)$$

The best fit value is found to be  $(1.9 \times 10^{-8} \pm 1.2 \times 10^{-19})$ .

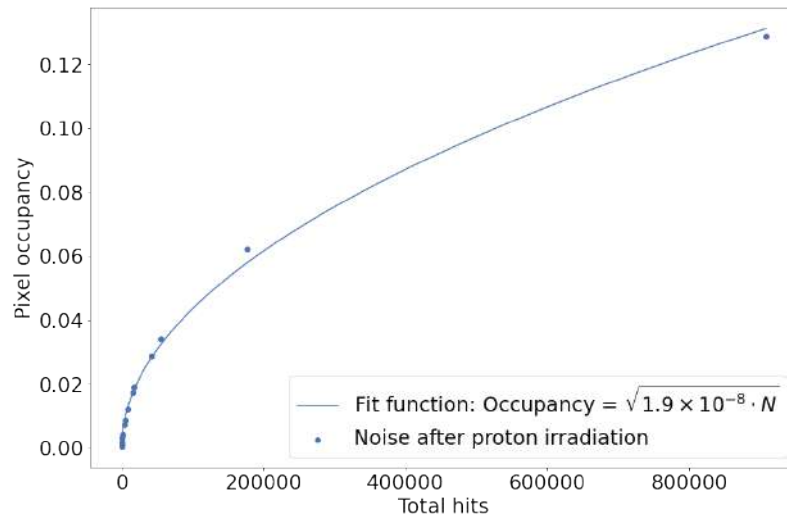


**Fig. 9.29** Pixel occupancy of noise hits as function of total number of hits.

### 9.2.9 Signal response

Several reference measurements of the sensor response to an  $^{55}\text{Fe}$  source were made before the proton irradiation campaign. All were carried out at room temperature and with a bias voltage of -60 V. The hitmap of one measurement with  $10^6$  hits is shown in fig. 9.30 as an example.

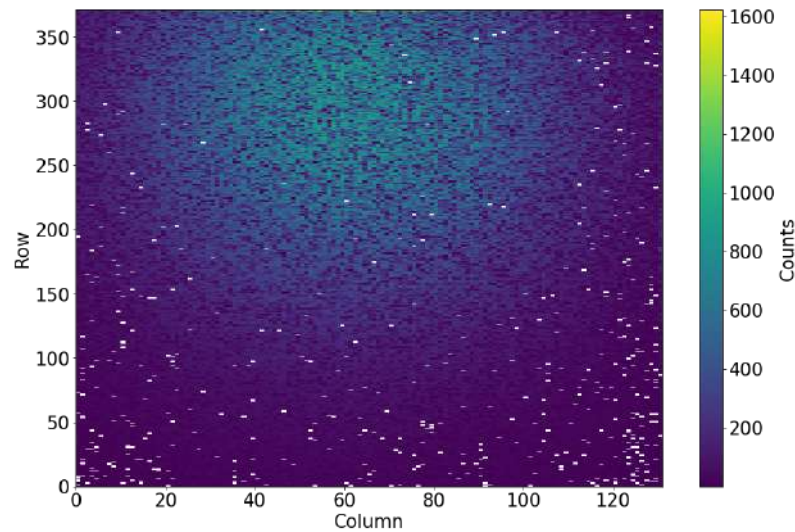


**Fig. 9.30**  $^{55}\text{Fe}$  hitmap of sensor before proton irradiation. Data taken with a bias voltage of -60 V.

Similar measurements were performed three months after the irradiation campaign. In order to suppress noise and ensure the sensor remains operable at all, these measurements were taken while the chip was cooled to below  $5\text{ }^\circ\text{C}$ , and generally at a bias voltage below -60 V. As a direct comparison to the reference measurement shown above, one post-irradiation measurement at -60 V bias voltage and with a total of  $10^5$  hits is shown in fig. 9.31. Aside from the absence of a beamspot, the reduced pixel occupancy also observed in section 9.2.8 is immediately noticeable in the hit map and quantified below.

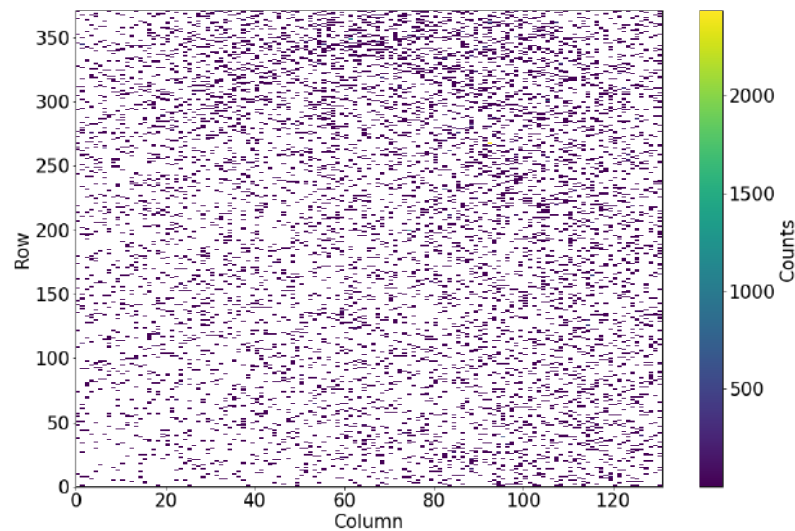


**Fig. 9.31**  $^{55}\text{Fe}$  hitmap of sensor after proton irradiation. Data taken with a bias voltage of  $-60$  V.

The pixel occupancy is shown as a function of the applied bias voltage in fig. 9.32. All measurements involved consist of a total of  $10^5$  hits and were taken at  $5$  °C. The  $^{55}\text{Fe}$  source was not moved between measurements.

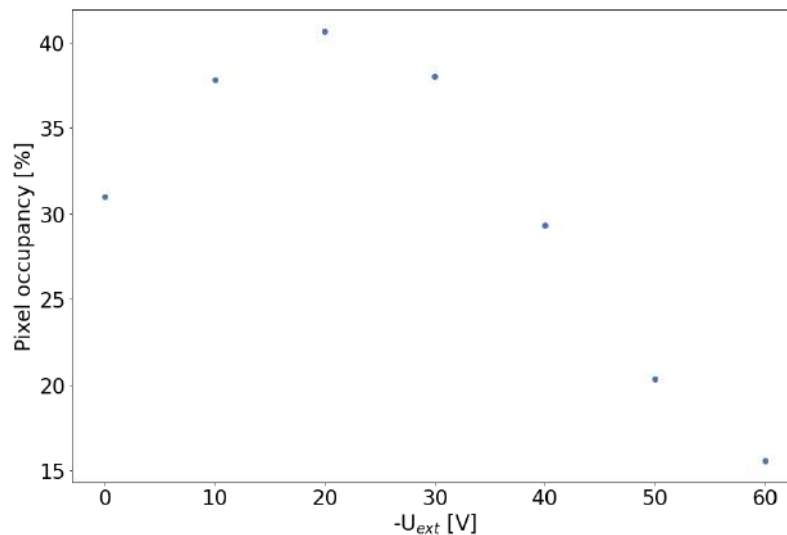


**Fig. 9.32** Pixel occupancy of a  $^{55}\text{Fe}$  measurement after proton irradiation as function of bias voltage.

The pixel occupancy of these reference measurements evidently exhibits a dependence on the bias voltage. Unlike the occupancy during noise measurements shown in fig. 9.27, which increased with increasing bias voltage, the maximum occupancy during  $^{55}\text{Fe}$  irradiation is reached at  $U_{\text{ext}} = -20$  V. Given the lack of comparison data, it is not currently clear whether the the behaviour shown in fig. 9.27 is reproducible, and if so, whether the voltage dependence is a consequence of readout limitations. It should be mentioned, however, that none of the measurements involved shows any obvious signs of the decoding errors often observed during the operation of the AP 3.1. Such errors preferentially appear at high rates and are studied in detail in [36].

A direct comparison between the pixel occupancies of the sensor before (blue) vs. after (red) proton irradiation is shown in fig. 9.33 as a function of the total number of hits. It should be noted that the distance  $r$  between source and sensor is not corrected for

across measurements; given that the source can be approximated as a point source, a  $1/r^2$  dependency is expected that would shift the curve. While an exact match between measurements therefore cannot be expected, the effect of this is likely negligible within the context of the measurements presented.

The hit-dependent pixel occupancy of the noise shown in fig. 9.27 is included for reference (green), along with the corresponding fit function found in section 9.2.8. Since experience has shown that the sensor is somewhat unstable and prone to inconsistent behaviour post-irradiation, measurements at all voltage settings are included for better statistics and in order to gain a broader picture of the measurements.

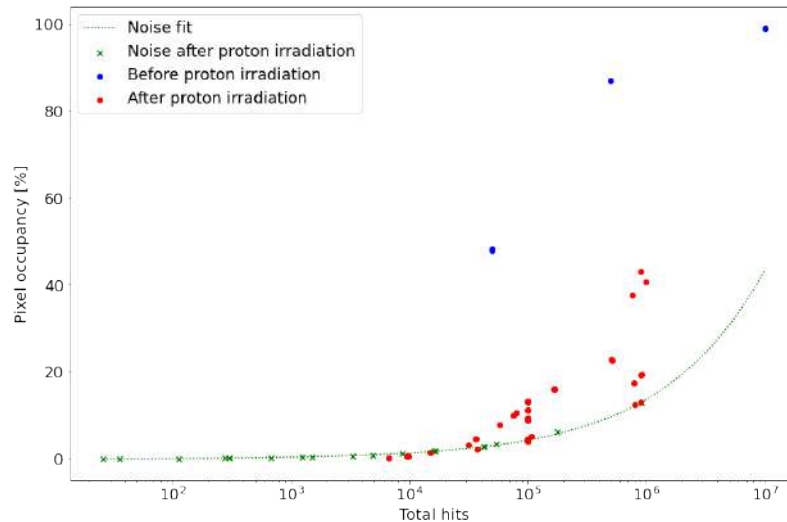


**Fig. 9.33** Comparison of pixel occupancy as a function of total number of hits pre- and post-proton irradiation. The post-irradiation sensor noise (green) measured in section 9.2.8 is included for context.

Fig. 9.33 shows that while the pixel occupancy of the sensor increases with the total number of hits after irradiation, it consistently remains lower than that seen before irradiation. Even under the conservative assumption that only unoccupied pixels sustained damage during the proton irradiation, fig. 9.33 implies the loss of around half the pixel matrix given that the highest achieved occupancy is 43%. Compared to the occupancy for the same number of hits pre-irradiation, this corresponds to a reduction by more than 50%.

Combined with the conspicuous absence of a distinguishable beam spot, it may be concluded that reliable data-taking is no longer possible at the standard settings after a proton fluence of  $1 \times 10^{14}$  neq/cm<sup>2</sup>. This fluence is less than one-fifth of the lifetime fluence expected for the MightyPix, which is — at the low end — estimated to be  $6 \times 10^{14}$  neq/cm<sup>2</sup> [37].

## 9.3 Long-term X-ray irradiation of a powered ATLASPix 3.1

In an effort to disentangle the effects of NIEL and IEL (also referred to as Total Ionising Dose, or TID) damage, a previously unirradiated ATLASPix 3.1 was subjected to a total of 78 hours of X-ray irradiation in four irradiation steps, and under varying starting conditions.

While an analysis of the dose dependence of the observed effects is of interest, a stringent calculation of the dose is difficult given the available data and in the presence of several

confounding factors.

As was seen in Ch. 8.2, the X-ray spectrum of tungsten expected in silicon consists of several peaks in addition to a Bremsstrahlung spectrum. Moreover, the sensor was irradiated through the back for the first two measurements and through the front for the last two. The resulting spectra are expected to differ since the depletion zone is located closer to the front side of the sensor, resulting in different amounts of silicon bulk for an X-ray photon to pass through before entering the radiation-sensitive area. Considering that the width of the depletion zone is not truly known either, the average energy deposited by an X-ray photon can only be roughly estimated.

While the size of a beam spot produced by a 5 mm collimator is theoretically given by a trivial calculation, the use of a protective cap during irradiation complicates things by introducing additional bulk material that photons need to pass through before reaching the active sensor area. As is shown in section 9.3.5, the recorded beam spot is also cut off at the top due to increased thickness of the cap. As a result, certain sensor areas were exposed to radiation of reduced, but otherwise poorly known and varying intensities.

Despite the difficulties in the dose calculation mentioned above, the doses after each irradiation step are broadly estimated under the assumption that the average photon deposits an energy of 15 keV, the depletion depth of the AP 3.1 is 50  $\mu\text{m}$ , the photons arrive at a rate of 630 kHz/mm<sup>2</sup> for at an anode current of 1 mA and 125 kHz/mm<sup>2</sup> for an anode current of 0.2 mA<sup>4</sup>, and the beam spot size is 5% of the total sensor area. The resulting doses after each irradiation step are listed in table 9.3. It should be noted that only the sensor area within the beamspot of the 5 mm collimator during TID1 and TID2 received the full cumulative dose of 3.1 kGy, while the remaining sensor was only subject to the cumulative radiation of 2.2 kGy collected during TID3 and TID4.

An overview of the long-term measurements is provided in table 9.3.

|             | Duration | $I_{\text{anode}}$ | Collimator | Dose     | Date       |
|-------------|----------|--------------------|------------|----------|------------|
| <b>TID1</b> | 16 hrs   | 0.2 mA             | 5 mm       | 150 Gy   | 07.07.2022 |
| <b>TID2</b> | 16 hrs   | 1 mA               | 5 mm       | 750 Gy   | 12.07.2022 |
| <b>TID3</b> | 22 hrs   | 1 mA               | –          | 1.05 kGy | 20.12.2022 |
| <b>TID4</b> | 24 hrs   | 1 mA               | –          | 1.15 kGy | 22.12.2022 |

**Table 9.3** Overview of long-term X-ray measurements. All irradiations took place using a tungsten anode, and while the sensor was biased with  $U_{\text{ext}} = -60\text{V}$ . The doses listed are rough estimates. It should be noted that only the sensor area within the beamspot of the 5 mm collimator received the doses listed for TID1 and TID2.

### 9.3.1 Beam-induced current and breakdown voltage during irradiation

Reference I-V curves were taken before any long-term irradiations took place. The I-V curves are shown in fig. 9.35 and were taken while the sensor was irradiated at increasing anode currents, and without use of a collimator. The sensor was irradiated for around five minutes for each I-V curve.

From these, the beam-induced current at -60 V bias voltage was extracted and is shown in fig. 9.34. A fit through the currents observed while the chip was actively under irradiation shows a linear dependence on the anode current, which is directly related to the rate of X-ray photon emission. The deviation of the observed leakage current at 0 mA anode current from the applied fit can be attributed to the temperature evolution during the measurement, which is shown in red. While the I-V curves were taken at increasing anode currents overall, the measurement without X-ray current was taken last and as

<sup>4</sup> These estimates are based on the fit of data set 1 (see fig. 7.8) of the rate measurements performed in Ch. 7.4.

such, while the temperature in the X-ray chamber was highest. The first data point therefore does not conform to the pattern of the temperature increasing along with the anode current. The error bars on the measured current reflect the estimated expected deviation in leakage current given the distance to the average temperature during the measurement. This deviation is calculated from the parameters shown in fig. 9.13 as a proxy; while these numbers derive from measurements of the same sensor as used during the TID measurements presented here, it may be expected that the resulting expected shift is more accurate for the measurement at 0 mA anode current as the data shown in fig. 9.13 was taken without the influence of irradiation. The data points are weighted accordingly for the fit.

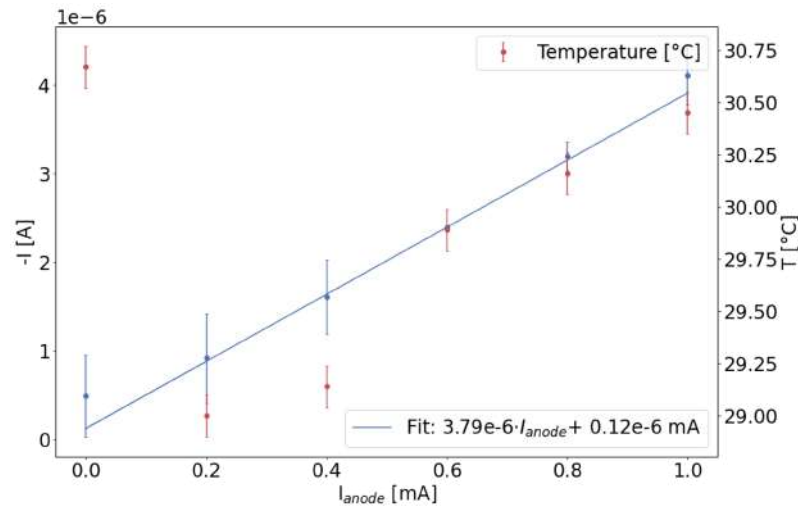


**Fig. 9.34** Beam-induced current extracted from I-V curves at -60 V bias voltage (blue), and temperature associated with each measurement (red).

Following the same line of reasoning as in Ch. 9.2.3, where the energy of an average X-ray photon emitted by a tungsten anode is conservatively estimated to be 15 keV following the results presented in Ch. 8.2, and under the assumption that the photon fluxes correspond to the rates found in Ch. 7.4, the beam-induced current for an anode current of 1 mA is expected to be no larger than 200 nA.

This value is, with a factor of 20, evidently far below the beam-induced current shown in fig. 9.34. This discrepancy remains even after correcting for the inherent leakage current under the conservative assumption that it contributes maximally to the current by subtracting it from all observed beam-induced currents.

It is not clear at this stage what causes the deviation of the observed from the expected beam-induced current and further studies are needed in order to determine its source.

The I-V curves presented in fig. 9.35 show that the breakdown voltage remained stable at -69.5 V while the sensor was actively irradiated with increasing anode currents.

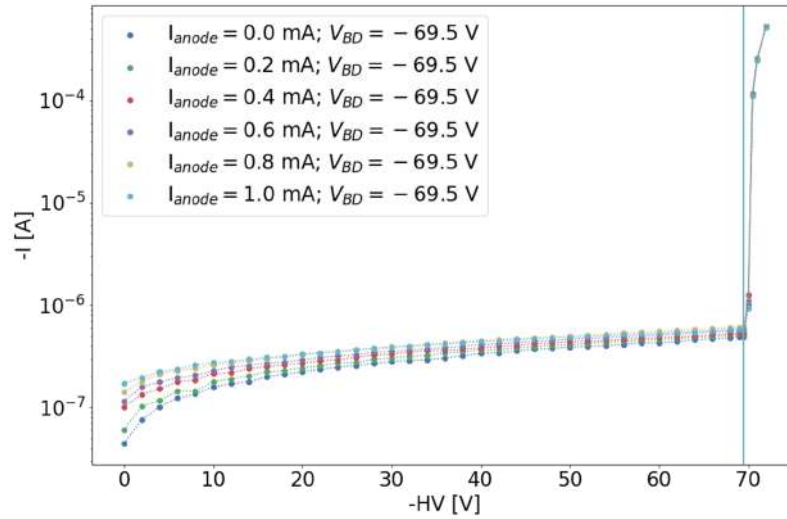


**Fig. 9.35** Breakdown voltage during active X-ray irradiation with various anode currents.

### 9.3.2 Long-term X-ray irradiation

A total of four long-term X-ray irradiation campaigns were carried out using the previously largely unirradiated ATLASPix 3.1, two of which (TID1 and TID2) took place in July, and two (TID3 and TID4) in December 2022. A 5 mm collimator was used for TID1 and TID2 in an effort to protect the sensor periphery from radiation, while none was used for TID3 and TID4. As a result, the entire sensor including its periphery was irradiated during TID3 and TID4. During TID1 and TID2, the sensor was powered via the GECCO board and irradiated through the back due to geometric constraints of the measurement infrastructure. During TID3 and TID4, it was irradiated through the front using the custom adapter discussed in Ch. 6.1.2. All irradiations took place while the sensor was biased at -60 V. The anode current was 0.2 mA for TID1, and 1 mA for the remaining measurements. Between July and December, the sensor was in frequent use and was regularly configured, and occasionally irradiated using a  $^{55}\text{Fe}$  source. While some low-temperature measurements were taken using the cooling setup described in ch. 6.1.4, the chip was generally stored at room temperature.

I-V curves were taken before and after all TID irradiations. The leakage current was measured after TID3 and TID4.

A number of core observations were made during the long-term irradiations that are pre-emptively summarised at this point in an effort to aid comprehension amid the large number of confounding factors found in the measurements. These observations are discussed in detail below.

1. The initial beam-induced current jump increased by a factor of three after an estimated total ionising dose of 2 kGy.
2. The leakage current exhibits an ingrow behaviour during the first  $\sim 100$  seconds of each measurement. Given that this also occurs when the sensor is not biased, this is indicative of current from the LV power supplies leaking into the bias circuit.
3. The breakdown voltage shows an overall decrease after long-term X-ray irradiation.

The beam-induced current during the four long-term measurements summarised in table 9.3 are shown together in fig. 9.36 for easy comparison, and individually along with the associated temperature measured in the X-ray chamber for a more detailed view in fig. 9.37.

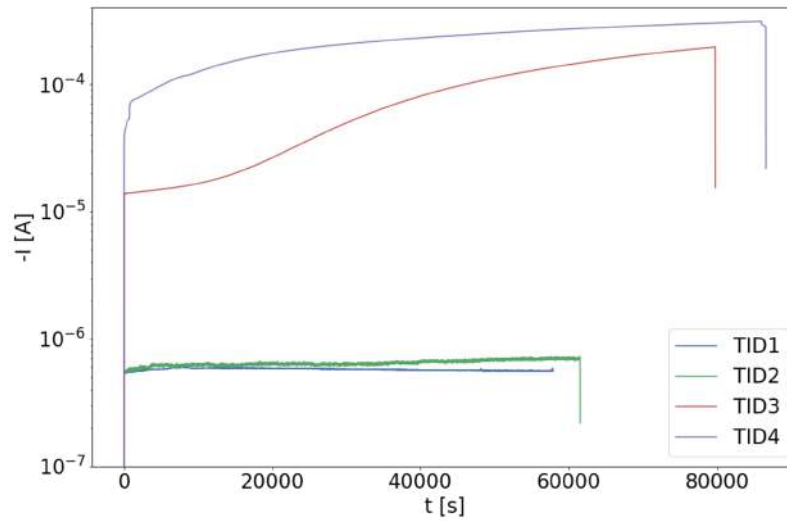


**Fig. 9.36** Overview of beam-induced currents recorded during long-term TID measurements.

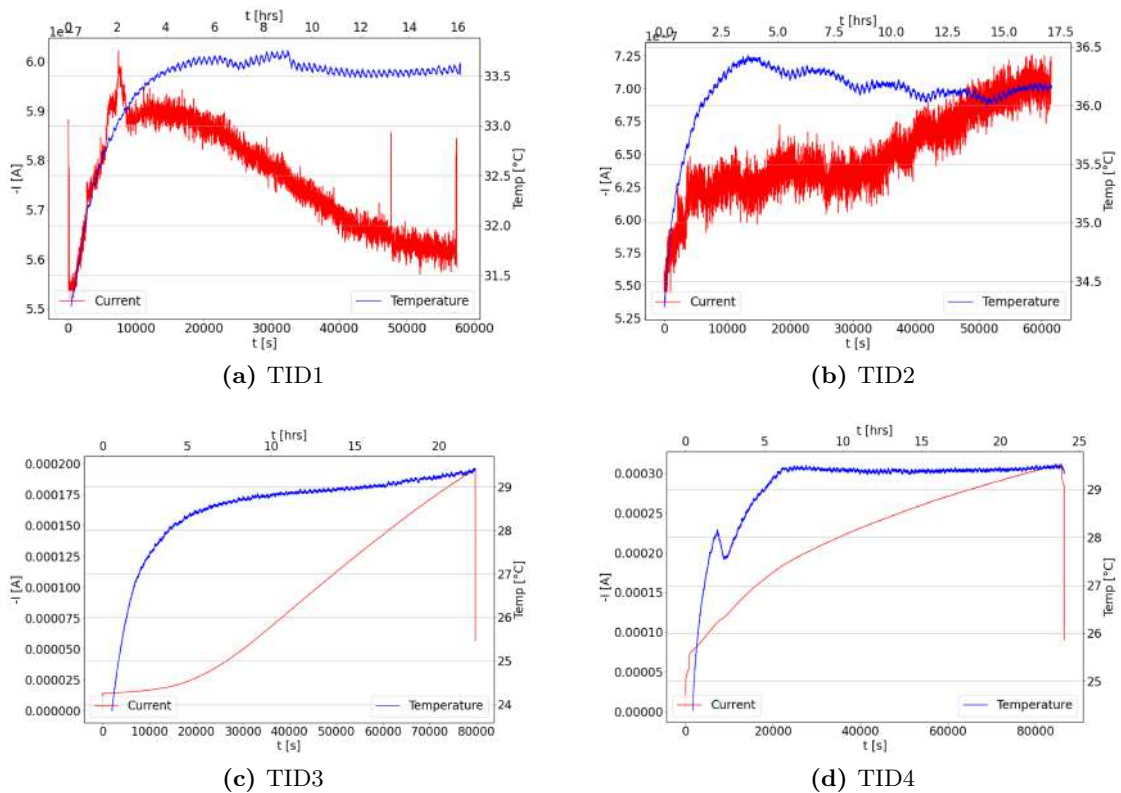


**Fig. 9.37** Zero-suppressed time evolution of beam-induced currents and temperature inside X-ray chamber during long-term irradiation. Note the zero suppression.

It is evident from fig. 9.37 that the time evolution of the beam-induced current is vastly different across irradiations. This can partially be explained by taking into account the influence of variables like the presence of a collimator, the applied bias voltage, and the anode current.

The impact of the 5 mm collimator on the beam-induced current is apparent in the comparatively low currents of TID1 and TID2. Given that the beam spot covers between at most 5% of the total sensor area (see section 9.3.5), the order of magnitude of TID1 and TID2 matches that of the uncollimated measurements when scaled accordingly.

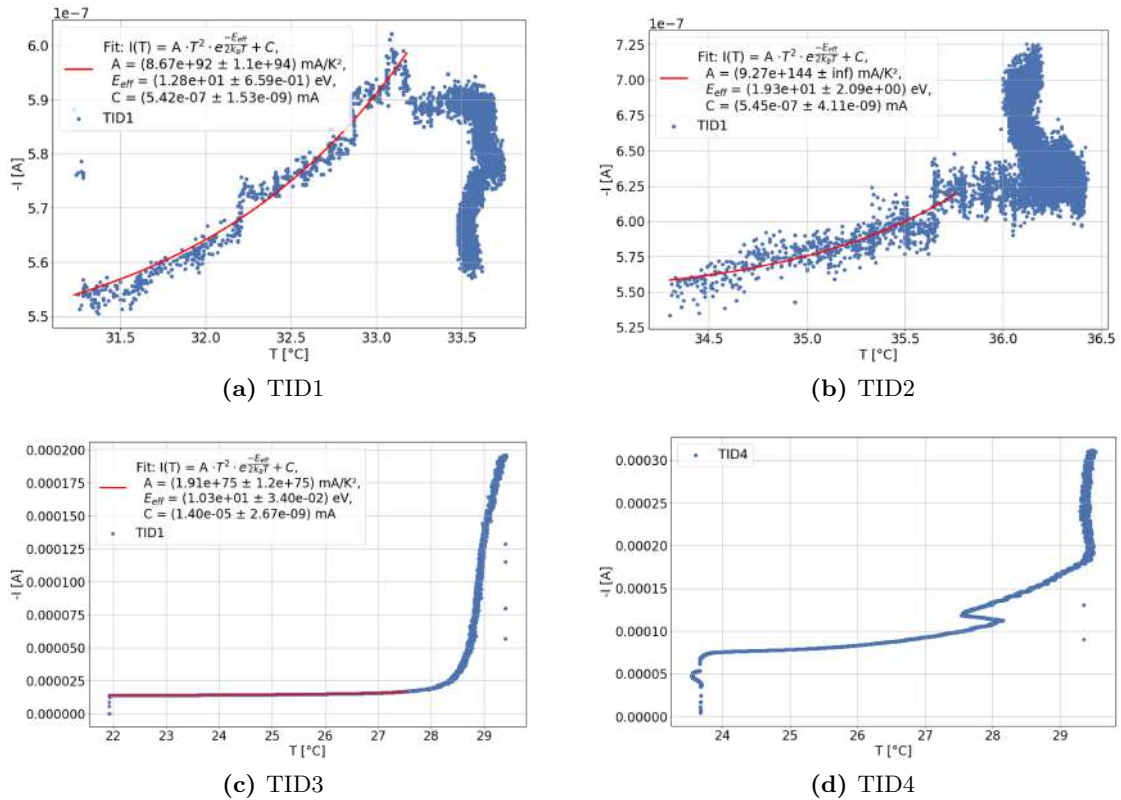


**Fig. 9.38** Temperature dependence of beam-induced current during long-term X-ray irradiation.

The overall trend of the beam-induced current over time appears to approximate logarithmic growth for all irradiations except TID1, which instead decreases after an initial ingrow period. This difference may be explained by two concurrent effects: the temperature dependence of the leakage current, and the comparatively low photon rate during TID1 resulting from the low anode current combined with the use of a collimator.

Fig. 9.38 shows the recorded current as a function of the temperature inside the X-ray chamber. It is immediately clear that the initial ingrow period can mostly be attributed to an increase in temperature. Following the discussion about the temperature dependence of the leakage current in Ch. 9.2.4, eq. 3.19 is fitted to the observed data for the sake of completeness; it may, however, be assumed that the temperature dependence of a sensor under active irradiation deviates from that of a sensor whose dominant current contribution is the generation current  $I_{gen}$ . It should also be noted that even in the regime where the temperature dependence dominates the current evolution, the beam-induced current increase seen after an equilibrium is reached remains a contributing factor, such that the current cannot be expected to strictly follow the temperature dependence shown in 9.2.4. It is reasonable to assume that — aside from the temperature dependence — the observed current evolution is the result of two time constants, one describing the charging of the sensor by the X-ray beam, and one the discharging process. While the collimator is also used for TID2, whose time evolution has no regime of strict decay, the beam intensity for TID1 is reduced by a factor of five compared to that of TID2. The resulting lower charge introduction rate conceivably caused discharging to become the dominant contribution.

The average total current increases per hour after the temperature has stabilised, which is assumed to be after five hours, are listed in table 9.4, along with the current directly after turning on the X-ray beam. The numbers are broad estimates intended to put the measurements into perspective given the difference in starting conditions.

|             | Average current increase/hour | Initial beam-induced current [ $\mu\text{A}$ ] |
|-------------|-------------------------------|--|
| <b>TID1</b> | -2.5 nA                       | 0.55   |
| <b>TID2</b> | 5.2 nA                        | 0.53   |
| <b>TID3</b> | 10.0 $\mu\text{A}$            | 13.6   |
| <b>TID4</b> | 7.6 $\mu\text{A}$             | 66.8   |

**Table 9.4** Average current increase per hour after reaching temperature equilibrium, which is assumed to be after 5 hours, and observed current directly after turning on the X-ray beam. TID1 and TID2 were taken using a 5 mm collimator.

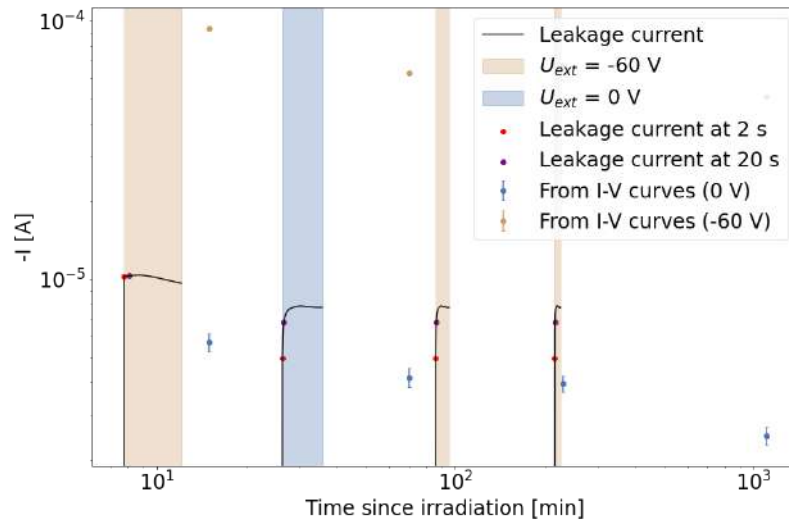
Compared to the pre-irradiation current found using the I-V curves shown in section 9.3.1, which was on the order of 4  $\mu\text{A}$  for an anode current of 1 mA, the post-irradiation current jump of TID3 and TID4 have evidently increased. As a collimator was used for TID1 and TID2, it is more difficult to compare their initial current jumps to the values found from the I-V curves. A naive estimate can be made under the assumption that firstly, the current scales directly with the irradiated area, secondly, that the beam spot is at maximum 5% of the total sensor size, and thirdly, the beam-induced current responds to temperature changes according to the equation shown in fig. 9.13. The resulting collimator- and temperature-adjusted pre-irradiation current from the I-V curves is around 0.2  $\mu\text{A}$  for  $I_{\text{anode}} = 0.2$  mA, and 0.4  $\mu\text{A}$  for  $I_{\text{anode}} = 1$  mA, which is consistent with the observed currents listed in table 9.4.

While TID3 and TID4 were taken under the same starting conditions and the irradiation time-adjusted increases in current are of the same order of magnitude, it is interesting to note the discrepancy between their initial current jumps. The reason for this mismatch becomes clear when taking into account the leakage current of the sensor before turning on the X-ray beam: at 53.3  $\mu\text{A}$ , it two orders of magnitude larger than the current of 0.25  $\mu\text{A}$  at -60 V bias voltage extracted from the I-V curve measured directly before TID3. Subtracting the initial leakage current from the total current measured once the beam was turned on yields a beam-induced current jump of 13.4  $\mu\text{A}$  for TID4, which matches the value seen for TID3. It can be concluded that the beam-induced current jump is a factor of three higher than before irradiation after an estimated maximum total dose of 2 kGy, and that this value does not change after a further 1 kGy of irradiation.

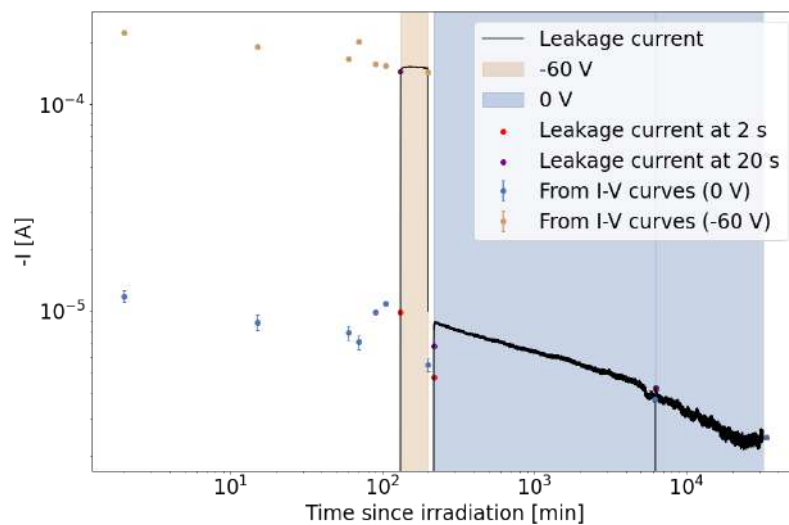
### 9.3.3 Leakage current after long-term irradiation

While I-V curves were taken before and after all long-term irradiations, the temperature-, configuration, and light dependence of the leakage current as well as the different time intervals before and after the irradiation at which measurements were performed means that a global analysis across all measurements is not feasible. As TID1 and TID2 are additionally expected to have affected only a small percentage of the total sensor area due to the use of a collimator, only the development of the leakage current after TID3 and TID4 is examined more closely.

After TID3 and TID4, the time evolution of the leakage current was monitored using two approaches: by taking I-V curves at irregular intervals, and via long-term leakage measurements ranging in duration from a few minutes to 18 days. Fig. 9.39 shows an overview of all leakage measurements as a function of time since the last long-term irradiation. The data is colour-coded to distinguish between measurements with and without an applied bias voltage. No temperature corrections were applied in the overview.



(a) Leakage currents recorded after TID3



(b) Leakage currents recorded after TID4

**Fig. 9.39** Overview of leakage currents measured after TID3 and TID4.

While the leakage currents seen in fig. 9.39 follow an overall trend of decreasing magnitude over time for all measurement types, it is notable that the leakage currents extracted from I-V curves are consistently lower than the corresponding long-term leakage currents at 0 V bias voltage, and higher at  $U_{\text{ext}} = -60$  V. The latter could conceivably be explained by charge-up effects caused by the voltage switching involved in the taking of I-V curves. The former is the result of a currently unexplained ingrow effect observed during the first  $\sim 100$  seconds of the leakage measurements, an example of which is shown in fig. 9.40. The leakage currents recorded at 2 seconds are indicated in red in order to visualise the currents at a timescale more comparable to that of measurement during the I-V curves, where each data point is the statistical average of 5 measurements taken over the course of 5 seconds. Similarly, the leakage current at 20 seconds is indicated in purple as it takes the HV power supply 17 seconds to reach the full bias voltage of -60 V. For biased measurements, therefore, this is the earliest time at which the target current is recorded. For unbiased measurements, it is an additional data point visualising the time evolution of the charge-up effect. This ingrow stage is particularly unexpected for the measurements where no bias voltage is applied to the sensor. As the sole source of the observed current are the low voltage power supplies, this observation implies that charge from the low voltages leaks into the bias circuit. On a more practical note, it means that any measurements taken must be allowed sufficient time to reach equilibrium.

Taking into account the charge-up effect, the time evolution of the leakage current is consistent across I-V curves and long-term leakage measurements.

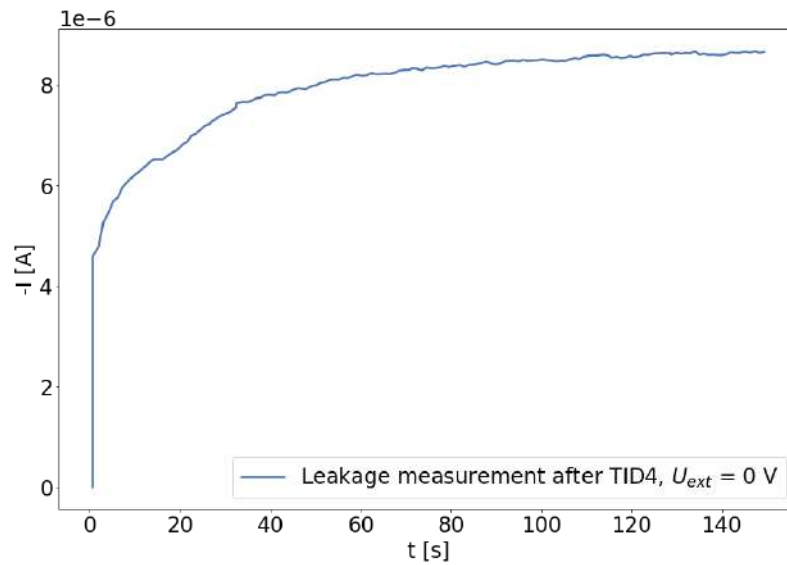


**Fig. 9.40** Close-up view of leakage current ingrow effect seen during the first 100 seconds of a leakage measurement.

A time constant for the time evolution of the leakage current is obtained for the two longest measurements after TID4, the first of which was taken over the course of three, the second over 18 days. The measurements, along with the temperature evolution and temperature dependence, are shown in fig. 9.41. The fitted curves are found in fig. 9.42.

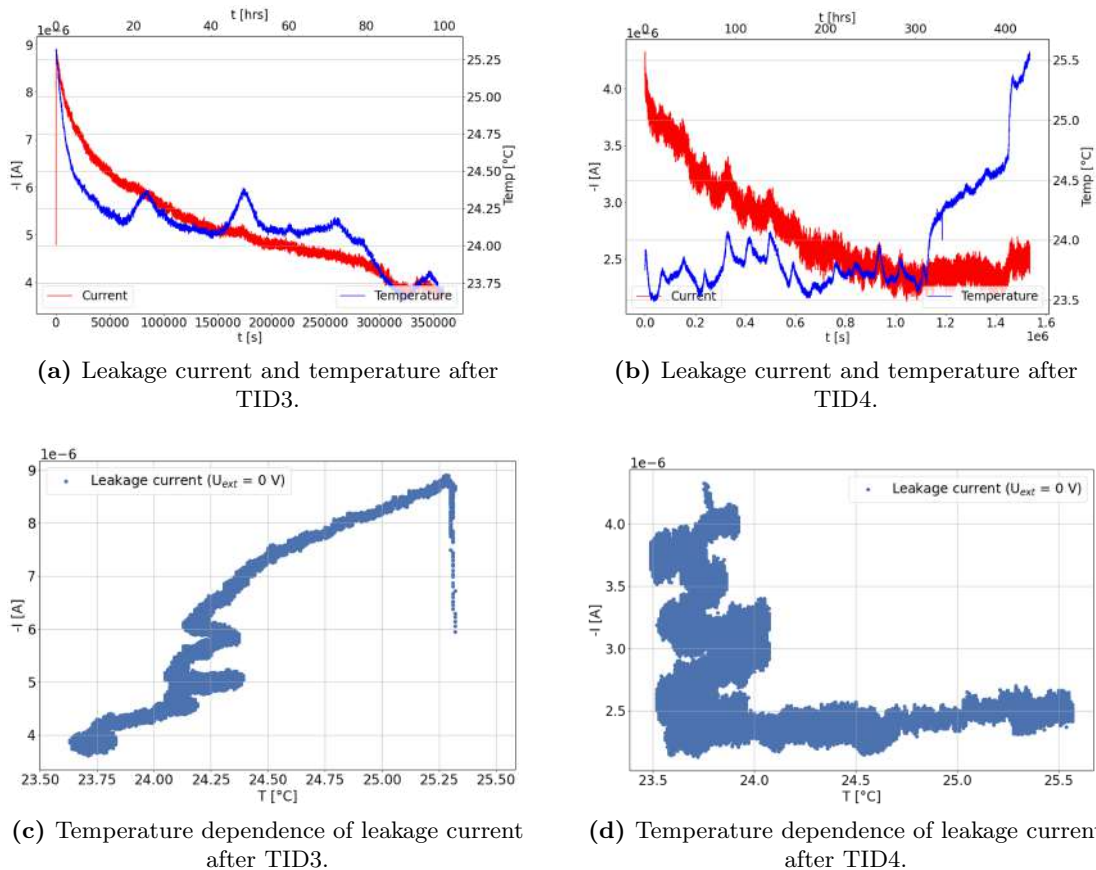
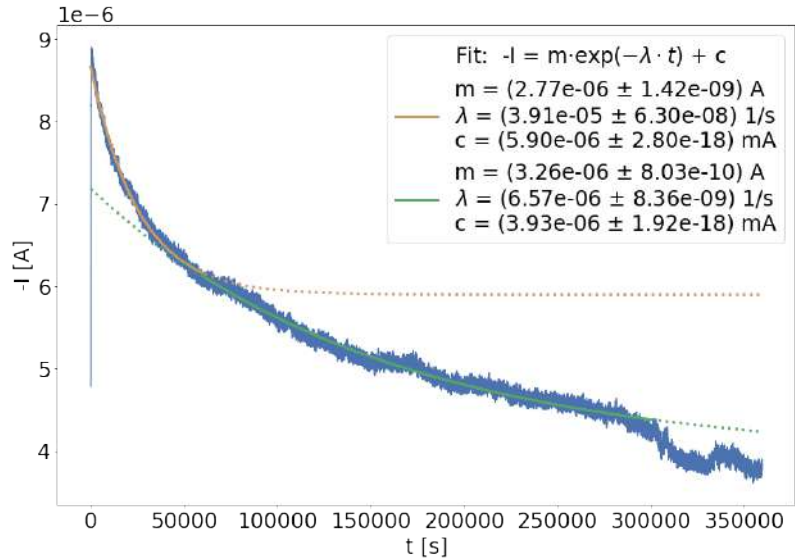
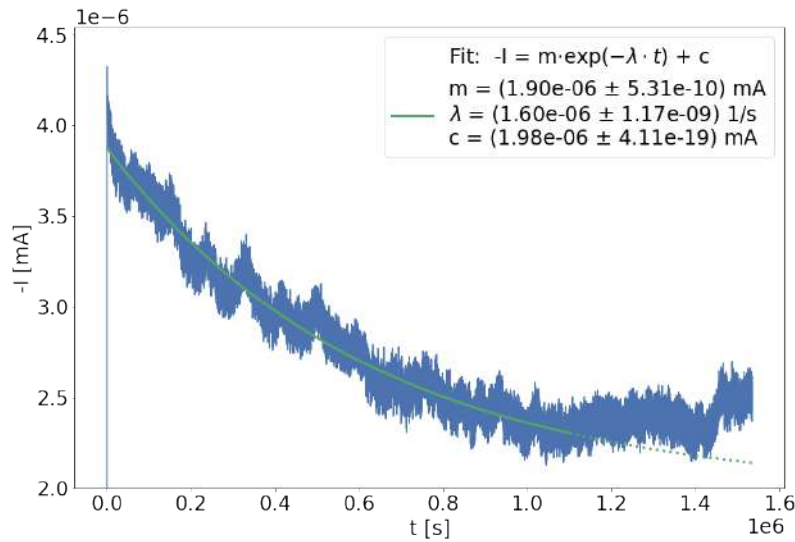


**Fig. 9.41** Temperature dependence of the leakage current after long-term irradiation.



(a) TID3



(b) TID4

**Fig. 9.42** Time evolution of leakage current after long-term X-ray irradiation. An exponential fit is applied to find a time constant.

The temperature dependence of the leakage current measurements is evident from fig. 9.41 and is accounted for by fitting regimes of different temperatures separately. For the regime of the largest temperature stability, the time constant resulting from the exponential fit function

$$-I = m \cdot \exp(-\lambda \cdot t) + c \quad (9.8)$$

is  $(6.57 \times 10^{-6} \pm 8.36 \times 10^{-9})$  1/s for TID3, and  $(1.60 \times 10^{-6} \pm 1.17 \times 10^{-9})$  1/s for TID4.

Comparing the leakage current of  $I_{leak} \approx -2.3 \times 10^{-6}$  A 18 days after TID4 to the current recorded at 0 V during a pre-irradiation I-V curve, where  $I_{leak} \approx -4 \times 10^{-8}$  A, it can be concluded that the leakage current after an estimated maximum dose of 3.2 kGy of X-ray irradiation, which is  $< 1\%$  of the TID expected for the MightyPix [37], is two orders of magnitude larger than before the irradiation. It should be noted that the leakage current calculation does not take into account the charge-up effect discussed above, which could

potentially increase the pre-irradiation current, nor is the temperature adjusted for. The latter effect is expected to counteract the former as the temperature after TID4 was around 6 °C below that during the pre-irradiation I-V curve. At the same time, the dose estimate is conservative considering the majority of the sensor area was shielded from TID1 and TID2, and therefore was subjected only to radiation during TID3 and TID4.

### 9.3.4 Impact of long-term irradiation on breakdown voltage

The breakdown voltage of the sensor was measured at irregular time intervals after each long-term irradiation. Their time evolution is shown in fig. 9.43. The breakdown voltages immediately before TID3 and TID4 are included for reference, as well as the breakdown voltage measured before any long-term irradiation. It should be noted that the reference measurement before TID4 is simultaneously the last data point after TID3; the identical points in question are indicated with a square marker.

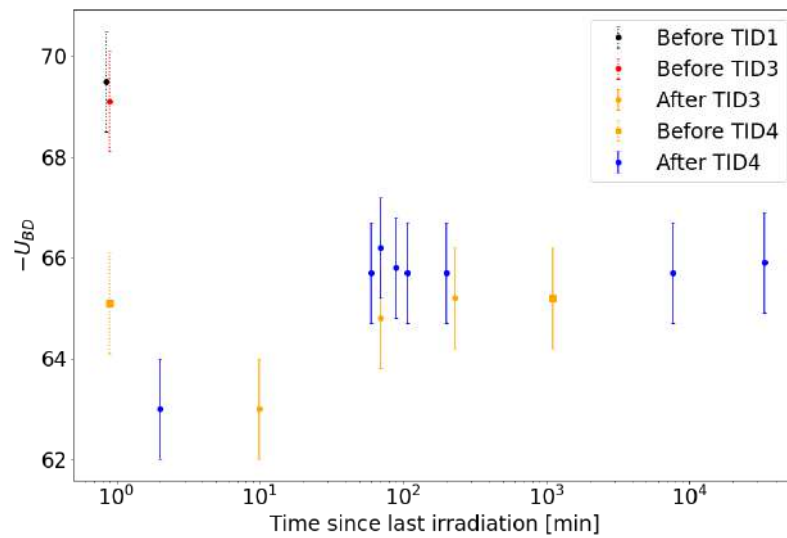


**Fig. 9.43** Time evolution of breakdown voltage after long-term irradiation. A reference measurement of the breakdown voltage before any long-term irradiation is included in black.

Two observations can be made from fig. 9.43: firstly, the breakdown voltage drops after long-term irradiation. For both TID3 and TID4, the breakdown voltage immediately after irradiation is around  $(-63.0 \pm 1.0)$  V. The pre-irradiation breakdown voltage, however, was larger for TID3 than for TID4; the total drop was therefore larger for TID3 despite the total irradiation dose being lower than for TID4.

Secondly, the breakdown voltage is subject to a time-dependent recovery effect that plateaus after around five hours. The sensor recovered to a similar value of around  $(-66.0 \pm 1.0)$  V after both TID3 and TID4, which is significantly lower than the pre-irradiation breakdown voltage of  $(-69.5 \pm 1.0)$  V.

It is worth mentioning that while a certain temperature dependence of the breakdown voltage has been observed (see Ch. 9.2.5), this effect is only visible at sub-zero temperatures and on scales where the temperature differs by  $\mathcal{O}(10)$  °C. Any variations in temperature are therefore not expected to play a role in the observed recovery effect.

### 9.3.5 Signal response

As no reference Fe-55 spectra were taken before the X-ray campaign and measurements after TID4 do not yet exist, a stringent analysis of the sensor response to the long-term X-ray irradiation campaign cannot be conducted. Even so, observations were made in

$^{55}\text{Fe}$  measurements taken between TID2 and TID3 that are worth mentioning qualitatively.

The hitmap of a  $^{55}\text{Fe}$  measurement taken four months after TID2 is shown in fig. 9.44. The measurement was taken at a bias voltage of -60 V and at a temperature of around 18 °C. The lack of a clear beam spot is explained by the relatively large distance between the sensor and the  $^{55}\text{Fe}$  source, which was deliberately placed farther away in order to improve the operation stability of the sensor. The colourscale of the hitmap is manually restricted to 10 counts at the upper end to enhance the contrast between the diffuse — but existent — beam spot.

Fig. 9.44 shows area around 30 pixels wide and 40 pixels high surrounding column 50 and row 300 with a markedly reduced pixel occupancy compared to the remaining sensor. This is the area of the TID1 and TID2 beamspot; the width of 30 pixels corresponds to a size of around 4.5 mm and is reflective of the 5 mm collimator used during the measurements. The height of 40 pixels translates to 2 mm, which is smaller than expected. The asymmetry can most likely be attributed to the use of a protective cap during the measurements, which adds bulk material for impinging radiation to pass through before reaching the sensor. The thickness of the cap is not uniform across the sensor due to the placement of the cap clasp, which is reflected in the shape of the beamspot.

Given that the immediate beamspot area behaves noticeably differently than the remaining sensor, this observation indicates that the reduced occupancy is a consequence of damage to the active pixel matrix, not the periphery.

It should be emphasised that the data was taken 4 months after the completion of TID2. The measurement demonstrates that a total ionising dose of less than 900 Gy is sufficient to have a lasting impact on the pixel matrix in the irradiated sensor area.

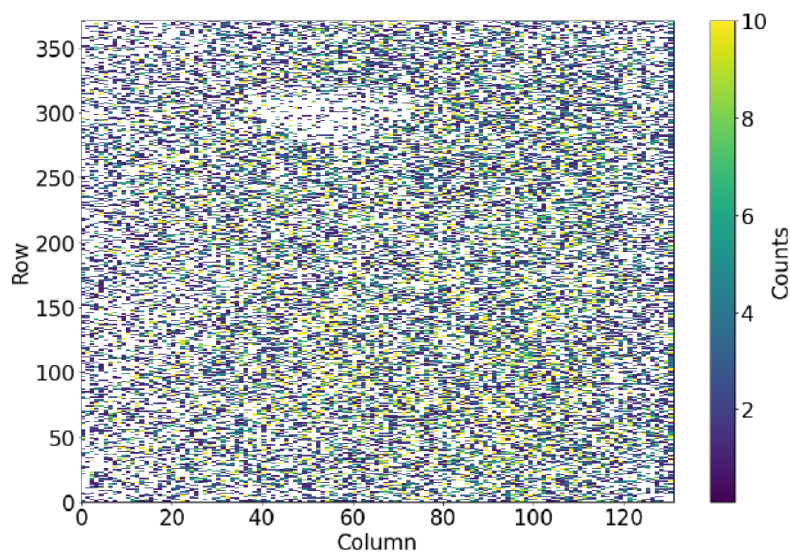


**Fig. 9.44** Hitmap of a  $^{55}\text{Fe}$  measurement. Data taken 4 months after TID2.

# Summary and outlook

On its mission to find evidence of New Physics Beyond the Standard Model, the LHCb experiment is foreseen to undergo a major upgrade during LS4 of the LHC in 2033. As one cornerstone of this upgrade, the Scintillating Fibre tracker is set to be replaced by the MightyTracker, a hybrid downstream tracking system combining the current scintillating fibre technology with radiation-hard HV-MAPS sensors in its innermost regions. The harsh radiation environment in the upgraded detector requires a good understanding of the radiation damage expected for its detectors.

This thesis presents a first effort to develop suitable measurement infrastructure and characterisation routines for the LHCb group in Heidelberg in preparation for the arrival of the MightyPix sensor.

As a proxy for the MightyPix, the work carried out in the scope of this thesis was conducted using the ATLASPix 3.1, which is a HV-MAPS sensor of similar build. In an effort to eventually disentangle the damage contributions from ionising and non-ionising radiation, separate irradiation campaigns were carried out using X-ray photons and protons. During these, two powered and biased ATLASPix 3.1 sensors were irradiated with a total proton fluence of  $\phi_{\text{eq}} \approx 1 \cdot 10^{14} \text{ n}_{\text{eq}}/\text{cm}^2$ , and a total ionising dose of approx. 3.2 kGy, respectively. These values correspond to a fifth of the total neutron-equivalent fluence, and less than 1% of the TID expected for the MightyPix.

Several key observations were made, particularly regarding the breakdown voltage and the leakage current of the ATLASPix 3.1 after irradiation:

Analyses of the beam-induced current and the leakage current indicated a charge-up effect for both proton and X-ray irradiation, associated with time-dependent discharging behaviour after the irradiation. The time constant of discharging was determined to be on the order of  $10^{-6} \text{ 1/s}$  for the X-ray irradiated sensor; it may be of interest to explore the corresponding timescale for a proton-irradiated sensor in future measurements. The beam-induced current jump was found to have increased by a factor of three after a TID of around 1 kGy. A second ingrow effect was observed even without impinging radiation, where the leakage current of a powered, but unbiased sensor was found to grow in during the first  $\sim 100$  seconds. This finding is indicative of a leak between the low voltage power supplies and the biasing circuit, and warrants closer investigation. Regardless of the source of the ingrow, the observation shows that it is necessary allow sufficient time for the leakage current to stabilise during measurements.

The fluence dependence of the leakage current during proton irradiation was shown to be consistent with radiation-induced acceptor removal. After proton irradiation, the temperature dependence of the leakage current was found to be consistent with electron-hole generation in the silicon bulk.

For photon irradiation, the leakage current was found to have increase by two orders of magnitude after a TID of around 3.2 kGy.

The breakdown voltage showed a qualitatively comparable behaviour after both proton and photon irradiation: an initial drop followed by a recovery effect, as well as an overall

decrease in breakdown voltage after irradiation. As it is not currently known whether the recovery can be attributed to annealing, discharging, or other effects, a measurement of the recovery time constant may be an instructive next step.

As the precise location and mechanism of the breakdown observed in the AP 3.1 are currently unknown, any attempts to explain the observed breakdown behaviour remain speculative; however, the temperature dependence of the breakdown voltage was found to be consistent with the hypothesis that the observed early breakdown of the ATLASPix is an avalanche effect. The overall behaviour was comparable before and after proton irradiation, indicating that the breakdown mechanism was not significantly modified after a total proton fluence of  $\phi_{\text{eq}} \approx 1 \cdot 10^{14} \text{ n}_{\text{eq}}/\text{cm}^2$ .

Measurements of S-Curves and VDAC voltages before and after proton irradiation showed a significant increase of the pixel threshold, but tentatively ruled out global shifts in the voltages *th*, *bl*, and *inj* as the cause.

A significant increase in noise was found after proton irradiation, with observations indicating that a large portion of noise can be attributed to a small fraction of pixels; at the same time, around half the pixel matrix was lost after a proton fluence equivalent to less than a fifth of the expected lifetime fluence of the MightyPix.

In spite of some systematic limitations that emerged during the work presented in this thesis, a good amount of progress was made both in building the infrastructure facilitating future investigations of this sort, and in identifying pitfalls to be avoided in the future. These include, but are not limited to, stringent measurements in temperature-controlled settings, and full sensor characterisation runs before and after irradiation campaigns. Progress was also made in providing pointers for future studies, which may include the separate irradiation of the periphery, irradiation campaigns to higher fluences, and determining the time constants of recovery effects.

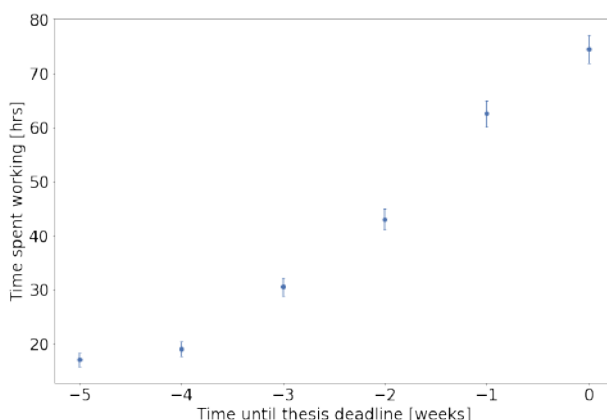
# Acknowledgements

There are many people I owe a big thank you to, and I would like to acknowledge at this point.

First and foremost, Sebastian - thank you for guiding me through this year, and putting up with all the last-minute corrections of everything that I output. In acknowledgement of that I attach a copy of piece of modern art that I have hanging above my desk. It turns out, by the way, that the relationship between the last-minute panic and the inspiration in question is linear. The experimental data on which this observation is based is included for good measure (no, this level of linearity was neither pre-mediated nor anticipated. Yes, the data is real).



(a) Based on real events. [47]



(b) Cumulative hours per week spent working on this thesis as a function of remaining time until deadline.

**Fig. 9.45** One last figure, because now I can't stop.

Prof. Ulrich Uwer I'd like to thank for giving me the opportunity to work in this fantastic research setting, and for fostering such a great working environment within the group.

To Prof. Silvia Masciocchi - thank you for agreeing to be my second referee at short notice!

To Lucas, or the *Chip Whisperer*, with whom I share the misery of putting up with a gaggle of moody ATLASPixes: thank you for saving me from many a chip crisis! An alternative title of this thesis is, "The ATLASPix 3.1: A tale in *why though?*". That said, debugging our knowledge of the Universe one ATLASPix at a time is exhausting, but pretty cool. Either way, thanks also for looking over my thesis, and for being an all-around fun person to work with!

To the Mu3e group in Heidelberg, as well as the MightyPix group everywhere else: thank

you for many insightful discussions! Also for the fun at the DESY testbeam with everyone who participated.

In the same vein, special thanks to everyone who made the Bonn testbeam happen!

To my family, who always, always have my back: I can't express the amount of gratitude I have for your support. Really.

And finally, to my housemates and friends, whose Venn diagrams thankfully overlap in the form of a fried egg (sunny side up), and who may or may not have kept me fed this past month where I was chained to my desk: Thank you so much for the amount of joy (and unannounced cake) you put in my life even when I'm a complete hermit. I look forward to jamming and climbing with you again!

# Bibliography

- [1] S. L. Glashow. “Partial Symmetries of Weak Interactions”. *Nucl. Phys.* 22 (1961), pp. 579–588 (p. 17).
- [2] Wikimedia Commons. Standard Model of Elementary Particles. url: [https://en.wikipedia.org/wiki/File:Standard\\_Model\\_of\\_Elementary\\_Particles.svg](https://en.wikipedia.org/wiki/File:Standard_Model_of_Elementary_Particles.svg).
- [3] I. Belyaev, G. Carboni, N. Harnew, C. Matteuzzi, F. Teubert, ”The history of LHCb”. *The European Physical Journal H.* 46 (2021). doi:10.1140/epjh/s13129-021-00002-z.
- [4] A. Sakharov, ”Violation of CP invariance, C asymmetry, and baryon asymmetry of the universe”. *Pisma Zh. Eksp. Teor. Fiz.* 5 (1967) 32
- [5] M. Thomson, ”Modern Particle Physics”. Cambridge University Press, Cambridge, 2013.
- [6] LHCb Collaboration, ”LHCb Tracker Upgrade Technical Design Report”. Tech. rep. 2014. url: <https://cds.cern.ch/record/1647400>
- [7] T. Ackernley et al., ”Mighty Tracker: Design studies for the downstream silicon tracker in Upgrade Ib and II”. Tech. Rep. LHCb-INT-2019-007. CERN-LHCb-INT-2019-007, CERN, Geneva, Feb, 2019.
- [8] D. Murray, ”Developing silicon pixel detectors for LHCb: constructing the VELO Upgrade and designing a MAPS-based tracking detector”. PhD Thesis, University of Manchester, 2022.
- [9] E. Vilella, ”HV-CMOS chip design experience”. Presented at the IT/MT for U2 upgrade: kickoff meeting, March, 2019.
- [10] M.S. Tyagi, R. Van Overstraeten, ”Minority carrier recombination in heavily-doped silicon, *Solid-State Electronics*”. 26 (1983) 577–597. doi:10.1016/0038-1101(83)90174-0.
- [11] J. Hammerich, ”Towards MightyPix, an HV-maps for the LHCb mighty tracker upgrade”. *Journal of Instrumentation* 17, (2022).
- [12] M. Tanabashi et al. “Review of Particle Physics”. *Phys. Rev. D* 98 (3 Aug. 2018), p. 030001. doi: 10.1103/PhysRevD.98.030001. url: <https://link.aps.org/doi/10.1103/PhysRevD.98.030001> (pp. 17, 19, 26, 28).
- [13] O. Krasel, C. Gossling, R. Klingenberg, S. Rajek, and R. Wunstorf, “Measurement of trapping time constants in proton-irradiated silicon pad detectors”. *IEEE Trans. Nucl. Sci.*, vol. 51, no. 6, pp. 3055–3062, Dec. 2004
- [14] M. Moll, “Radiation Damage in Silicon Particle Detectors - microscopic defects and macroscopic properties”. PhD thesis, University of Hamburg, 1999.

- [15] M. Moll, "Displacement Damage in Silicon Detectors for High Energy Physics". IEEE Transactions on Nuclear Science, vol. 65, no. 8, pp. 1561-1582, Aug. 2018. doi: 10.1109/TNS.2018.2819506.
- [16] M. Moll, "Acceptor removal - Displacement damage effects involving shallow acceptor doping of p-type silicon devices". Proceedings of Science, Vertex 2019, pp. 27, 2020. doi: 10.22323/1.373.0027
- [17] M. Moll, E. Fretwurst, G. Lindström, "Investigation on the improved radiation hardness of silicon detectors with high oxygen concentration". Nuclear Instruments and Methods in Physics Research Section A: Accelerators, Spectrometers, Detectors and Associated Equipment, vol 439, no. 2, pp. 282-292, 2000. doi: 10.1016/S0168-9002(99)00842-6
- [18] M. Moll, E. Fretwurst, M. Kuhnke, and G. Lindström, "Relation between microscopic defects and macroscopic changes in silicon detector properties after hadron irradiation". Nucl. Instrum. Methods Phys. Res. B, Beam Interact. Mater. At., vol. 186, pp. 100–110, Jan. 2002.
- [19] R. Schimassek, "Development and characterisation of integrated sensors for particle physics." Karlsruhe, 2021. url: <http://dx.doi.org/10.5445/IR/1000141412>.
- [20] W. Adam et al., "Trapping in proton irradiated p+-n-n+ silicon sensors at fluences anticipated at the HL-LHC outer tracker". J. Instrum., vol. 11, no. 4, p. P04023, 2016
- [21] I. Pintilie, G. Lindstroem, A. Junkes, and E. Fretwurst, "Radiation-induced point- and cluster-related defects with strong impact on damage properties of silicon detectors". Nucl. Instrum. Methods Phys. Res. A, Accel. Spectrom. Detect. Assoc. Equip., vol. 611, pp. 52–68, Jun. 2009.
- [22] R. Wunstorf, "Systematische Untersuchungen zur Strahlenresistenz von Silizium-Detektoren für die Verwendung in Hochenergiephysikexperimenten". Ph.D. thesis, Dept. Phys., Univ. Hamburg, Hamburg, Germany, 1992.
- [23] L. Gonella et al. "Total Ionizing Dose effects in 130-nm commercial CMOS technologies for HEP experiments". Nuclear Instruments and Methods in Physics Research Section A: Accelerators, Spectrometers, Detectors and Associated Equipment 582.3 (2007). VERTEX 2006, pp. 750–754. issn: 0168-9002, doi: 10.1016/j.nima.2007.07.068.
- [24] G. Lutz., "Semiconductor Radiation Detector Device Physics". Springer-Verlag, 1st edition, 1999.
- [25] I. Peric, "A novel pixelated monolithic particle detector implemented in high-voltage CMOS technology". Nucl. Instr. Meth. A 582, 876 - 885 (2007)
- [26] H. Kolanoski, N. Wermes, "Particle Detectors". Oxford University Press, June 2020.
- [27] A. Herkert, "Characterization of a Monolithic Pixel Sensor Prototype in HV-CMOS Technology for the High-Luminosity LHC". PhD thesis, Heidelberg University, 2020.
- [28] Bacchetta, N., Bisello, D., Candelori, A., Da Rold, M., Descovich, M., Kaminski, A., Messineo, A., Rizzo, F., Verzellesi, G. (2001), "Improvement in breakdown characteristics with multiguard structures in microstrip silicon detectors for CMS". Nucl. Instrum. Meth. A, 461, 204–206.
- [29] K. Padeken, "The MightyTracker: Upgrade 2 of the Downstream Tracking System". Presented at the International Workshop on Pixel Detectors for Particles and Imaging, Santa Fe, 15.12.2022.

- [30] L. Rossi, P. Fischer, T. Rohe, N. Wermes, "Pixel Detectors: From Fundamentals to Applications". Springer Berlin Heidelberg New York, 2006, ISBN-13: 978-3-540-28332-4
- [31] M. Moll, "Acceptor removal - Displacement damage effects involving the shallow acceptor doping of p-type silicon devices". PoS, Vertex2019, 027, 2020.
- [32] G.-F. Dalla Betta, N. Ayllon, M. Boscardin, M. Hoeferkamp, S. Mattiazzo, H. McDuff, R. Mendicino, M. Povoli, S. Seidel, D.M.S. Sultan, N. Zorzi, "Investigation of leakage current and breakdown voltage in irradiated double-sided 3D silicon sensors". Journal of Instrumentation, 11(09), P09006, 2016.
- [33] DMS Sultan, S. Gonzalez Sevilla, D. Ferrere, G. Iacobucci, E. Zaffaroni, W. Wong, M.V. Barrero Pinto, M. Kiehn, M. Prathapan, F. Ehrler, I. Peric, A. Miucci, J. Kenneth Anders, A. Fehr, M. Weber, A. Schoening, A. Herkert, H. Augustin, M. Benoit (2019), "Electrical characterization of AMS aH18 HV-CMOS after neutrons and protons irradiation". Journal of Instrumentation, 14(05), C05003.
- [34] J. Hammerich, PhD thesis in preparation, University of Liverpool.
- [35] J. Hammerich, "Analog Characterization and Time Resolution of a large scale HV-MAPS Prototype". Master Thesis, University of Heidelberg, 2018.
- [36] L. Dittmann, "Tests of an HV-CMOS Prototype for the LHCb MightyTracker". Master Thesis, University of Heidelberg, 2022.
- [37] E. Vilella, "HV-CMOS chip design experience". Presented at the IT/MT for U2 upgrade: kickoff meeting, 16 Mar. 2018
- [38] G. Masetti, M. Severi, and S. Solmi, "Modeling of carrier mobility against carrier concentration in arsenic-, phosphorus-, and boron-doped silicon". IEEE Transactions on Electron Devices 30.7 (1983), pp. 764–769. doi: 10.1109/T-ED.1983.21207
- [39] N. Thomopoulos, "Statistical Distributions: Applications and Parameter Estimates", Springer International Publishing, 2017. doi: 10.1007/978-3-319-65112-5
- [40] P. Wolf, "A Proton Irradiation Site for Silicon Detectors at Bonn University". Presented at the DPG Frühjahrstagung 2022, Heidelberg, T13: Semiconductor Detectors.
- [41] Laboratoire National Henri Becquerel. LNE-LNHB/CEA - Table de Radionucléides -  $^{55}\text{Fe}$ . [Online; Last accessed Friday 27th January 2023]. URL: [http://www.lnhb.fr/nuclides/55Fe\\_tables.pdf](http://www.lnhb.fr/nuclides/55Fe_tables.pdf).
- [42] Private communication
- [43] I. Perić, ATLASPIX3 user manual, Karlsruhe Institute of Technology (KIT), Karlsruhe, 2019, accessed: 07.11.2021. [Online]. Available: [https://adl.ipe.kit.edu/downloads/ATLASPIX3\\_um\\_v1.pdf](https://adl.ipe.kit.edu/downloads/ATLASPIX3_um_v1.pdf)
- [44] LHCb collaboration, R. Aaij et al., "LHCb detector performance", Int. J. Mod. Phys. A30 (2015) 1530022, arXiv:1412.6352.
- [45] R. Schimassek, "Description of the GECCO Test System". 2021. url: [https://git.scc.kit.edu/adl\\_documents/gecco\\_documentation](https://git.scc.kit.edu/adl_documents/gecco_documentation).
- [46] Ryunosuke O'Neil, "HV-MAPS for the LHCb Upgrade-II Mighty Tracker". The International Workshop on Vertex Detectors (VERTEX 2022). 2022. url: <https://cds.cern.ch/record/2838632>.
- [47] B. Watterson, "MOOD", 1992

Erklärung:

Ich versichere, dass ich diese Arbeit selbstständig verfasst habe und keine anderen als die angegebenen Quellen und Hilfsmittel benutzt habe.

Heidelberg, den 31.01.2023

A handwritten signature in black ink, written over a horizontal dotted line. The signature is cursive and appears to read 'Münster'.